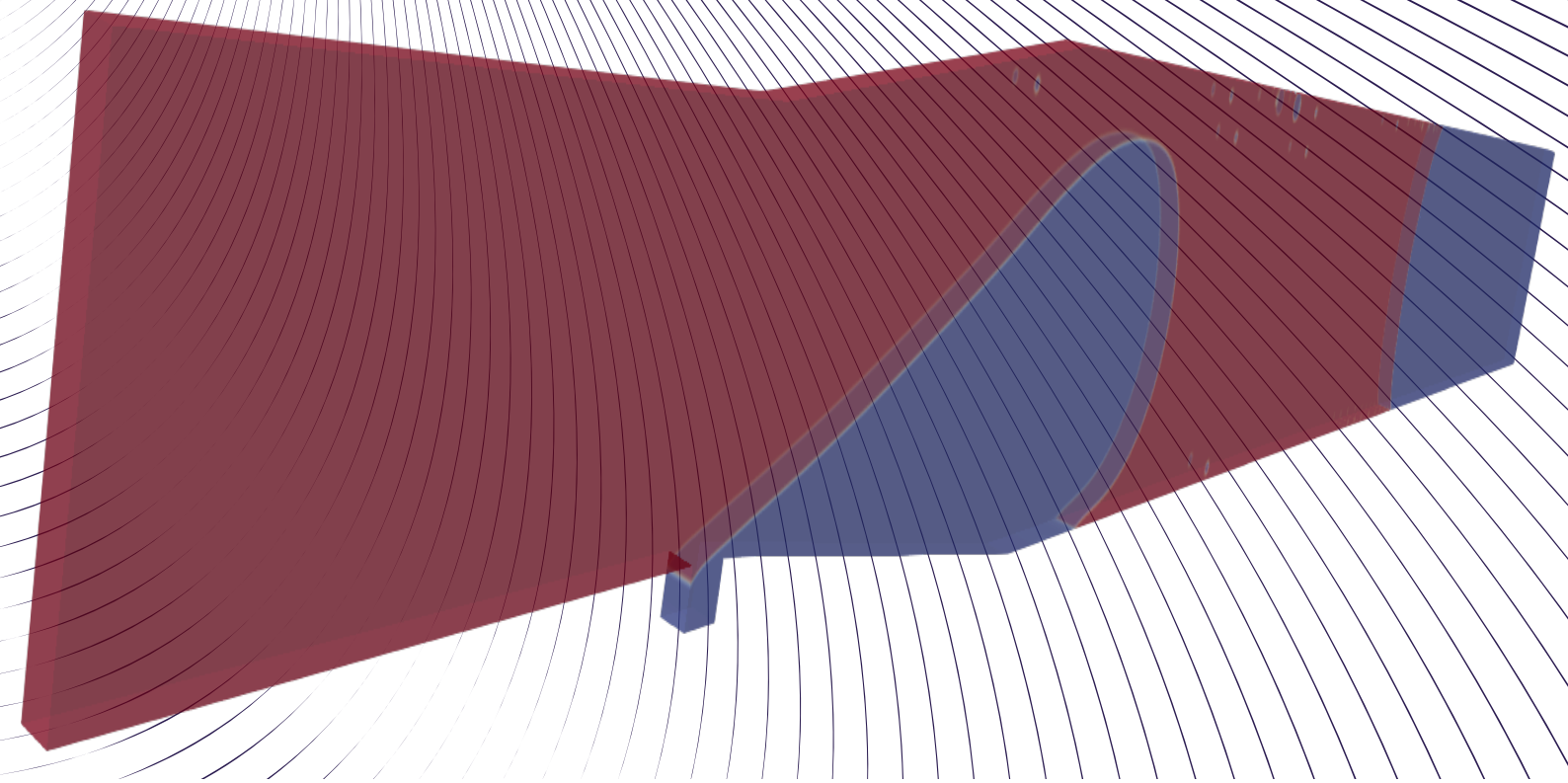

Numerical Investigation of Flow Boiling in Divergent Shaped Microchannels

L. Kæhler & T. Lynggaard

Thermal Energy and Process Engineering, TEPE4-1007, 2021-12

STUDENT REPORT

AALBORG UNIVERSITY

Department of Energy Technology
Aalborg University
http://www.aau.dk

AALBORG UNIVERSITY
STUDENT REPORT

Title:
Numerical Investigation of Flow Boiling in Divergent Shaped Microchannels

Project Period:
01/02/21 - 28/05/21

Project Group:
TEPE4-1007

Participants:
Lars Kæhler
Tobias Lynggaard

Supervisor:
Jakob Hærvig

Page Numbers: 62

Date of Completion:
28/05/2021

Abstract:

Flow boiling in microchannels is one of the most promising cooling technology for compact electronics, however, more knowledge is required on the subject. In the present work, flow boiling is numerically investigated in a divergent microchannel with different slopes. This is done using volume of fluid and dynamic mesh refinement based CFD solver in OpenFOAM. First, the accuracy of the solver is tested by comparison to the analytic solution of a Stefan Problem. Furthermore, the solver is validated by comparison to the Nusselt number correlations of Berenson and Klimenko by simulating a film boiling problem. Two-dimensional flow boiling simulations of ethanol are performed in a microchannel with subcooled laminar inlet conditions, a constant heat flux specified at all walls, and a cavity implemented as nucleation site. The influence of the wall slope and the Boiling number are investigated upon the heat transfer performance and bubble dynamics. The simulations show that an increase in the Boiling number increases the bubble growth rate, diameter, and affects the detachment time. The slope of the wall also affects the bubble dynamics, the flow velocity, and the local Boiling number. The simulations show that the highest Nusselt number and thus heat transfer is obtained when a liquid film layer is present and that the liquid film layer is dependent on both the wall slope and the Boiling number.

Executive Summary

Recent decades have seen a rapid development in the technology of electric components, which tends to become more compact and yet often more powerful. This tendency implies high requirements to the cooling system, and here microchannel flow boiling is one of the most promising technologies. However, the technology is associated with instabilities, and more research is required to reach its full potential. One solution to minimise the instabilities associated with microchannel flow boiling is to design the channel with a divergent shape. In the present study, flow boiling in microchannels is numerically investigated. A parameter variation is performed upon the slope of the walls and the Boiling number, and the influences are investigated for the heat transfer performance and bubble dynamics.

First, the accuracy of the solver is investigated by solving a 1D Stefan problem and comparing the numerical results to the analytic solution in relation to the interface position. The simulation is performed with, respectively, the Lee and Tanasawa phase-change model. Here, the numerical simulations with, respectively, the Lee and Tanasawa method show an error of 2.4 % and 0.25 % to the analytic solution. Hence, a high accuracy of the solver is proven, and the Tanasawa phase-change model is implemented for the further work. The accuracy of the solver is, furthermore, investigated by solving a 2D film boiling problem which can be seen in Figure 4.10. The space-averaged Nusselt number at the bottom wall is calculated and compared to the Nusselt number correlations presented by Berenson and Klimenko as shown in Figure 3b. An error of 14 % and 31 % are seen to, respectively, the Berenson and Klimenko correlations for the time- and space-averaged Nusselt number. Compared to the numerical results of other researchers, the accuracy of the simulation is found to be within an acceptable range. A grid independence study has, furthermore, been made. It is found that the feature of dynamic mesh refinement can be applied without compromising the accuracy of the results.

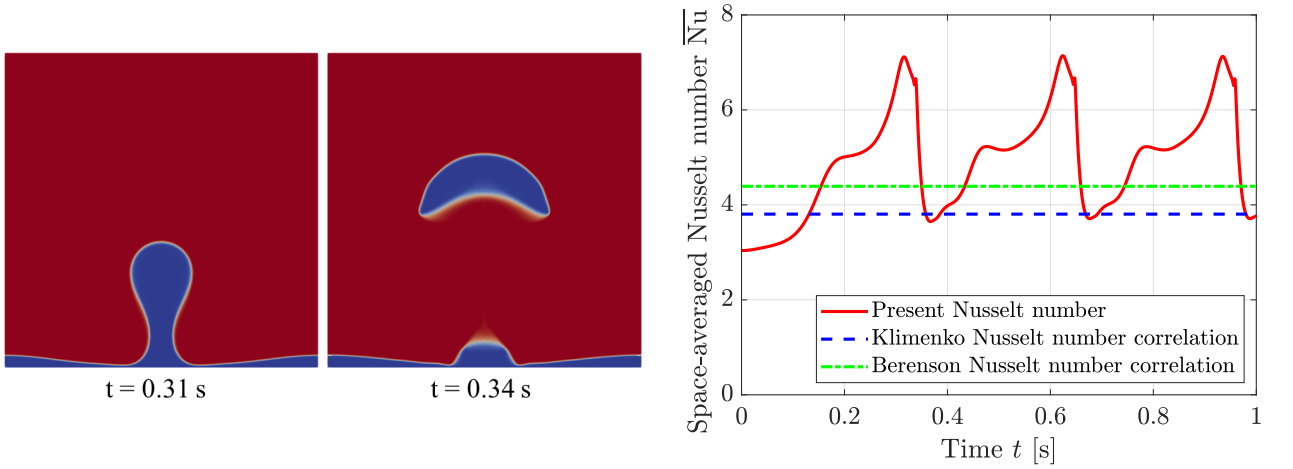

(a) View of film boiling with bubble detachment, P_{sat} = 21.9 MPa and $T_w = T_{sat}$ + 5 K.

(b) Nusselt number comparison for the correlations of Berenson and Klimenko and for the numerical simulation, P_{sat} = 21.9 MPa and $T_w = T_{sat}$ + 5 K.

Figure 1

The microchannel flow boiling is simulated for, respectively, a Boiling number of $1.25 \cdot 10^{-4}$ and

$1.75 \cdot 10^{-4}$ and multiple different wall slopes. The simulations show that the Boiling number has an significant influence upon the bubble dynamics as seen in Figure 6.1. Here, it can be seen that the bubble growth rate and the bubble size are larger for the higher Boiling number. The 40 % increase in the Boiling number yields a 43.2 % increase in the diameter of the bubble. The bubble dynamics are also affected by the slope of the wall. The simulations show that an increase in the wall slope causes an decrease in the bubble velocity and changes in the bubble size. By increasing the wall slope and the Boiling number together, the bubble diameter is increased with almost 100 %.

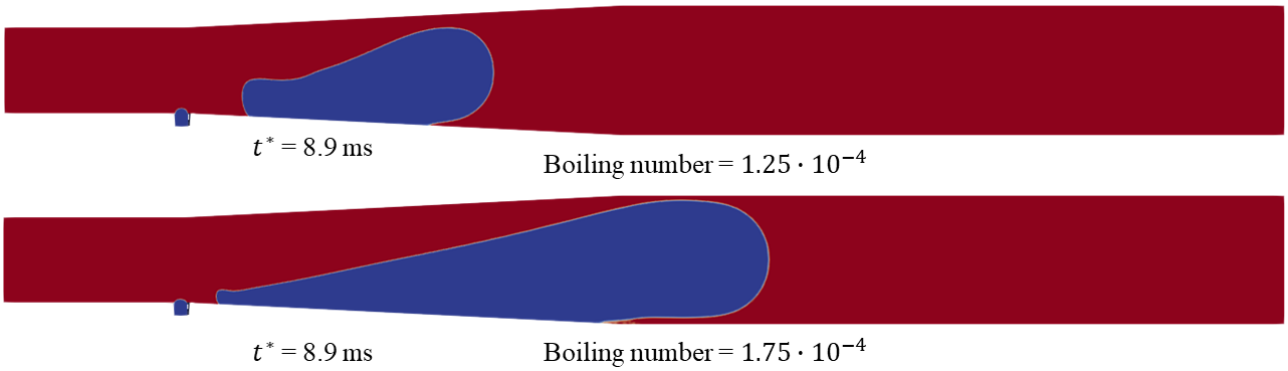

Figure 2: Flow boiling for the dimensionless time $t \cdot U_{\text{in}}/d_{\text{h}}$ with a Boiling number of, respectively, B = $1.25 \cdot 10^{-4}$ and $1.75 \cdot 10^{-4}$.

The heat transfer performance of the microchannel is investigated in relation to the Nusselt number. The simulations show that the highest Nusselt number is taking place when a thin liquid film layer is present. Furthermore, it is found that the liquid film layer is based on a combination of the Boiling number and the wall slope. A presentation of the area-weighted volume fraction and the local Nusselt number is shown in Figure 3. It can be seen that the Nusselt number peaks at the same time as the volume fraction is close to zero. This indicates that a liquid film layer is present and moves by the measuring point.

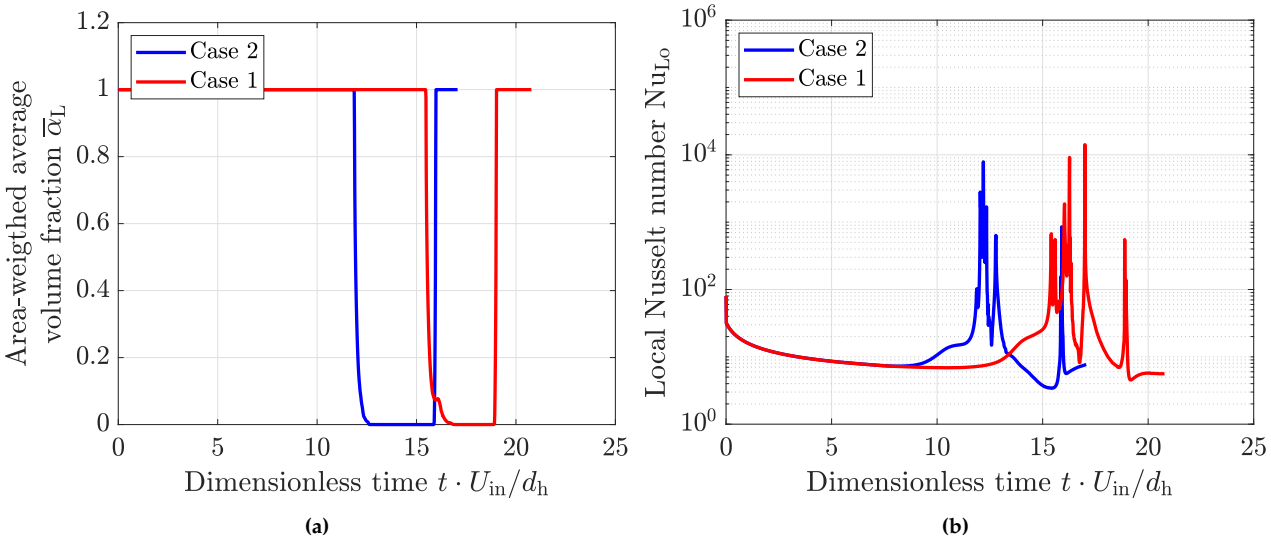

Figure 3: The area-weighted average volume fraction of liquid and the local Nusselt number measured at a fixed point near the outlet of the upper wall to the dimensionless time $t \cdot U_{\text{in}}/d_{\text{h}}$.

Preface

This thesis is written by group TEPE4-1007 consisting of Lars and Tobias during the spring semester of 2021. This is a Master's project for M.Sc. in *Thermal Energy and Process Engineering* at the *Department of Energy Technology* at Aalborg University. The thesis has been written under the guidance of Jakob Hærvig, assistant professor at Aalborg University.

Reading Instructions

The references and citations are made in accordance with the Harvard method, marked as: [Surname of main author, year]. The bibliography can be found at the end of the thesis, and here the sources are listed in alphabetic order. The dimensionless numbers, symbols, subscripts, and abbreviations used throughout the report are listed in the nomenclature, which is found after the table of contents.

Applied Software

This is a numerical study that is set up and simulated using OpenFOAM version 8. OpenFOAM is an acronym for Open Source Field Operation and Manipulation and is a CFD program capable of simulating the action of thermo- and fluid dynamics. The program has a selection of standard solvers, and the solvers are made for different types of cases. The solver chosen for the present study is not a standard solver but a solver assembled by Ali Yahyaee Nujukambari, a PhD student at Aalborg University. A description of the basics of the solver will be presented in the present work. To run the simulations, 32 cores at a cluster has been provided by the Energy Department of Aalborg University. ParaView and MATLAB® are used to post-processing the numerical data and the graphical representations, and EES is used to look up the thermal properties unless otherwise stated.

Aalborg University, May 28, 2021

Lars Kæhler
Lars Kæhler
<lkahle16@student.aau.dk>

Tobias Lynggaard
Tobias Lynggaard
<tlyngg16@student.aau.dk>

Contents

Nomenclature

Dimensionless numbers	Description
$\mathrm{B} = \frac{\dot{q}}{H_{\mathrm{lg}}\,\dot{m}''}$	Boiling number
$\mathrm{Bo} = \frac{g(\rho_{\mathrm{l}}-\rho_{\mathrm{g}})d_{\mathrm{h}}^2}{\sigma}$	Bond number
$\mathrm{Ca} = \frac{U_{\mathrm{in}}\,\mu_{\mathrm{l}}}{\sigma}$	Capillary number
$\mathrm{Gr} = \frac{\rho_{\mathrm{g}}^2\, g\, \lambda^3}{\mu_{\mathrm{g}}^2}\left(\frac{\rho_{\mathrm{l}}}{\rho_{\mathrm{g}}} - 1\right)$	Grashof Number
$\mathrm{Nu} = \frac{d_{\mathrm{h}}\,\frac{\partial T}{\partial n}\vert_{n=0}}{T_{\mathrm{w}}-T_{\mathrm{bulk}}}$	Nusselt number
$\mathrm{Nu}_\lambda = \frac{\lambda}{T_{\mathrm{w}}-T_{\mathrm{sat}}}\frac{\partial T}{\partial n}\vert_{n=0}$	Nusselt number for the Taylor wave
$\mathrm{Pr} = \frac{C_{\mathrm{p,g}}\,\mu_{\mathrm{g}}}{k_{\mathrm{g}}}$	Prandtl number
$\mathrm{Re}_d = \frac{U_{\mathrm{in}}\,d_{\mathrm{h}}}{\nu_{\mathrm{l}}}$	Reynolds number with respect to d_{h}

Symbol	Description	Unit
A	Area	m^2
a	Thermal diffusivity	m^2/s
$\mathrm{C_a}$	Compressive factor	-
C_p	Specific heat Capacity	J/(kg K)
d_{h}	Hydraulic diameter	m
g	Gravitational acceleration	$\mathrm{m/s}^2$
H_{lg}	Latent heat of vaporisation	J/kg
h	Heat transfer coefficient	$\mathrm{W/(m^2\ K)}$
k	Thermal conductivity	W/(m K)
K	Interface curvature	1/m
l	Length	m
M	Molecular weight	kg/kmol
$\dot{m}$	Mass Flow	kg/s
$\dot{m}''$	Mass flux rate	$\mathrm{kg/(m^2\ s)}$
$\dot{m}'''$	Volumetric mass rate	$\mathrm{kg/(m^3\ s)}$
P	Pressure	Pa
$\dot{q}$	Heat flux	$\mathrm{W/m^2}$
$\dot{Q}$	Heat transfer rate	W
R	Universal gas constant	J/(K mol)
r	Mass transfer intensity factor	1/s
S	Surface	-
t	Time	s
T	Temperature	K
U	Velocity	m/s
V	Volume	m^3

x	Position on the x-axis	m
y	Position on the y-axis	m

Greek symbols	**Description**	**Unit**
α	Volume fraction with respect to water	kg/m^3
β	Phase change number	-
η	Solution to transcendental eq.	-
ϵ	Perturbation wave amplitude	m
γ	Phase-change coefficient	-
λ	Characteristic length of Taylor wave	m
μ	Dynamic viscosity	kg/(m s)
ν	Kinematic viscosity	m^2/s
Φ	Represents thermo-physical properties	
ρ	Density	kg/m^3
σ	Surface tension	N/m
θ	Contact Angle	-

Subscipts	**Description**
b	Bubble
Be	Berenson
c	Compressive
C	Cell
co	Condensation
D	Domain
e	Evaporation
freez	Freezing
g	Gas
Kli	Klimenko
l	Liquid
i	Interface
in	Inlet
Sat	Saturation
TBL	Thermal Boundary Layer
u	Unperturbed film
w	Wall

Other	**Description**
$*$	Non-Dimensionalised Value
$\langle\rangle$	Average over time
—	Average over a surface
∞	Free stream

$*$	Non-Dimensionalised Value
$'$	per meter $1/m$

Abbreviations	**Description**
CFD	Computational Fluid Dynamics
ONB	Onset of Nucleate Boiling
VOF	Volume Of Fluid
1D	One-Dimensional
2D	Two-Dimensional
3D	Three-Dimensional

Chapter 1

Introduction

The demand for cooling of electronic systems has increased over the past decades and will further increase as the electronic components are becoming more compact yet often more powerful. Karayiannis and Mahmoud (2017) claim that the heat dissipation from computational chips will reach 2 - 4.5 MW/m^2 with local hot spots up to 12 - 45 MW/m^2 by 2026. This implies that better cooling systems are required since air cooling is inadequately for most applications over 1 MW/m^2 (Tullius et al., 2011).
Multiple cooling technologies are investigated by Agostini et al. (2007), and they conclude that flow boiling in microchannels is the most promising solution. Here microchannel flow boiling obtains high heat fluxes even at low mass fluxes, contributing to a low required pumping power making it more efficient than other technologies. One advantage of a microchannel is the high-surface-area-to-volume ratio, which enhances the heat transfer coefficient. This is also shown by Kandlikar et al. (2006) as seen in Figure 1.1 where a lower hydraulic diameter and thus a higher surface-area-volume ratio results in a higher heat transfer coefficient.

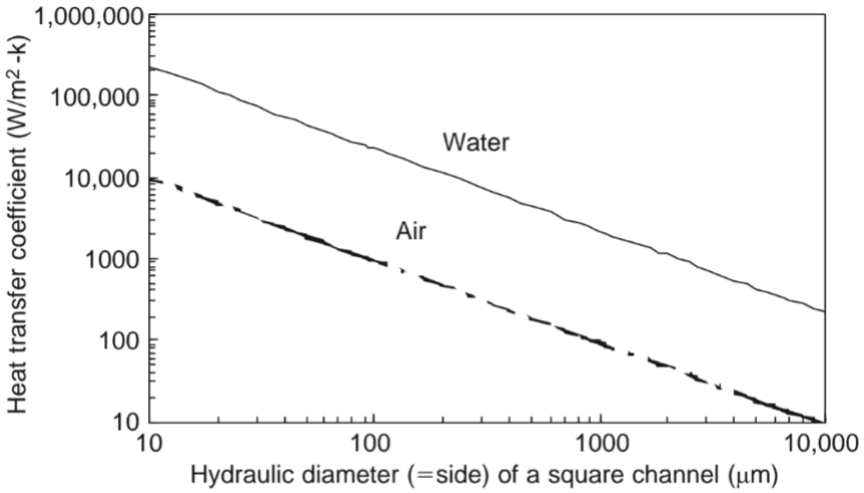

Figure 1.1: The effect of the hydraulic diameter and thus the surface-area-to-volume ratio upon the heat transfer coefficient for a laminar single-phase flow in a channel (Kandlikar et al., 2006).

Another advantage in microchannel flow boiling is that the heat transfer of latent heat of evaporation can be orders higher than the sensible heat of single-phase cooling. Flow boiling also contributes to a very uniform surface temperature, typically within a few degrees, in the channel. This near-isothermal performance is advantageous in many applications, e.g., electronic components that have the best performance and lifespan at specific operating temperatures (Tullius et al., 2011). Kandlikar et al. (2006) compared single- and two-phase flow in a microchannel with a hydraulic diameter of 200 μm under laminar flow conditions. They found that flow boiling in a microchannel can exceed a heat transfer coefficient of 100 000 W/m^{2}K, where a single-phase flow can reach 10 000 W/m^{2}K as seen in Figure 1.1. The disadvantage of flow boiling compared to other methods is that less knowledge exists on this subject. However, more and more researchers are looking into flow boiling

in a microchannel due to its high potential.

1.1 State of the Art of Flow Boiling in Microchannels

A wide range of experimental and numerical investigations of flow boiling in microchannels have been conducted over the past decades. This includes an investigation of the optimal shape and size of a microchannel. Not all agree on how a microchannel is specified, but Kandlikar (2002) states it to be when the hydraulic diameter d_h is between 10 and 200 μm, and this is therefore also the specification for a microchannel in the present work. In Table 3, a review of multiple microchannel flow boiling studies are made and it can be seen on the hydraulic diameter used that not everybody agree on the microchannel definition. It can also be seen that different microchannel shapes have been investigated. For the optimal shape of a microchannel, Yen et al. (2006) experimentally investigated the difference between a square channel and a circular channel. They used Pyrex glass as the channel material in order to observe what occurs inside the channel. They found that the squared channel has a higher heat transfer coefficient since the corners operate as nucleation sites. Magnini and Matar (2020b) have numerically investigated the impact of the shape of the microchannel for rectangular and square channels with a maximum aspect ratio of 8. They discovered that the square channel has a higher heat transfer coefficient at low flow rates due to a thinner liquid film thickness, but this also made the square channel more likely to get dry-out zones. Whereas the rectangular channels has a higher heat transfer coefficient at high flow rates.

Dry-out zones are not an uncommon phenomenon for flow boiling in microchannels and have been observed experimentally by many researchers (Steinke and Kandlikar, 2004), (Serizawa et al., 2002). The more confined space in microchannels compared to conventional channel makes the dry-out more likely to occur. The confined space also affects the flow patterns seen in microchannels compared to the known flow patterns from conventional channels. Serizawa et al. (2002) investigated the flow patterns for a microchannel with a hydraulic diameter of 50 μm using water and observed the following four flow patterns; bubbly flow, slug flow, liquid ring flow, and liquid droplet flow. The bubbly flow and the slug flow are also known from the conventional channel. However, due to the confined space, the slugs fill most of the cross sectional area, which is in contrast to the relatively smaller slugs in the conventional channels. This makes the slug flow regime interesting since a small liquid film layer is present between the slug and the heated wall enhancing the local heat transfer (Ferrari et al., 2018a).

The numerical investigation of slug flow in microchannel has been performed in various ways. Many researchers are not simulating the onset of bubble nucleation since their phase-change model are only capable of evaporating the liquid at the interface of an already existing vapour bubble. Some researchers are therefore creating the slug by seeding a small bubble at the wall in beginning of the channel. Due to constant heat flux or constant temperature defined at the wall, the bubble evaporates and grows into a slug (Ling et al., 2015), (Mukherjee et al., 2011). Other researchers seed the entire slug in the beginning of the channel (Magnini et al., 2013b), (Okajima and Stephan, 2019). The liquid film layer surrounding the bubble becomes superheated due to a constant heat flux or constant temperature defined at the wall, which makes the bubble grow. Only one article is found where the bubble is nucleating from a cavity in flow boiling (Jafari and Okutucu-Özyurt, 2016).

The nucleation sites have a significant influence on the bubble growth and bubble detachment in the flow boiling. In practical applications, the nucleation of bubbles is taking place in cavities placed in the surface of the channel. Different cavities are active as nucleation site depending on the cavity

size, local wall temperatures, and local liquid temperature (Kandlikar, 2006). These parameters, likewise, affect the bubble size before detachment. A large bubble diameter can result in the bubble filling out the entire cross-sectional area, and this can lead to instabilities such as reversed flow (Prajapati and Bhandari, 2017).

Table 1.1: Overview of articles investigating flow boiling in microchannels.

Author	Coolant	Channel size and shape	Method
Ferrari et al. (2018a)	R245fa	Square channel D_h = 100 [μm]	Numerical (OpenFOAM) Using VOF method. 3D, where only a fourth of the channel is simulated. Seeding of a bubble.
Magnini et al. (2013b)	R113 R245fa	Circular channel D_h = 500 [μm]	Numerical (Ansys Fluent) Using VOF method. 2D axisymmetrical. Seeding of a bubble.
Okajima and Stephan (2019)	FC-72	Circular channel D_h = 200 [μm]	Numerical (OpenFOAM) Using VOF method. 2D axissymmetrical. Seeding of a bubble.
Pan et al. (2020)	R113	Square channel D_h = 200 [μm]	Numerical (Ansys Fluent) Using VOF method. 2D. Seeding of a bubble.
Serizawa et al. (2002)	Water	Circular channel D_h = 50 [μm]	Experimental, microscope and high speed camera. Silicia tube connected to a stainless steel tube heated by DC current.
Jafari and Okutucu-Özyurt (2016)	Water	Square channel D_h = 100 [μm]	Numerical, Cahn–Hilliard phase-field method. 2D. Bubble nucleation from a cavity.
Hetsroni et al. (2006)	Water Ethanol	Triangular channel D_h = 100 - 220 [μm]	Experimental, microscope and high speed camera.
Lee and Mudawar (2008)	HFE7100	Rectangular channel Aspect ratio = 2.47 - 4.27 D_h = 175.7 - 415.9[μm]	Experimental, high speed video imaging and photomicrography.

1.1.1 Instabilities

According to Prajapati and Bhandari (2017) instabilities are more frequent to occur in microchannels compared to conventional channels. The main reason for this is the more confined space in microchannels (Wang et al., 2007). The confined space makes a vapour bubble more likely to grow to a size where it fills out the entire cross sectional area. This phenomenon is also referred to as bubble clogging which can be seen visualised in Figure 1.2.

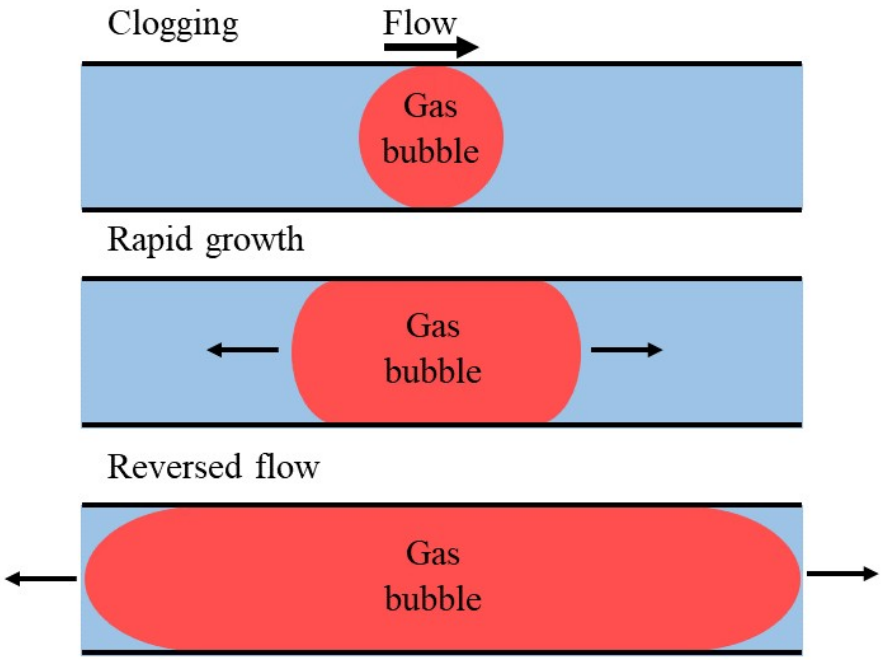

Figure 1.2: Visualisation of the instabilities in a microchannel refereed to as clogging, rapid growth, and reversed flow.

The phenomenon of bubble clogging is greatly affected by the subcooling of the inlet liquid and the ratio between the heat flux and the mass flux rate (Bogojevic et al., 2009). The ratio between the heat flux and the mass flux rate is also described as the Boiling number where the mass flux rate is multiplied by the enthalpy of vaporisation in order to make it non-dimensional. An increase in the Boiling number yields a more rapid evaporation meaning that bubble clogging is more likely to occur. If the the evaporation becomes too rapid, the bubble clogging can result in bubble growth in both the upstream and downstream direction as illustrated in Figure 1.2. This phenomena is called rapid growth and occurs since the bubble comes closer to the channel wall where a superheated liquid film layer near the wall increases the evaporation (Bogojevic et al., 2013). This can result in reverse flow where the flow is pushed upstream of the channel by the rapid growing bubble. For a system with a single microchannel the bubble eventually get pushed downstream of the channel when the pressure at the inlet has increased sufficiently (Brutin et al., 2003). However for a system with multiple microchannels it is possible for the reversed flow to exit the channel at the inlet where it then enters another channel as illustrated in Figure 1.3 (Steinke and Kandlikar, 2004).

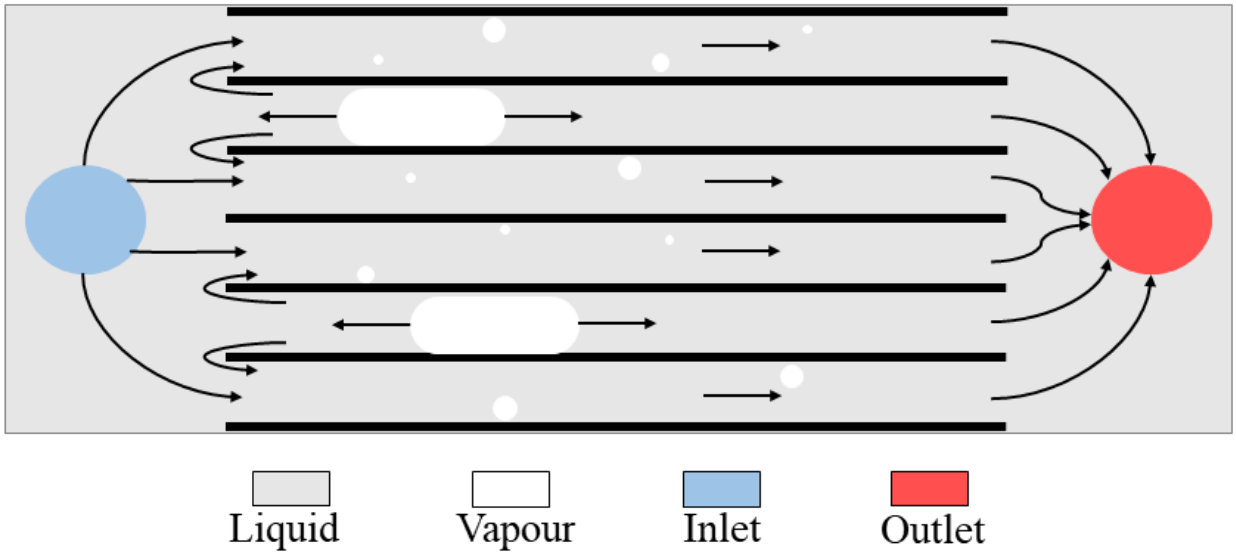

Figure 1.3: Illustration of the reversed flow phenomenon in a multiple microchannel system.

These three phenomena will for both the single channel and the multiple channel system result in oscillations in the pressure and the temperature which can lead to mechanical vibration in the heat sink (Bogojevic et al., 2013). These instabilities should therefore be avoided and this can first of all be done by changing the boiling number as previous stated. Another solution is to give the channel a divergent shape which Mukherjee and Kandlikar (2009) claim to have a positive effect on the above stated instabilities . This has been experimentally confirmed by Prajapati et al. (2015), however, to the best of the authors' knowledge no numerical investigations of different divergent channels have been made. Wang et al. (2012) found that the thermal properties of the coolant also have an affect on the instabilities. They compared ethanol and the refrigerant FC-72 and discovered that ethanol has a more steady wall temperature fluctuation. It is, therefore, crucial to choose the correct setup parameters and a suitable coolant.

1.1.2 Coolant

Multiple different coolants can be used in a microchannel for the cooling of electronic components. In Table 3 it can be seen that many types of coolants have been investigated in microchannel flow boiling. The table shows only a small portion of all the different coolants that can be used in microchannel flow boiling. So, in order to choose the most suitable coolant for the present work, some criteria need to be set. Some selected properties for the different coolant are, therefore, listed in Table 1.2.

Table 1.2: Overview of key parameters for different coolants at atmospheric pressure. Note that the properties for gas and liquid is at saturation temperature. Properties is given by EES.

	Water	**Ethanol**	**HFE7100**	**FC-72**	**R113**	**R245fa**
H_{lg} [kJ/kg]	2256	849.9	116.3	83	144.4	196
ρ_l/ρ_g [-]	1609	448.2	148	121.4	204.3	230.4
T_{sat} [°C]	100	78.4	61	56	47.6	14.9
T_{freez} [°C]	0	-114	-135	-90	-35	-106.7
μ_l [kg/m·s]	$2.818{\cdot}10^{-4}$	$4.475{\cdot}10^{-4}$	$3.918{\cdot}10^{-4}$	$4.38{\cdot}10^{-4}$	$5.1{\cdot}10^{-4}$	$4.66{\cdot}10^{-4}$
μ_g [kg/m·s]	$1.227{\cdot}10^{-5}$	$1.043{\cdot}10^{-5}$	$1.987{\cdot}10^{-5}$	-	$1.086{\cdot}10^{-5}$	$0.977{\cdot}10^{-5}$
σ [N/m]	0.05891	0.01764	0.009561	0.01	0.01468	0.0149

The coolant must be capable of keeping the temperature of the electronic components below 85 °C (Marcinichen et al., 2013). This means that water would have to be below atmospheric pressure in order to have a saturation temperature, T_{sat}, below 85 °C since it boils at 100 °C as seen in Table 1.2. Other coolants have to be above atmospheric pressure to avoid boiling at room temperature. Another issue is related to the freezing temperature T_{freez}. If the electronic components are to be used in cold environments, for example, under military operations in cold places, the water can freeze. In these environments, the refrigerants have the advantages due to low freezing temperatures as seen in Table 1.2. However, for refrigerants, the enthalpy of vaporisation, H_{gl}, is much lower than for water, and the exploit of latent heat are therefore reduced. Therefore, some researchers have been looking at alcohols such as ethanol since it provides good thermal properties while at the same time low freezing and boiling temperatures. Another aspect when choosing the suitable coolant is the density ratio between the liquid and gas ρ_l/ρ_g. A high-density ratio between liquid and gas can result in high temperature or pressure enhancing the instabilities. Numerically a low-density ratio is also desired since this reduces the simulation time due to lower velocities. Another parameter that should be considered when choosing a coolant is the impact it has on the environment. Parameters such as global warming potential and ozone layer potential have caused many refrigerants to be outfaced. Safety issues should also be considered if the microchannel e.g. is used for cooling of electronics, the coolant should be dielectric in case of leakage. In case of leakage it is also important that the coolant is not toxic. If there is a risk of very high temperatures then the flammability of the coolant should be considered. However most of these parameters depends on the application of the coolant.

1.2 Scope

Different coolants have been discussed in the previous section, and one of the criteria for the present work is that the coolant needs to have a saturation temperature at atmospheric pressure below 85 °C. Likewise is a high enthalpy of vaporising wanted to avoid rapid evaporation and to exploit the advantages of latent heat. Ethanol will therefore be the coolant for the flow boiling simulations of the present work, and no other coolants will be further investigated.

Researchers have proved the square and rectangular channel to obtain a higher heat transfer coefficient compared to the circular channel, as mentioned in Section 1.1 on page 2. Wang et al. (2012) claims that more research should be done on rectangular channels with high aspect ratios and that these channels have the potential of being used in industrial applications. Rectangular channels

with aspect ratios over eight can approximately be seen as two dimensional (2D) (Magnini and Matar, 2020b). It should be noted that bubble nucleation and growth have three-dimensional (3D) effects. However, when the bubble occupies the entire cross-sectional area which happens fast in a microchannel, the effects becomes to close to symmetric and can be seen as 2D. Compared to a 3D domain, the 2D domain can drastically reduce the computational processing cost. On that account, most researches are simulating this problem in 2D as it can be seen in Table 1.1. In the present work, the domain is specified as a rectangular channel with an aspect ratio way above eight which will be simulated in 2D. The height of the channel is referred to as the hydraulic diameter and is specified to 100 μm.

It is mentioned in Section 1.1 on page 2, that the instability of reverse flow can occur in microchannels, and one solution could be to give the channels a divergent shape. Therefore, divergent shaped microchannels will be investigated in the present work. This investigation will, however, not regard the instabilities but instead the influence the divergent shape has upon the bubble dynamics and the heat transfer.

The Computational Fluid Dynamic (CFD) solver of the present work is an OpenFOAM solver based on the Volume of Fluid (VOF) method. The VOF method is convenient for flow boiling simulations and is widely used as indicated in Table 1.1. The present solver is capable of simulating the nucleation of bubbles, and there will be no requirement of seeding a bubble. Instead, a cavity will be implemented as the nucleation site. The solver has the feature of dynamic mesh refinement implemented thus fewer cells are needed for the simulations, limiting the computational costs. Based on the abilities of bubble nucleation and dynamic mesh refinement, this solver is found applicable for the subject.

In this chapter, it has been set forth that flow boiling in microchannels has great potential in relation to the cooling of electronic components, but more knowledge is required on the topic. Based on the introduction and state of the art, it has been specified what is in the scope of the project. The scope has been further specified in the problem statement in the upcoming chapter.

Chapter 2

Problem Statement

Based on the introduction and the scope, the following problem statement has been formed. The problem statement is, furthermore, divided in to three more specific objectives and the methodology used to answer the problem statement and objectives is elaborated.

2.1 Problem Statement

How can flow boiling in a microchannel be numerically set up and simulated, and what influence does it have to vary the slope of the walls and obtaining a divergent channel?

1. How accurate is the solver compared to the exact solution of a 1D Stefan problem and to the Nusselt number correlations of a 2D film boiling problem?
2. What can be done to abbreviate the required simulation processing power without comprising the accuracy of the results?
3. How do the slope of the expanding channel and the Boiling number affect the heat transfer performance and the bubble dynamics of the microchannel?

2.2 Methodology

To answer the problem statement and the objectives, the following procedures are used:

First, flow boiling theory related to microchannels is elaborated in order to answer the objectives. This theory includes the onset of nucleation in cavities, flow boiling patterns, nucleate and convective heat transfer, and the related dimensionless numbers.

For the 1^{st} objective, two validation problems are made. To validate the solver and the phase-change model, a 1D Stefan problem is simulated. This problem has an analytic solution, and by comparison the accuracy of the numerical results are analysed. Furthermore, the more complex 2D film boiling problem is solved. Here the accuracy of the numerical result are analysed by comparison to prior studies and to the Nusselt number correlations presented by Berenson and Klimenko.

For the 2^{nd} objective, the basics of dynamic mesh refinement are first elaborated. Subsequently, dynamic mesh refinement based simulations are performed on the 2D film boiling problem. A grid independence study is performed for the simulations with a constant mesh and the simulation with dynamic mesh refinement enabled. The accuracy can be compared based on the results.

For the 3^{rd} objective, a parameter variation is performed upon the wall slope of the expanding channel and the Boiling number. Heat flux q is applied at the walls and the coolant is ethanol. A sketch of the microchannel with expanding walls and an implemented cavity is shown in Figure 2.1. Here L_{E} and d_{E} are the expansion length and expansion diameter, respectively. The slope of the walls are varied based on the two dimensionless numbers; $d_{\mathrm{h}}/d_{\mathrm{E}}$ and $d_{\mathrm{E}}/L_{\mathrm{E}}$ in the range of, respectively, 1.25 - 1.75 and 2 - 10. The Boiling number is varied from $1.25 \cdot 10^{-4}$ to $1.75 \cdot 10^{-4}$.

An initial simulation without any degree of expansion will also be performed for comparison. The parametric study is performed upon the heat transfer performance and the bubble dynamics.

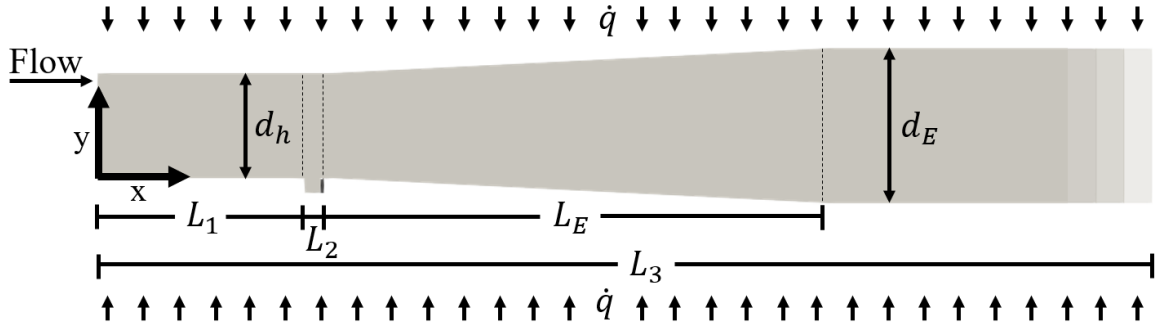

Figure 2.1: Sketch of the divergent shaped microchannel. Note that the channel will be longer.

The structure of the thesis is illustrated in Figure 2.2 to give a graphical overview.

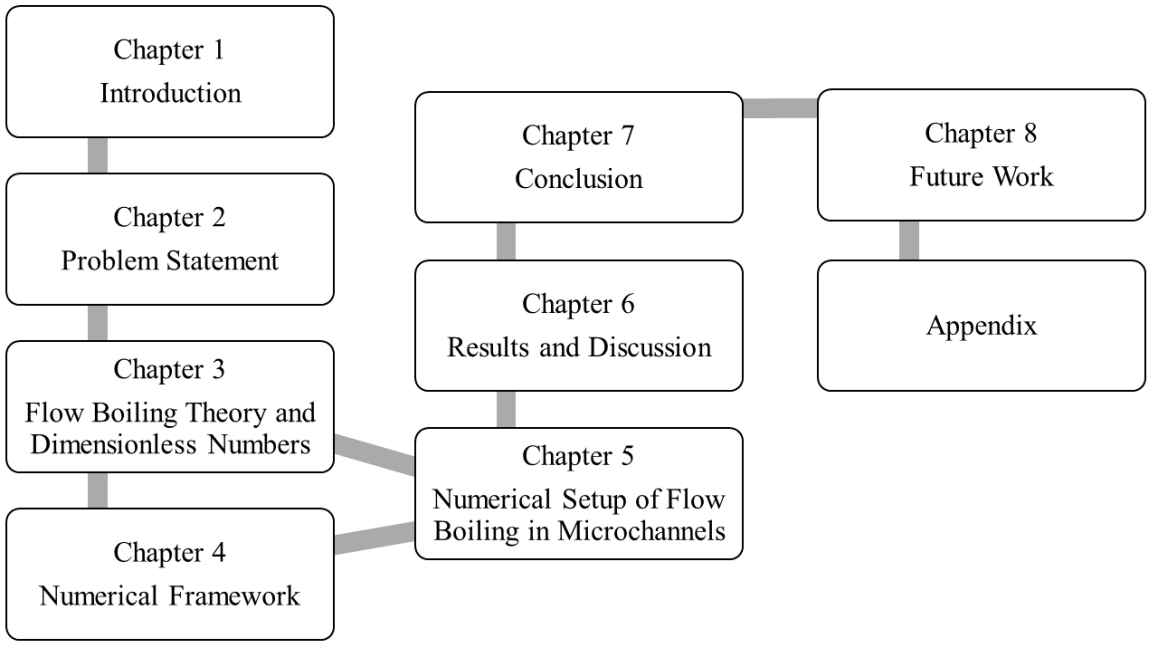

Figure 2.2: Structure of the thesis.

Chapter 3

Dimensionless Numbers and Flow Boiling Theory

In this chapter, the dimensionless numbers and the flow boiling theory related to microchannel flow boiling are elaborated. The theory includes the onset of nucleation in cavities, flow boiling patterns, and nucleate and convective heat transfer.

3.1 Dimensionless Numbers

The dimensionless numbers described in this section are significant for microchannel flow boiling and are used throughout the further project. Therefore, the following definitions of the numbers are applied throughout the project unless otherwise stated.

3.1.1 Boiling Number

The Boiling number B will be varied in the parameter investigation since it is an interesting number that accounts for the relation between the heat flux $\dot{q}$ and the mass flux $\dot{m}''$:

$$\mathrm{B} = \frac{\dot{q}}{H_{\mathrm{lg}}\, \dot{m}''} \tag{3.1}$$

with H_{lg} being the latent heat of vaporisation. An increase of the Boiling number indicates the evaporation of the flow boiling accelerates and if the Boiling number becomes too large, instabilities such as rapid dryout and reversed flow can occur. Conversely, if the Boiling number becomes too small, the bubble nucleation can be suppressed leading to no boiling. Many researchers have investigated the Boiling number in flow boiling in terms of keeping the heat flux or mass flux constant while varying the other (Jafari and Okutucu-Özyurt, 2016), (Ferrari et al., 2018b), (Megahed, 2011). The research is performed with a constant latent heat of evaporation and states that an increase in the Boiling number results in more elongated bubbles and a change in the detachment time.

3.1.2 Nusselt Number

In relation to describe the heat transfer performance of the flow boiling, the Nusselt number is convenient to use. The Nusselt number is a dimensionless number concerning the ratio of convective to conductive heat transfer across a surface as indicated in the following equation:

$$\mathrm{Nu} = \frac{h\, d_{\mathrm{h}}}{k} \tag{3.2}$$

with h being the convective heat transfer coefficient and k being the thermal conductivity. The Nusselt number can be reformulated based on the two equations:

$$\dot{q} = \frac{\dot{Q}}{A_\mathrm{w}} = h\,(T_\mathrm{w} - T_\mathrm{bulk}) \tag{3.3}$$

$$\dot{q} = -k\,\frac{\partial T}{\partial n}|_{n=0} \tag{3.4}$$

with $\dot{Q}$ being the heat transfer rate, A_w being the wall area, and T_w and T_bulk being the wall and bulk temperature, respectively. Equation 3.3 represents the specific form of Newton's law of cooling per unit area and Equation 3.4 represents Fourier's law of heat conduction per unit area. By setting Equation 3.3 and 3.4 equal and reformulating them in terms of the Nusselt number, the following Nusselt number expression is obtained (VDI, 2010):

$$\mathrm{Nu} = \frac{h\,d_\mathrm{h}}{k} = \frac{d_\mathrm{h}\,\frac{\partial T}{\partial n}|_{n=0}}{T_\mathrm{w} - T_\mathrm{bulk}} \tag{3.5}$$

Hence, the Nusselt number can be calculated based on either the the convective and conductive heat transfer or based on the specific temperatures and the temperature gradient. For flowboiling, T_bulk is dependent on the properties of both the liquid and gas. The bulk temperature can be calculated as the average bulk temperature across a specific cross-sectional area by:

$$T_\mathrm{bulk} = \frac{\sum_{i=1}^{n} U_{x,i}\,\rho_i\,T_i \Delta A_i}{\sum_{i=1}^{n} U_{x,i}\,\rho_i \Delta A} \tag{3.6}$$

with ρ being the density and U_x being the velocity in the x-direction.

3.1.3 Other Dimensionless Numbers

According to Li and Wu (2010), two-phase flow is dependent on the following four forces: viscous, inertia, surface tension, and gravity. However, due to the small diameter of a microchannel, the gravitational force becomes insignificant compared to the surface tension. This is indicated by the Bond number in Equation 3.7 which expresses the ratio between the gravitational and surface tension forces.

$$\mathrm{Bo} = \frac{g(\rho_\mathrm{l} - \rho_\mathrm{g})d_\mathrm{h}^2}{\sigma} \tag{3.7}$$

with g being the gravitational acceleration, σ the surface tension, ρ_l the density of liquid, and ρ_l the density of gas. Here the numerator represents the gravitational effects and the denominator represents the surface tension. It can be seen that the gravitational effects are dependent on the hydraulic diameter to the power of two. This indicates the gravitational effect becomes very small for a microchannel and thus the surface tension becomes the dominant force. This yields the two-phase flow is evenly distributed in the cross-section of the channel which will be elaborated in the upcoming flow pattern section.

In relation to the viscous, inertia, and surface tension forces, the Reynolds number and Capillary number are essential. The Reynolds number accounts for the inertia and viscous forces and the Capillary number accounts for the viscous and the surface tension forces. Equation 3.8 shows that the Reynolds number is defined based on the hydraulic diameter. This indicates that the inertia forces are less significant than the viscous forces for a microchannel compared to a conventional channel. The Capillary number described in Equation 3.9 can be seen as the relative effect of the viscous drag forces compared to the surface tension forces that are taking place across the interface. In flow boiling this number has an effect upon the shape of the bubbles since the viscous forces try to deform the bubble while the surface tension forces try to minimise the surface area of the bubble.

$$\mathrm{Re}_d = \frac{U_{\mathrm{in}}\, d_{\mathrm{h}}}{\nu_{\mathrm{l}}} \tag{3.8}$$

$$\mathrm{Ca} = \frac{U_{\mathrm{in}}\, \mu_{\mathrm{l}}}{\sigma} \tag{3.9}$$

with U_{in} being the inlet velocity, ν_{l} being the kinematic viscosity of liquid, and μ_{l} being the dynamic viscosity of liquid.

3.2 Flow boiling Theory

In this section, the characteristics of microchannel flow boiling are described. This description underlies the phase-change simulations of Chapter 4 and the microchannel flow boiling simulations of Chapter 5.

3.2.1 Onset of Nucleate Boiling and Cavities

Onset of nucleate boiling (ONB) refers to the transition from single- to two-phase that occur under nucleate and convection boiling. ONB can be divided into homogeneous and heterogeneous nucleation. In homogeneous nucleation, the formation of bubbles takes place in the liquid itself away from the walls. According to Whalley (1996), the liquid can be raised way above the saturation temperature before the nucleation takes place but it requires a very smooth surface with no irregularities. Thus the presence of homogeneous nucleation is only achievable under certain controlled environments. However if any cavities or irregularities are present, the bubble formation is much more likely to occur which is refered to as heterogeneous nucleation. In heterogeneous nucleation, the nucleation takes place at the interface between a surface and the liquid. In practical applications, the ONB is taking place in cavities in the surface roughness. Microscopic gas bubbles are entrapped in the cavities, and due to the heated surface, they grow up. Heterogeneous nucleation is the most common type of nucleation and is now further elaborated.

A cavity gets activated when the liquid temperature surrounding the bubble is at least equal to the saturation temperature. A cavity can also be activated if the evaporation forces from the heated surface to the bubble, dominates the condensation forces from the bubble to the subcooled surrounding liquid (Kandlikar, 2006). In Figure 3.1, ONB is illustrated for flow boiling with a cavity. According to Yin and Jia (2016), the evaporation forces include the heat flux from the wall q and the heat transfer from the superheated thermal boundary layer. Even though the temperature of inlet

fluid T_∞ is subcooled, the temperature of the thermal boundary layer T_{TBL} can become superheated due the heat flux from the wall. If the bubble height y_b is larger than the thermal boundary layer thickness y_{TBL}, the subcooled fluid of T_∞ gets in contact with the upper part of the bubble yielding condensation forces.

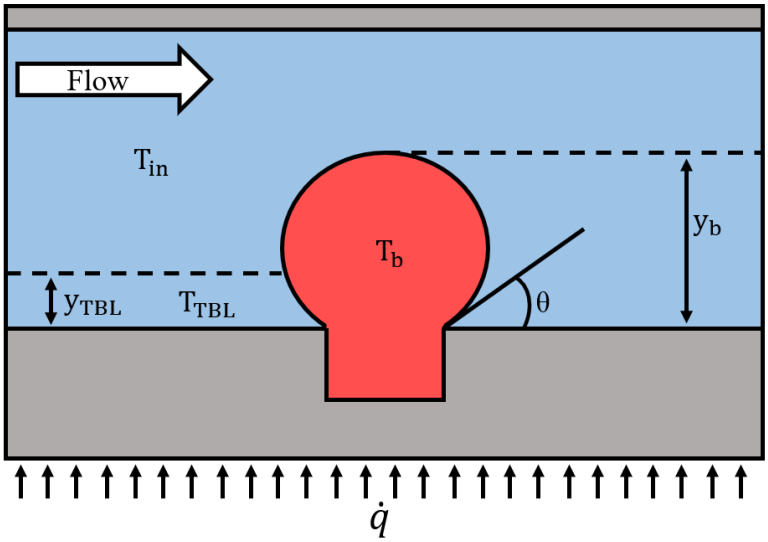

Figure 3.1: Heterogeneous nucleation illustration by the schematic of a bubble in a cavity with flow. Note that the transition from T_{TBL} to T_{in} is drawn abrupt for the illustration but is smooth in practical.

The thermal boundary layer thickness and temperature are both dependent on the flow velocity and thus the flow velocity influences whether a cavity is active. If T_{TBL} and y_{TBL} for instance are decreasing, the ONB process is delayed or suppressed (Saha, 2015). Therefore, for flow boiling it is crucial to have knowledge about the relation between the heat flux and the flow velocity.

The cavity shape and dimensions together with the contact angle, have an impact upon the bubble formation and bubble departure. According to Márkus and Házi (2012), the bubble formation is dependent on the cavity size with the cavity width being more significant than the cavity depth. The contact angle θ describes the angle between the bubble root and the surface. According to Liu et al. (2005), the contact angle has an influence upon the the ONB since it requires more heat to initiate the nucleation for at bubble with a smaller contact angle.

3.2.2 Two-Phase Flow Patterns

The flow patterns for microchannel flow boiling deviates from what is know from conventional flow patterns. One of the main reason for this is the low gravitational force compared to the surface tension force occurring in microchannels. The ratio between these two forces is as explained in Section 3.1.3 on page 11 referred to as the bond number. From equation 3.7 it can be seen that this bond number has a hydraulic diameter squared, meaning that the small hydraulic diameter occurring i microchannels has a major effect on the bond number.

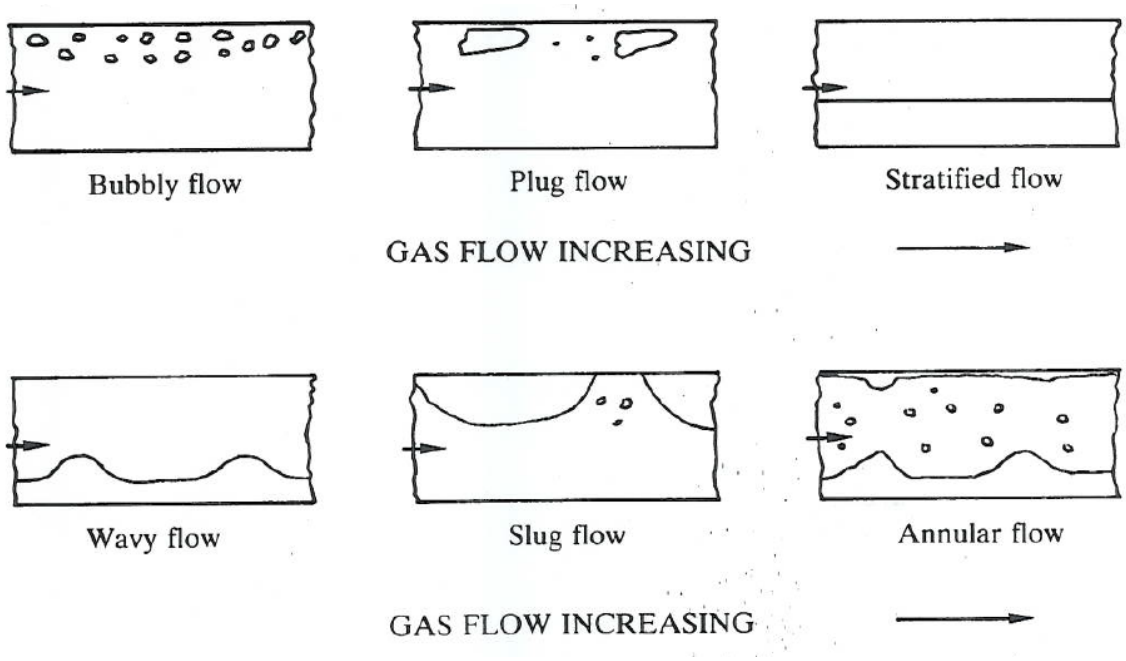

Figure 3.2: Illustration of flow patterns observed in conventional channels (Whalley, 1996).

In Figure 3.2 the different flow patterns for horizontal conventional channels is shown. The first flow regime is the bubbly flow where small gas bubbles are occurring in the liquid at the top half of the channel. The second flow regime is the plug flow in some literature also refereed to as slug flow. This flow is however recognised by small plugs/slugs of gas in the top half of the channel. The third flow regime is the stratified flow where the top half of the channel is gas and the bottom half is liquid this flow regime almost never occurs. Instead of a plane line as shown for the stratified flow a more wavy line would almost always be the case. This is also referred to as the wavy flow regime. The fifth flow regime is when the liquid waves becomes so large that they touches the top wall. The last flow regime seen in Figure 3.2 is the Annular flow where a liquid film layer is occurring in the top and bottom of the channel.

The major differences between the microchannel and conventional flow patterns is first of all that the gas in the microchannel is not moving towards the top of the channel as seen for the conventional flow regimes. This behavior is a result of the low bond number occurring in the microchannel. It also means that the stratified flow and the wavy flow pattern is non existing in microchannels (Qu et al., 2001). A second major difference is the much more confined space occurring in microchannels meaning that the gas plugs/slugs is filling almost the entire cross sectional area of the channel.

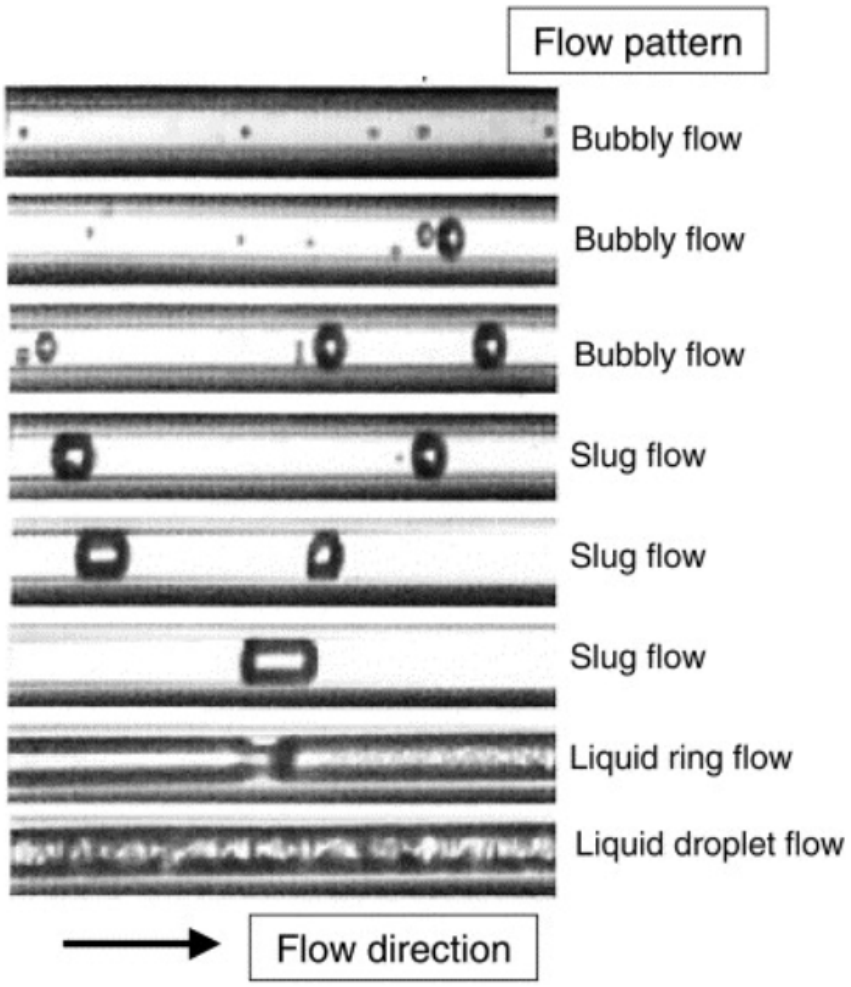

Figure 3.3: Flow pattern in microchannels experimental observed by (Serizawa et al., 2002).

Different flow regimes has been experimentally observed by many researchers. Some researcher even claims to have found new flow patterns in microchannels. These new flow patterns is however not always agreed upon (Saha, 2015). Serizawa et al. (2002) experimentally visualised different flow patterns for microchannel flow boiling which can be seen in Figure 3.3.
Here the bubbly flow is first visualised where multiple small bubble is observed in the middle of channel. The next flow regime observed is the plug/slug flow where the slug flow is filling up almost the entire cross sectional area. The third flow observed is the liquid ring flow. This type of flow pattern looks like the annular flow observed in the conventional channel expect here small rings of liquid is found around the gas. The fourth and last flow pattern observed in the microchannel is the liquid droplet flow where small droplets of liquid exist inside the gas. A overview of the different flow patterns can be seen in Table 3.1 where both the flow patterns from the conventional channel and the flow patterns observed by Serizawa et al. (2002) is described.

Table 3.1: A description of the flow patterns observed by Serizawa et al. (2002) in microchannels and the flow patterns described by (Whalley, 1996) in conventional channels.

Flow Regimes	**Microchannels**	**Conventional channels**
Bubble flow	Small bubbles in the whole cross section of the channel.	Small bubbles in the top half of the channel.
Plug/slug flow	The small bubbles have coalesced into a larger slug which fills most of the cross sectional area in the channel.	The small bubbles have coalesced into large plug bubbles placed in the top half of the channel.
Stratified flow	Not observed in Microchannel.	The top half of the channel is gas and the bottom is liquid. The interface between the liquid and gas is smooth. This flow pattern almost never happens.
Wavy Flow	Not observed in Microchannel.	The top half of the channel is gas and the bottom is liquid. The interface between the liquid and gas is wavy. The wave can become so large that it reaches the top of the channel also known as slug flow.
Liquid Ring flow	A gas core with liquid rings around it.	Not observed in Conventional channels.
Liquid droplet flow	A gas core with liquid droplets inside.	Not observed in Conventional channels.
Annular flow	The liquid forms a film layer between the gas and the wall small liquid bubbles can occur in the gas.	Here the liquid forms a film layer between the gas and the wall. Small liquid bubbles can occur in the gas. Note that the liquid film layer is thicker in the bottom half.

3.2.3 Heat Transfer in Flow Boiling

The heat transfer mechanisms of flow boiling in microchannels have not been well documented and are difficult to predict. Due to the difference in flow patterns of the micro- and conventional channel, the heat transfer mechanisms also differs. Many conventional flow boiling prediction models have been applied to predict the flow boiling and heat transfer in microchannels, but they have been found inadequate in the prediction (Saha, 2015). This indicates that more research is required to fully understand the topic of microchannel flow boiling. The heat transfer tendencies of microchannel flow boiling are, however, similar to the heat transfer mechanisms of flow boiling in conventional channels. Therefore, the following heat transfer elaboration is based on the theory of flow boiling in conventional channels.

The heat transfer mechanisms of flow boiling consist of nucleate boiling and convective boiling. In Figure 3.4, the heat transfer coefficient h can be to seen in relation to the flow boiling regime for, respectively, nucleate and convective boiling. It can be seen in the figure that nucleate and convective boiling coexist but they are dominant at different flow regimes.

The nucleate boiling is related to bubble nucleation as elaborated in Section 3.2.1 and is therefore dominant in the bubbly regime. As the liquid is saturated, the bubbles grow at the heated surface until detachment. As a bubble detaches, the bubble contributes with heat to the liquid while a new liquid flows towards the surface and a new bubble forms and so on. Even at subcooled inlet conditions nucleate boiling can occur. If the liquid is subcooled, bubbles are still capable of forming at the heated surface due a higher temperature in the thermal boundary layer. As the bubbles grows and reaches out of the thermal boundary layer and into the subcooled liquid, the bubbles condensate yielding a rise in the liquid temperature (Whalley, 1996). This can cause a collapse of the bubble and the pattern can repeat. As the bubbles detach and grow and eventually coalescence into the slug and the annular flow regime, a liquid film layer is created at the surfaces. Through these regimes the nucleate boiling is decreasing since less liquid is evaporating. At dryout completion, the nucleate boiling becomes insignificant.

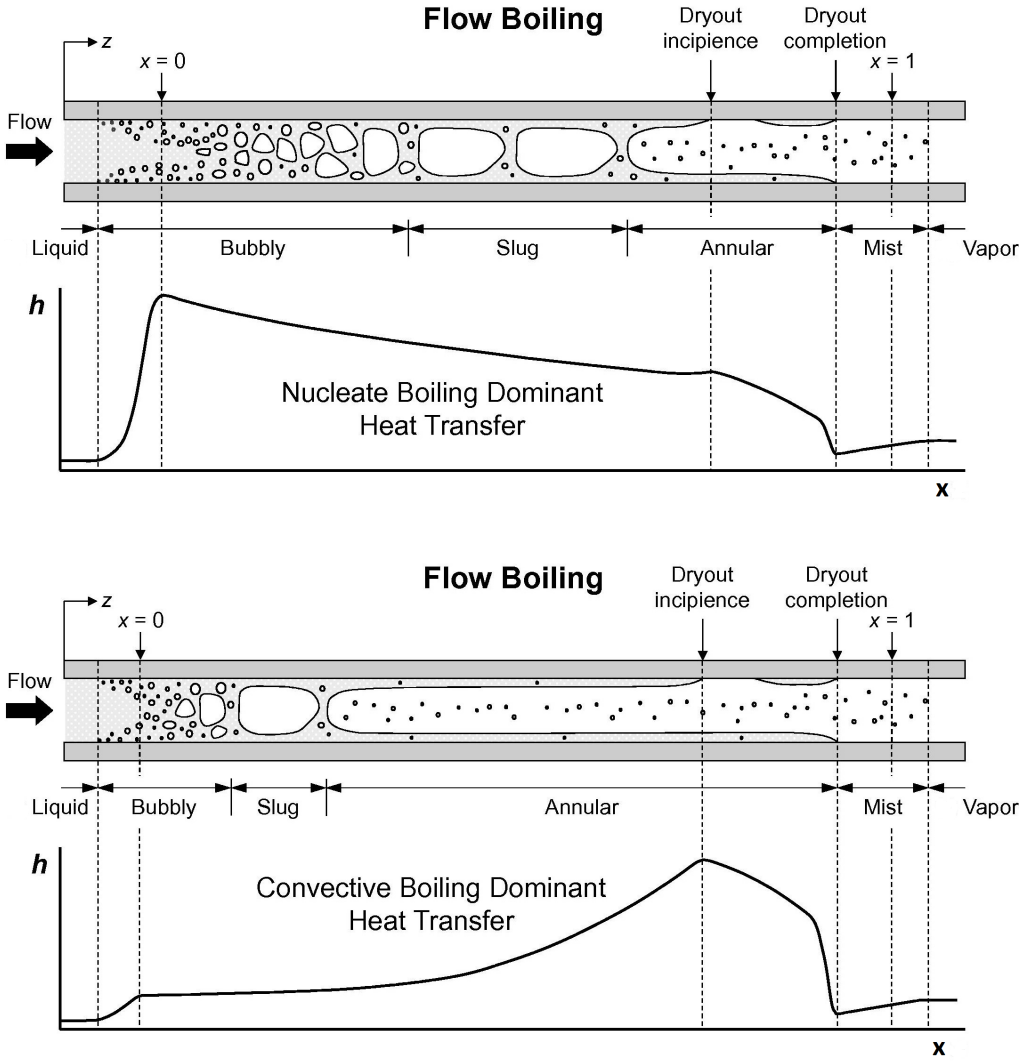

Figure 3.4: Sketch of flow boiling together with, respectively, the nucleate- and convective heat transfer coefficients (edited) (Kim and Mudawar, 2014).

At the inlet, only single-phase forced convection is taking place yielding a relative low heat transfer

coefficient. Going into the slug and annular regime the convective boiling increases. It can be seen that the convective heat transfer increases as the film layer thickness decreases. Many researchers have investigated the film layer of the slug flow regime and agreed on a reduced film layer thickness yields a higher heat transfer (Ferrari et al., 2018b), (Magnini and Matar, 2020a). As dryout spots occur, the film layer is at its thinnest yielding the convective boiling and also the combined heat transfer peaks. Subsequently, a complete dryout takes place causing a drastically decrease in the heat transfer coefficient. This is a result of the convective boiling now depends on single-phase forced convection which is low compared to the two-phase convective heat transfer.

Chapter 4

Numerical Framework

In this chapter, the numerical framework of the numerical solver is elaborated. This includes a description of the governing equations and phase-change models, the basics of the volume of fluid (VOF) method and dynamic mesh refinement. The solver and the implemented phase-change models are, furthermore, validated by comparison to a 1D Stefan problem and a 2D film boiling problem.

4.1 Governing equations

The solver of the numerical work is based on the three below listed governing equations derived from Navier-Stokes. The governing equations and the VOF method have been implemented into the OpenFOAM solver of the present work similarly to the procedure presented in work of Samkhaniani and Ansari (2017). First, the continuity equation is given by:

$$\frac{\partial}{\partial t}(\rho) + \nabla(\rho \mathbf{U}) = 0 \tag{4.1}$$

where t is the time, ρ is the density, and U is the velocity. The thermal properties in the three governing equations are determined based on Equation (4.5) which is elaborated in the upcoming section. The second governing equation is the momentum equation given by:

$$\frac{\partial(\rho \mathbf{U})}{\partial t} + \nabla(\rho \mathbf{U}\mathbf{U}) - \nabla(\mu(\nabla \mathbf{U}^T + \nabla \mathbf{U})) = -\nabla P + \rho \mathbf{g} + \sigma K \nabla \alpha \tag{4.2}$$

where μ is the dynamic viscosity, P is the pressure, g is the the gravitational acceleration, σ is the surface tension, and α is the volume fraction of liquid. The interface curvature K is given by $K = -\nabla(\nabla\alpha/|\nabla\alpha|)$. The subscripts of l and g represent, respectively, liquid and gas. The third governing equation is the energy equation given by:

$$\frac{\partial}{\partial t}(\rho C_p T) + \nabla(\rho C_p U T) - \nabla(k \nabla T) = -\dot{m}''' H_{\mathrm{lg}} \tag{4.3}$$

where C_p is the specific heat capacity, T is the temperature, and k is the thermal conductivity. The enthalpy of vaporisation H_{lg} is implemented in the energy equation to account for the energy required to vaporise the liquid doing phase change. The volumetric mass flux rate $\dot{m}'''$ is solved using a phase-change model. Two phase-change models are implemented in the solver and they will be elaborated in a later section.

The schemes used to solve these equations are for the derivative term Euler which is a first-order, transient, implicit and bounded scheme. Then a Gauss linear scheme is used for the discretisation of the gradient term. Gauss upwind scheme has been used for the discretisation of the divergent

terms to ensure stability. To ensure that the Courant number stays below one, an adjustable time step has been implemented.

Since flow boiling is a two-phase problem, the thermophysical properties of the governing equations are specified depending on the specific phase. To take this in to account, the VOF method is used, and its basics are elaborated in the next section.

4.2 Volume of Fluid (VOF)

The numerical solver is based on the VOF method, which is a widely used method for interface tracking (Hirt and Nichols, 1981). The method uses a fixed grid technique and requires that the fluids are not interpenetrating. The method treats the two-phase system as a single-phase system with either the properties of gas or liquid (LIU, 2017). Hence, only one set of governing equations is solved in every cell, depending on the volume fraction. Solving for only one set of governing equations and an advection equation, the VOF method greatly reduces the required computational processing power. The volume fraction has to be solved to identify each phase separately, and it must sum to unity in each cell. The volume fraction is given by the liquid volume in the cell V_l to the cell volume V_C and can be solved by the advection equation:

$$\alpha(\mathbf{x},t) = \frac{V_\mathrm{l}}{V_\mathrm{C}} = \begin{cases} 1 & \mathrm{x} \in \text{Primary phase, cell is solely liquid} \\ 0 < \alpha < 1 & \mathrm{x} \in \text{Interface, cell contains both gas and liquid} \\ 0 & \mathrm{x} \in \text{Secondary phase, cell is solely gas} \end{cases} \tag{4.4}$$

In the present work, the primary and secondary phase represent gas and liquid, respectively, as Equation 4.4 states. The thermophysical properties for the primary and secondary phase, respectively, are assumed constant thus the system can be seen as incompressible. The properties at the interface are solved as an average value which is linearly dependent on the primary and secondary phase:

$$\Phi = \alpha\,\Phi_\mathrm{l} + (1-\alpha)\Phi_\mathrm{g} \qquad \Phi \in [k, \rho, \mu, C_p] \tag{4.5}$$

with Φ representing the thermal and transport properties.

A sketch of the principle of the VOF method can be seen in Figure 4.1. The figure illustrates the transition between the primary and secondary phase of a domain with a very coarse mesh. The interface is usually spread across two or three cells (LIU, 2017). Therefore, the interface can be positioned at various positions causing the interface to be smeared, as illustrated in Figure 4.1. Thus, it is crucial to apply a fine mesh in order to ensure a sharp interface when using the VOF method.

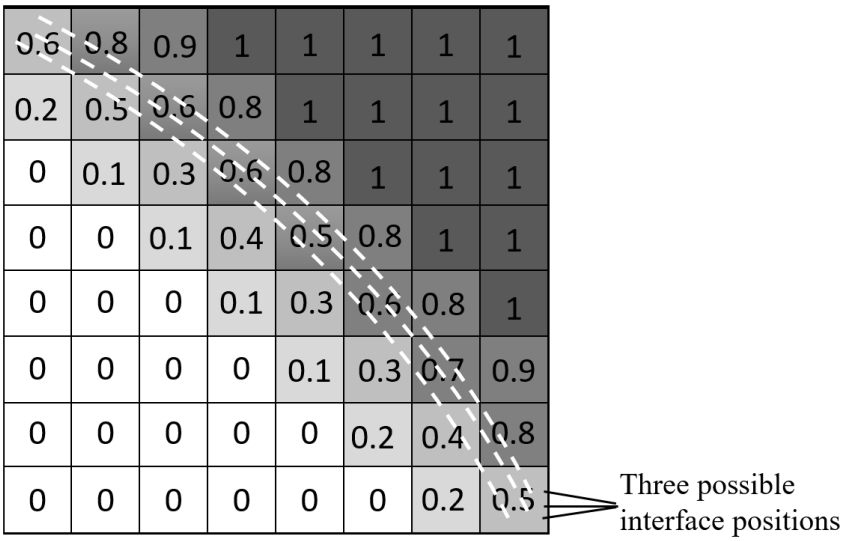

Figure 4.1: Illustration of the principles of the VOF method where the volume fraction is defined in each cell and three possible interfaces positions are drawn.

The interface is moving together with the flow of the fluid. Therefore, the volume fraction is adjusted to keep track with the interface by deriving a transport equation for the volume fraction. This is done by implementing the density from Equation 4.5 into the continuity equation ((4.1)) which can be rearranged to Equation 4.6. The following derivation of the VOF method has been formulated based on the work of Samkhaniani and Ansari (2017).

$$\frac{\partial \alpha}{\partial t} + \mathbf{U}\nabla\alpha + \alpha\nabla\mathbf{U} = -\frac{\rho_g \nabla \mathbf{U}}{(\rho_l - \rho_g)} \tag{4.6}$$

The interface is also moving as a result of the mass transfer of evaporation or condensation. Thus, the mass transfer of phase-change is implemented into the local continuity equation (4.1) for, respectively, the liquid and the gas phase:

$$\frac{\partial}{\partial t}(\rho_l) + \nabla(\rho_l \mathbf{U}) = -\dot{m}''' \tag{4.7}$$

$$\frac{\partial}{\partial t}(\rho_g) + \nabla(\rho_g \mathbf{U}) = +\dot{m}''' \tag{4.8}$$

Here $\dot{m}'''$ represents the volumetric mass transfer of phase-change which will be elaborated in the upcoming section regarding phase-change models. Since both phases are defined as incompressible, the first term at the left side of Equation 4.7 and 4.8 equal zero. The remaining part of the two equations can be rewritten by applying the divergence theorem and using integral notation:

$$\int_l = \mathbf{U} n_l \, \mathrm{d}\, S_n = -\frac{\dot{m}}{\rho_l} \tag{4.9}$$

$$\int_{g} = \mathbf{U} n_g \, dS_g = + \frac{\dot{m}}{\rho_g} \tag{4.10}$$

with S and n being the surface and the normal vector for, respectively, gas g and liquid l. The combined surface can be found by summarising Equation 4.9 and 4.10:

$$\int_{S} \mathbf{U} n \, dS = -\dot{m} \left(\frac{1}{\rho_g} - \frac{1}{\rho_l} \right) \tag{4.11}$$

which differentiated gives:

$$\nabla \mathbf{U} = \dot{m}''' \left(\frac{1}{\rho_g} - \frac{1}{\rho_l} \right) \tag{4.12}$$

By implementing Equation 4.12 into Equation 4.6, the transport equation for the volume fraction is expressed as:

$$\frac{\partial \alpha}{\partial t} + \mathbf{U} \nabla \alpha = -\dot{m}''' \left[\frac{1}{\rho_l} - \alpha \left(\frac{1}{\rho_l} - \frac{1}{\rho_g} \right) \right] \tag{4.13}$$

An additional divergence term; $\nabla(\alpha(1-\alpha)\mathbf{U}_c)$ is added into Equation 4.13. This term is implemented to minimise the smearing at the interface caused by compensation diffusive fluxes. Thus the transport equation is given by:

$$\frac{\partial \alpha}{\partial t} + \mathbf{U} \nabla \alpha + \nabla(\alpha(1-\alpha)\mathbf{U}_c) = -\dot{m}''' \left[\frac{1}{\rho_l} - \alpha \left(\frac{1}{\rho_l} - \frac{1}{\rho_g} \right) \right] \tag{4.14}$$

where $\mathbf{U}_c$ represents the compressive velocity given in Equation 4.15. The compressive velocity is calculated for the interface in the normal direction to avoid dispersion.

$$\mathbf{U}_c = min\left(C_a |U|, max(|U|)\right) \frac{\nabla \alpha}{|\nabla \alpha|} \tag{4.15}$$

The compressive factor C_a [-] [m/s] has purpose of controlling the compression flux. The factor should be in the range of 1 to 4.

4.3 Phase-Change Models

Two phase-change models are built into the present solver. These are the Tanasawa and Lee model, which are two widely used models in relation to phase-change simulations (Kharangate and Mudawar, 2017). Both models are elaborated in this section in order to be tested in the upcoming validation section. Based on a comparison, the phase-change model with the highest accuracy will be selected and implemented in the further simulations.

4.3.1 Tanasawa Phase-Change Model

In 1953 Schrage (1953) proposed a model for the mass flux of phase-change based on the interfacial jump in temperature and pressure across the interface $T_{\text{sat}}(P_{\text{l}}) = T_{\text{l}} \neq T_{\text{sat}}(P_{\text{g}}) = T_{\text{g}}$ and the evaporation γ_{e} and condensation γ_{co} coefficient [-]:

$$\dot{m}'' = \frac{2\gamma}{\gamma}\sqrt{\frac{M}{2\pi R}}\left[\gamma_{\text{c}}\frac{P_{\text{g}}}{\sqrt{T_g}} - \gamma_e\frac{P_l}{\sqrt{T_l}}\right] \tag{4.16}$$

with R being the universal gas constant and M the molecular weight. The values of γ_e and γ_{co} ranges from 0 to 1 and is given by (Kharangate and Mudawar, 2017):

$$\gamma_{\text{e}} = \frac{\text{number of molecules transferred to vapour phase}}{\text{number of molecules emitted from liquid phase}} \tag{4.17}$$

$$\gamma_{\text{co}} = \frac{\text{number of molecules absorbed by liquid phase}}{\text{number of molecules impinging on liquid phase}} \tag{4.18}$$

thus a coefficient of 0 yields no evaporation or condensation, and a coefficient of 1 yields perfect evaporation or condensation.

The phase-change model proposed by Tanasawa (1991) builds on equation 4.16 together with further assumptions. Tanasawa assumes that the mass transfer of evaporation and condensation are equal and thus the equation uses a shared phase-change coefficient γ. Tanasawa further assumes that the interface temperature equals the saturation temperature, and the mass flux depends linearly on the temperature jump between the vapour and interface. The mass flux rate of phase-change is, according to Tanasawa, defined as:

$$\dot{m}'' = \frac{2\gamma}{\gamma}\sqrt{\frac{M}{2\pi R}}\frac{\rho_{\text{g}} H_{\text{lg}}(T - T_{\text{sat}})}{T_{\text{sat}}^{3/2}} \tag{4.19}$$

The volumetric mass rate is given by $\dot{m}''' = \dot{m}''|\nabla\alpha|$. The phase-change coefficient is hard to predict and is only known with a great uncertainty, even for common fluids. Marek and Straub (2001a) have investigated the phase-change coefficient for water and specified it to be in the range of $1{\cdot}10^{-3} < \gamma \leq 1$. Marek and Straub (2001b) states that the phase-change coefficient exceeds 0.1 for dynamically renewing water surfaces such as jets or moving films, while the coefficient is below 0.1 for quasi-static stagnant surfaces. Magnini et al. (2013a) who simulates flow boiling, found the best agreement to the analytic solutions by setting $\gamma = 1$. Hardt and Wondra (2008a) who both simulates the Stefan problem and the film boiling problem also uses $\gamma = 1$. The same value is defined in the present numerical simulations unless otherwise stated.

4.3.2 Lee Phase-Change Model

In 1980 (Lee, 1980) presented a semi-empirical phase-change model. The model is based on the assumptions of quasi-static conditions, and the mass transfer takes place at constant pressure. The model includes a condensation and evaporation equation for the volumetric transferred mass rate:

$$\dot{m}''' = r_{co}(1-\alpha)\rho_g \frac{T - T_{sat}}{T_{sat}}, \qquad \text{for condensation} \tag{4.20}$$

$$\dot{m}''' = r_e \alpha \rho_l \frac{T - T_{sat}}{T_{sat}}, \qquad \text{for evaporation} \tag{4.21}$$

where r_{co} and r_e are time relaxation parameters also referred to mass transfer intensity factors. These are empirical values and can be in the extensive range of 0.1 to 10^7 (Kharangate and Mudawar, 2017).

4.4 Dynamic Mesh Refinement

The solver used for the present work has, as before mentioned, implemented a feature called dynamic mesh refinement. This feature becomes very useful when simulating boiling problems since a two-phase problem often requires a fine mesh at the interface between the two phases. The dynamic mesh refinement feature makes it possible to have a coarse mesh in the regions where only one phase exist while having a fine mesh in the regions where the interface lies.

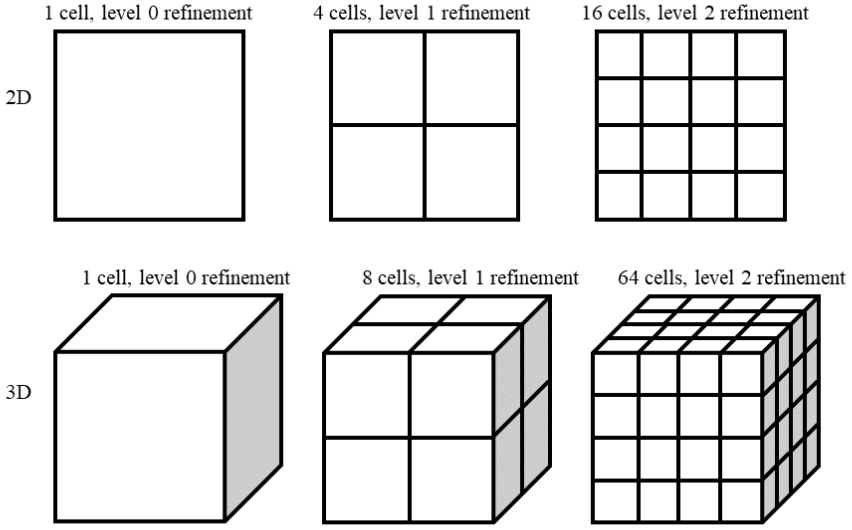

Figure 4.2: Illustration of the dynamic mesh refinement in 2D and 3D.

Figure 4.2 shows how the refinement is separating a cell into multiple smaller cells. It is possible to determine a specific level of refinement. Each level halves the cells in each dimension, meaning if 2D dynamic mesh refinement is applied, one cell is separated into four cells for each level of refinement specified. The refinement is defined to obey a selected property. For the present work, the volume fraction of liquid is chosen. The refinement is specified to take place whenever the volume fraction of liquid value lies between 0.999 and 0.001. The relation between the initial amount of cells and the refinement level will be included in the grid independence studies presented later in the present work.

4.5 Validation

In this section, two validation cases are made. First, the 1D Stefan problem is solved to validate the two phase-change model, and the most convenient model is selected for the further simulations. In the second case, the 2D film boiling problem is simulated and investigated, which includes grid independence tests and validation of the dynamic mesh refinement.

4.5.1 1D Stefan Problem

The 1D Stefan problem has become a benchmark when it comes to validation of phase-change models and has been numerical considered of among others; (Hardt and Wondra, 2008b), (Samkhaniani and Ansari, 2017), (Welch and Wilson, 2000), and (LIU, 2017). The 1D Stefan problem will be solved numerically and analytically and validated by comparison of the results. The numerical simulation will be performed for both the Tanasawa and Lee phase change solver, and the most accurate solver is chosen for the further project.

An illustration of the problem and the boundary conditions can be seen in Figure 4.3. Initially, the domain consists of saturated liquid with zero velocity. At the left wall, a constant temperature of 10 K superheat is defined, resulting in evaporation and a film layer of vapour is developed. As the hot wall continues to superheat the vapour, mass transfer is induced over the interface. Hence, the vapour stays motionless while the interface keeps moving towards the right wall. The right wall is defined as a surface with zero gradient and no-slip conditions. The length l of the domain is specified to 2 mm. The specific heat of the liquid and vapour is assumed equal ($C_{p,\mathrm{l}} = C_{p,\mathrm{g}}$). This assumption is made to ensure a constant mass flux in the energy equation throughout the phase-change.

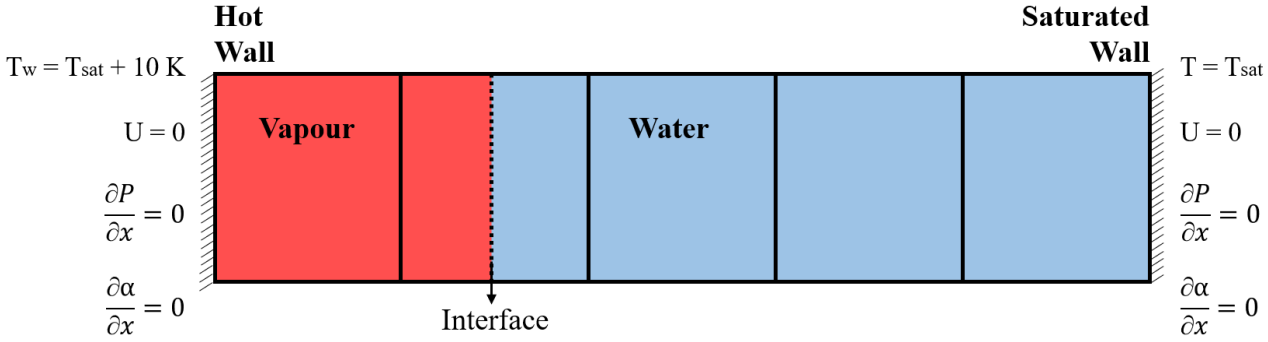

Figure 4.3: Sketch of the 1D Stefan problem and specified boundaries.

The problem has an analytic solution regarding the interface position $x_{\mathrm{i}}(t)$ and the interface temperature $T(x,t)$. The following analytic equations for the interface position and temperature have been presented by (Alexiades and Solomon, 1993) and later been rewritten by (Welch and Wilson, 2000).

$$x_{\mathrm{i}}(t) = 2\eta\sqrt{d_{\mathrm{g}}t} \tag{4.22}$$

$$T(x,t) = T_{\mathrm{w}} + \frac{T_{\mathrm{sat}} - T_{\mathrm{w}}}{\mathrm{erf}(\eta)} \,\mathrm{erf}\left(\frac{x}{2\sqrt{a_{\mathrm{g}}\, t}}\right) \tag{4.23}$$

with T_{w} being the temperature of the left wall, x being the position at the x-axis, and a_{g} being the thermal diffusivity of vapour. The subscript of i represents the interface and erf represents the error function with η being the solution to the transcendental equation:

$$\eta \exp\left(\eta^2\right) \,\mathrm{erf}(\eta) = \frac{c_{p,\mathrm{g}}\left(T_{\mathrm{w}} - T_{\mathrm{sat}}\right)}{\sqrt{\pi}\, H_{\mathrm{lg}}} \tag{4.24}$$

	ρ [kg/m^3]	ν [m^2/s]	k [W/m K]	C_p [J/kg K]
Liquid	888.2	$1.702 \cdot 10^{-7}$	0.6718	4 400
Vapour	5.129	$2.937 \cdot 10^{-6}$	0.03488	4 400
T_{sat} = 453.03 K; P_{sat} = 1 MPa; H_{lg} = 2 015 kJ/kg; σ = 0.04221 N/m				

Table 4.1: The thermal properties applied in the 1D Stefan problem at P_{sat} = 1 MPa.

First, the simulation is performed at under a pressure of 1 MPa and with the thermal properties shown in Table 4.1. This pressure has been chosen since it has proven great accuracy in the work of Samkhaniani and Ansari (2017). The interface position in the 1D simulations is defined to be at the cell where the volume fraction equals 0.5. The interface position as a function to the time can be seen in Figure 4.4 for both the numerical and analytical results. Here it can be seen that both the Tanasawa and Lee simulations show high convergence with the analytic solution. Tanasawa is, however, the most accurate. This is confirmed by Table 4.4 which also refers to the interface position. Here the interface positions at 50 s are listed together with the error between the analytical and numerical results. The simulations have been performed for cell numbers of 200, 400, and 800. This mesh independence study does not show completely convergence since the interface position keeps decreasing. The impact of increasing the number of cells is, however, minimal and thus the simulation of 800 cells have been found sufficient. For the fine mesh, it can be seen that the simulation with the Tanasawa and Lee model deviate with 0.25 % and 2.4 %, respectively, to the analytical solution.

Method	**Cell number**	**Interface position [mm]**	**Error [%]**
Analytical solution	-	1.8368	-
Tanasawa	200	1.8446	0.425
	400	1.8437	0.376
	800	1.8414	0.250
Lee	200	1.8863	2.695
	400	1.883	2.515
	800	1.8809	2.401

Table 4.2: The interface position for the Tanasawa and Lee method at 50 s with grids of, respectively, 200, 400, and 800 cells. The errors are calculated in relation to the analytic interface position.

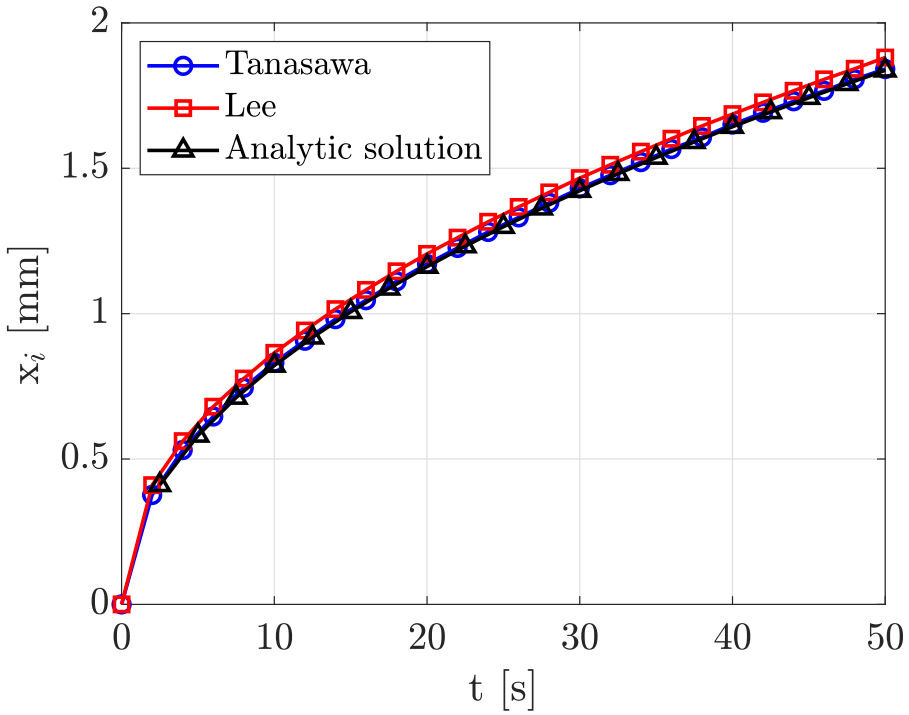

Figure 4.4: The interface position to the time for the Tanasawa method, the Lee method, and the analytic solution, respectively, at P_{sat} = 1 MPa.

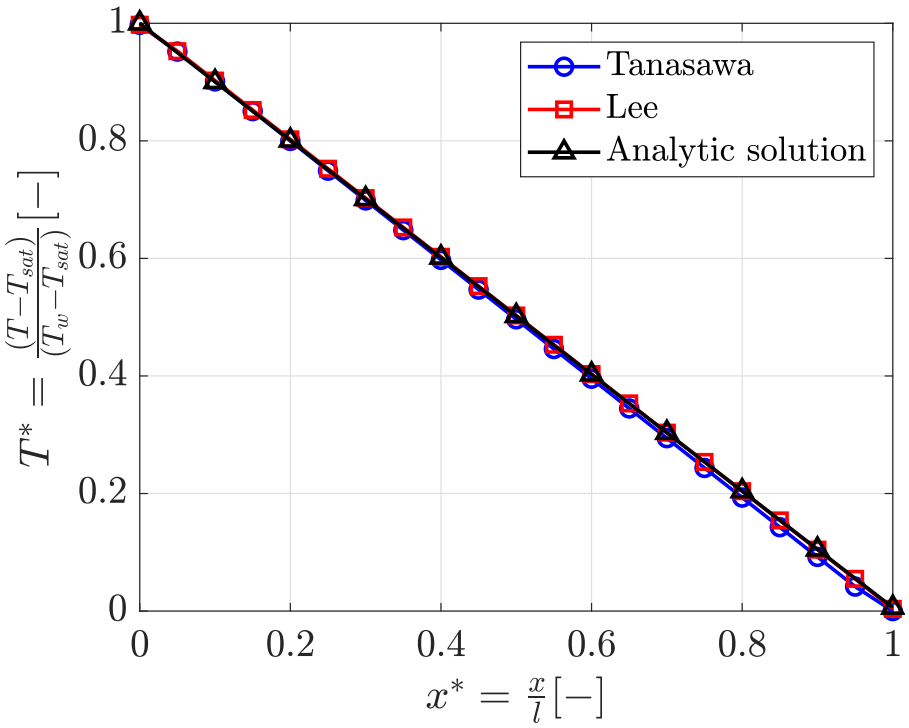

Figure 4.5: The dimensionless temperature to the dimensionless distance for the Tanasawa method, the Lee method, the and analytic solution, respectively, at P_{sat} = 1 MPa.

The dimensionless temperature T^* = (T - T_{sat}) / (T_w - T_{sat}) and dimensionless distance $x^* = x/l$ can be seen in Figure 4.5. Here it also can be seen that both Tanasawa and Lee are following the analytic

solution with high precision. Hence, it is determined that both models are within an acceptable range of the analytical solution, though with the Tanasawa model being the most accurate.

The microchannel flow boiling simulation in this project is performed at atmospheric pressure. This yields a much higher density ratio, and, therefore, the 1D Stefan problem is also tested by simulating at atmospheric pressure. The thermal properties of this simulation can be seen in Table 4.3. The simulation is performed with a grid of 800 cells and in Figure 4.6, the interface position is plotted to the time. It can be seen that both phase-change models are following the analytic solution with high precision, though with the Tanasawa model being the more accurate.

	ρ [kg/m^3]	ν [m^2/s]	k [W/m K]	C_p [J/kg K]
Liquid	959.1	$2.969 \cdot 10^{-7}$	0.6768	4 215
Vapour	0.5964	$2.063 \cdot 10^{-5}$	0.02465	4 215
T_{sat} = 373.15 K; P_{sat} = 101 325 kPa; H_{lg} = 2 256 kJ/kg; σ = 0.05891 N/m				

Table 4.3: The thermal properties applied in the 1D Stefan problem at P_{sat} = 101 325 kPa.

The dimensionless temperature to the dimensionless distance is shown in Figure 4.7. Again it is seen that both models are following the analytic solution but here but the Lee model is the more accurate. However, the Tanasawa model deviates with 0.033 at its most (at x^* = 0.5) which is in an acceptable range.

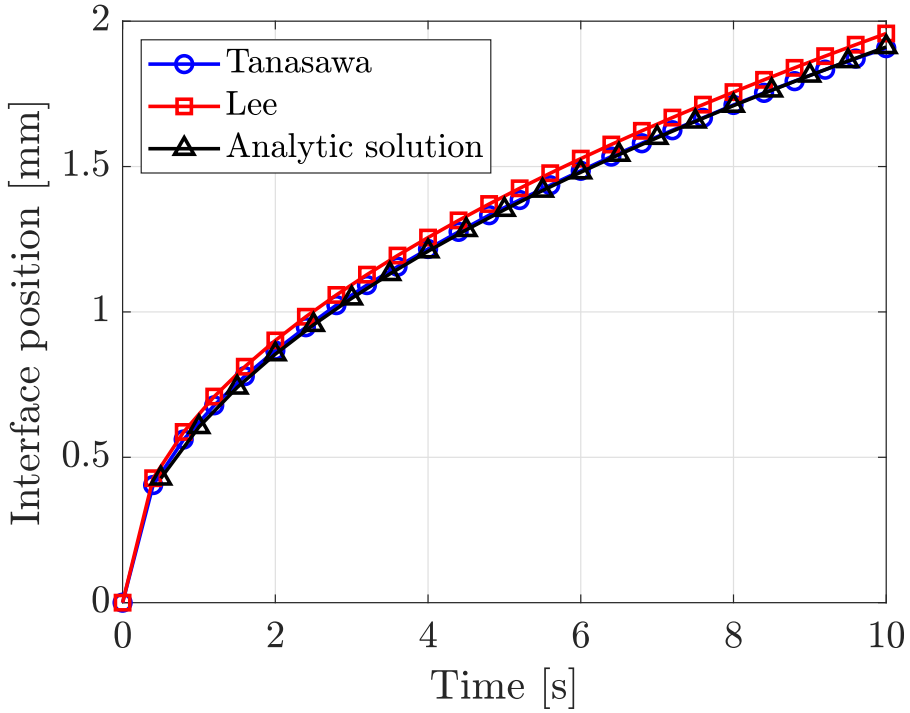

Figure 4.6: The interface position to the time for the Tanasawa method, the Lee method, and the analytic solution, respectively, at P_{sat} = 101 325 kPa.

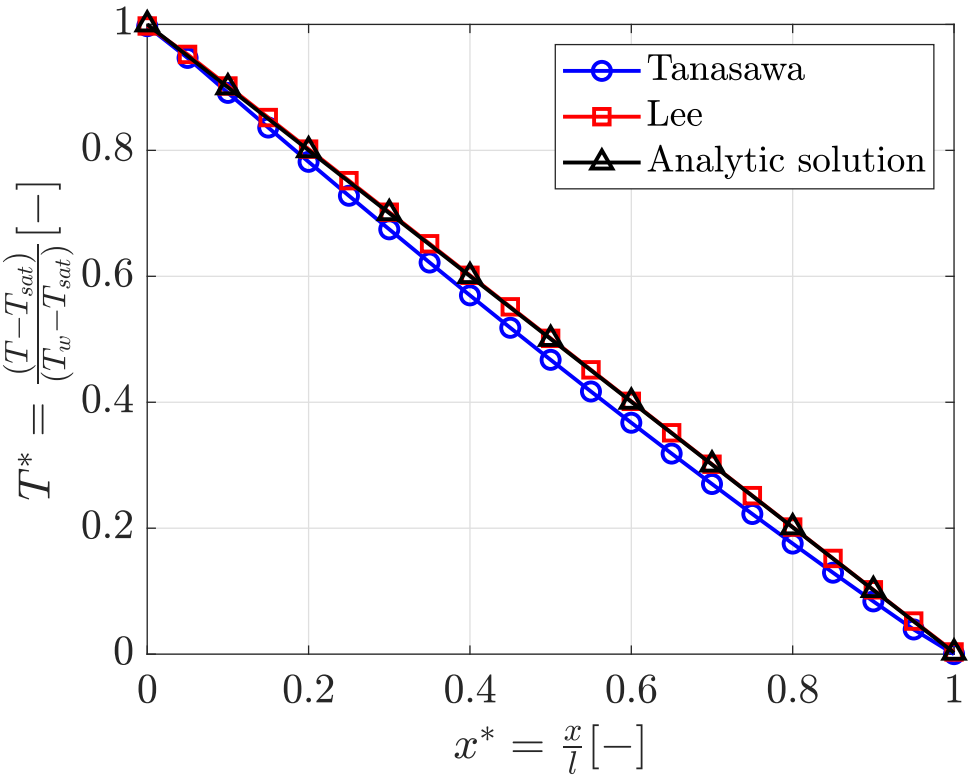

Figure 4.7: The dimensionless temperature to the dimensionless distance for the Tanasawa method, the Lee method, and the analytic solution, respectively, at P_{sat} = 101 325 kPa.

Based on the results, it can be concluded that both phase-change models are capable of accurately simulating the phase-change of the Stefan problem for both pressures. The Tanasawa model is the more accurate phase-change solver to simulate for the interface position as shown in Figure 4.4 and 4.6. In relation to the dimensionless temperature, the Lee model is the more accurate, but the Tanasawa model is still within an acceptable range with a maximum deviation of 0.033 in dimensionless temperature. Hence, the Tanasawa model is selected as the phase-change solver in the further project.

4.5.2 2D Film Boiling

The major regimes in pool boiling are convective boiling, nucleate boiling, and film boiling. The 2D film boiling problem concerns the thin film layer of vapour that is formed between a hot solid surface and saturated liquid. As evaporation of the liquid takes place at the hot surface, the liquid cannot come in contact with the surface and the film layer thickness continuous to increase. Due to the surface tension and the lower density of the vapour compared to the liquid, small vapour bubbles are initiated to form and rise. Thus, small waves are amplified at the interface, which is referred to as the Rayleigh-Taylor instability. As the bubbles keep rising, the bubbles will detach sooner or later depending on the thermal properties, and the heat flux applied from the solid surface. It can be seen in Figure 4.8a that the bubbles are detaching sooner and sequentially at low heat fluxes yielding quasi-periodic conditions. The film thickness is continually fluctuating, but a balance is obtained when the evaporation at the interface equals the vapour lost to bubble departure. In Figure 4.8b it can be seen that the bubbles do not detach at higher heat fluxes, and vapour columns are formed. As the columns rise, the top takes the shape of a mushroom.

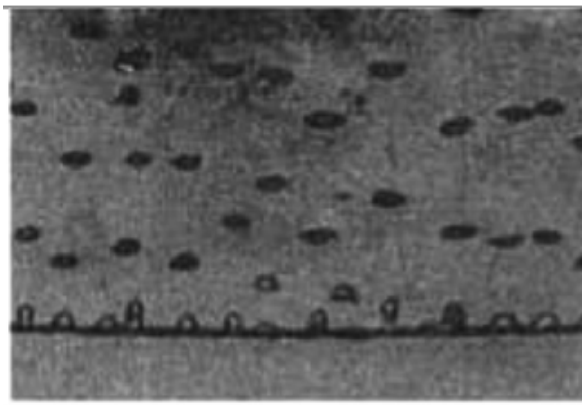

(a) Low heat flux at the solid surface $\dot{q}$ = 16.21.

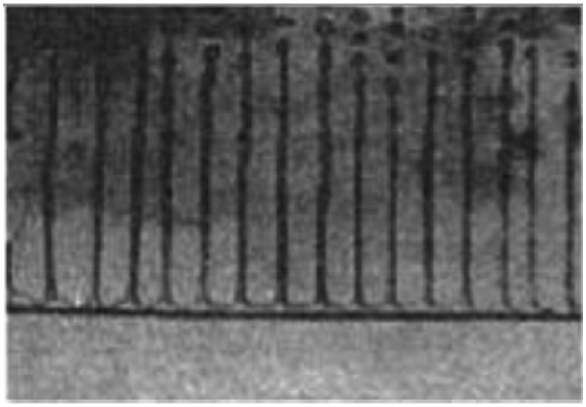

(b) High heat flux at the solid surface $\dot{q}$ = 27.10.

Figure 4.8: The bubble release pattern experimental observed by Reimann and Grigull (1975).

Film boiling is a complex phenomenon and has no analytical solution, but it can be validated by comparison to data of previous numerical solutions and to the Nusselt number correlation presented by Berenson.

Berenson Nusselt Number Correlation

In the pioneering study of Berenson he experimental measured the heat flux as a function of various temperature differences between the saturated liquid and the solid surface in order to obtain boiling curves for the relationship. Based on the experiments and assumptions, he derived a correlation for the heat flux and the Nusselt number of film boiling. The Nusselt correlation presented by Berenson has been widely accepted and used ever since (LIU, 2017), (Samkhaniani and Ansari, 2017), (Hardt and Wondra, 2008b), (Welch and Wilson, 2000) and is given by (Berenson, 1961):

$$Nu_{\mathrm{Be}} = 0.425 \left(\frac{\rho_{\mathrm{g}} \left(\rho_{\mathrm{l}} - \rho_{\mathrm{g}}\right) g \, H_{\mathrm{lg}}}{k_{\mathrm{g}} \, \mu_{\mathrm{g}(T_{\mathrm{w}} - T_{\mathrm{sat}})}} \right)^{1/4} \lambda^{3/4} \tag{4.25}$$

with λ representing the characteristic length of the wave:

$$\lambda = \sqrt{\frac{\sigma}{\left(\rho_{\mathrm{l}} - \rho_{\mathrm{g}}\right) g}} \tag{4.26}$$

Klimenko Nusselt Number Correlation

The correlation of Berenson assumes a laminar behaviour of the vapour film layer yielding the correlation is only proper at low heat fluxes. In order to obtain a correlation that is applicable at both low and high heat fluxes Klimenko (1981) has likewise considered the Rayleigh-Taylor instability. His Nusselt number correlation has been carried out based on assumptions similar to Berenson's. Furthermore, he assumes that the vapour film can be gravity-driven and turbulent at high heat fluxes yielding forced convection flow through the film layer. Klimenko has validated the correlation by comparison to experimental data, and the correlation shows an accuracy of $\pm$ 25 %. The Nusselt number correlation of Klimenko (1981) is expressed as:

$$Nu_{Kli} = \begin{cases} 0.19\mathrm{Gr}^{1/3}\,\mathrm{Pr}^{1/3}\,f_1 & \text{for } \mathrm{Gr} \leq 4.03 \cdot 10^5 \\ 0.0216\mathrm{Gr}1/2\,\mathrm{Pr}^{1/3}\,f_2 & \text{for } \mathrm{Gr} > 4.03 \cdot 10^5 \end{cases} \tag{4.27}$$

with the functions f_1 and f_2 being dependent on β:

$$f_1 = \begin{cases} 1 & \text{for } \beta \geq 0.71 \\ 0.89\beta^{-1/3} & \text{for } \beta < 0.71 \end{cases} \tag{4.28}$$

$$f_2 = \begin{cases} 1 & \text{for } \beta \geq 0.5 \\ 0.71\beta^{-1/2} & \text{for } \beta < 0.5 \end{cases} \tag{4.29}$$

The Grashof number Gr, the Prandlt number Pr, and β are given by:

$$\mathrm{Gr} = \frac{\rho_\mathrm{g}^2\, g\, \lambda^3}{\mu_\mathrm{g}^2} \left(\frac{\rho_\mathrm{l}}{\rho_\mathrm{g}} - 1 \right) \tag{4.30}$$

$$\mathrm{Pr} = \frac{C_{\mathrm{p,g}}\, \mu_\mathrm{g}}{k_\mathrm{g}} \tag{4.31}$$

$$\beta = \frac{C_{\mathrm{p,g}}(T_\mathrm{w} - T_\mathrm{sat})}{H_\mathrm{lg}} \tag{4.32}$$

Numerical 2D Film Boiling

In Figure 4.9 the computational domain, including the specified boundary conditions of the 2D Film boiling problem, is illustrated. The procedure of implementing the film layer and solve for the Nusselt number in OpenFOAM is based on the work of Samkhaniani and Ansari (2017).

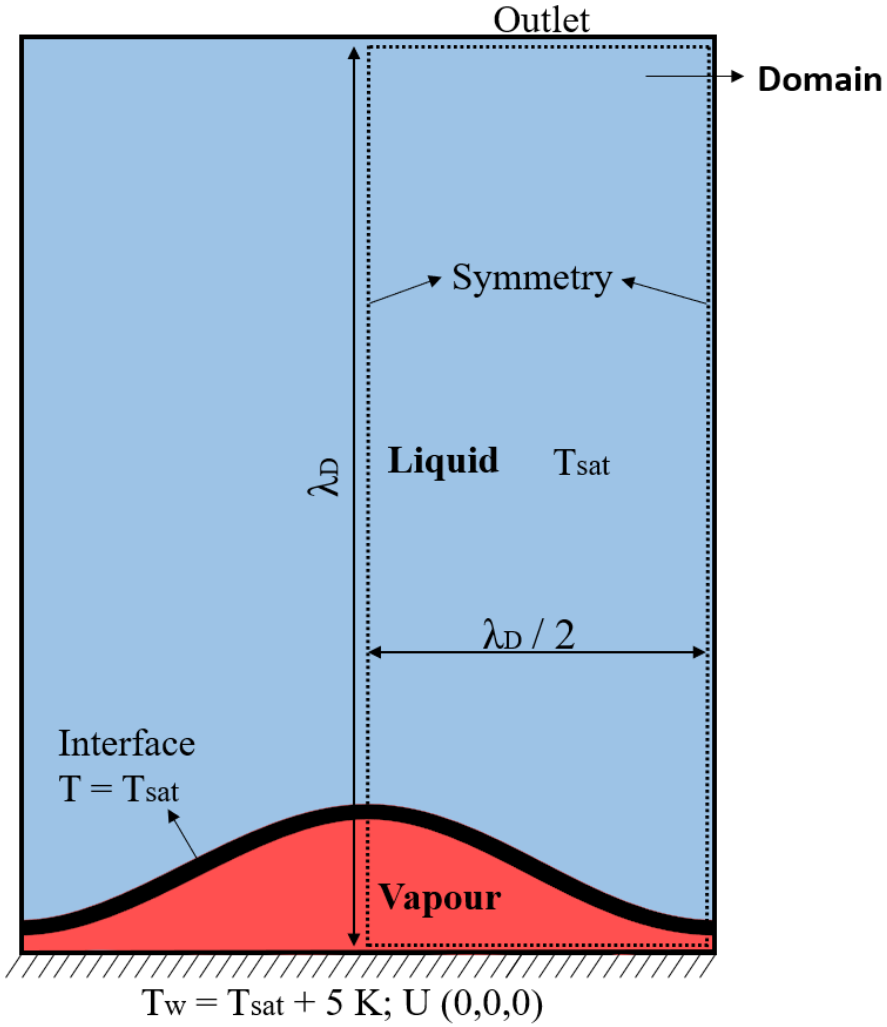

Figure 4.9: Sketch of the computational domain and specified boundaries.

In the initial time step of the numerical model, the film layer thickness y_g is implemented as:

$$y_{\mathrm{g}} = y_{\mathrm{u}} + \epsilon \, Cos\left(\frac{\pi \mathrm{N} x}{y_{\mathrm{D}}/2}\right) \tag{4.33}$$

with y_{u} being the unperturbed film thickness, ϵ the perturbation wave amplitude, and N the number of modes of perturbations.

$$y_{\mathrm{u}} = \frac{4.0}{128}\lambda_{\mathrm{D}}, \quad \epsilon = \frac{1}{128}\lambda_{\mathrm{D}}, \quad N = 1 \tag{4.34}$$

Here y_D is most dangerous unstable wavelength in a 2D domain corresponding to the wavelength at where the bubbles are most likely to rise and is given by:

$$\lambda_{\mathrm{D}} = 2\pi\sqrt{\frac{3\sigma}{g\left(\rho_{\mathrm{l}} - \rho_{\mathrm{g}}\right)}} \tag{4.35}$$

The film layer has been implemented based on the following constraints:

- The width of the domain is given by $y_D/2$.
- Every cell placed below interface at y_g is vapour (x=0).
- The temperature of the film layer is linearised between the saturation temperature of the saturated water and the constant temperature specified at the solid surface.

The local Nusselt number can be computed by:

$$Nu_\lambda = \frac{\lambda}{T_w - T_{sat}} \frac{\partial T}{\partial n}|_{n=0} \tag{4.36}$$

Validation of the 2D Film Boiling Simulation Near Critical Conditions

The numerical domain and the applied boundaries are illustrated in Figure 4.9. The domain has a width of $y_D/2$ and a height of y_D. The left and right boundary are defined with symmetry across the wall. Hence only half a domain needs to be simulated since it can be reflected, yielding less computational processing power required. The bottom boundary is defined as a wall with constant temperature and no-slip conditions. The top boundary is defined with the OpenFOAM boundary called inletOutlet. This boundary condition normally corresponds to a zero gradient but if any backward flow occurs into the domain, the boundary switches to become a fixed value. The Tanasawa phase-change model is used with the phase-change coefficient γ specified as 0.1. This value based on the work of (Marek and Straub, 2001b) who suggest a coefficient in this order of magnitude for experiments with quasi-periodic stagnant surfaces as described in section 4.3.1. A discussion of the phase-change coefficient can be found later in the section.

For the validation case, water is simulated near-critical conditions, P_{sat} = 21.9 MPa. This condition is chosen since it yields a low-density ratio resulting in more reliable simulations and because it is a commonly used condition for numerical film boiling simulations, e.g. (Guo et al., 2011) and (Samkhaniani and Ansari, 2017). The thermal simulation properties are shown in Table 4.4 are also based on the properties used in Guo et al. (2011) which are common properties for the case.

	ρ [kg/m^3]	μ [Pa s]	k [W/m K]	C_p [J/kg K]
Liquid	402.4	$4.67 \cdot 10^{-5}$	0.545	$2.18 \cdot 10^5$
Vapour	242.7	$3.238 \cdot 10^{-5}$	0.538	$3.52 \cdot 10^5$
T_{sat} = 646 K; P_{sat} = 21.9 MPa; $H_{lg} = 2.764 \cdot 10^5$ kJ/kg; $\sigma = 7 \cdot 10^{-5}$ N/m				

Table 4.4: The thermal properties applied in the film boiling validation case.

The film boiling simulation is shown in Figure 4.10 for multiple time steps and shows the bubble rise and departure from the film layer for the first and second period. The temperature at the bottom wall is 5 K above the saturation temperature $T_w = T_{sat}$ + 5 K. The simulation is performed with a grid of 240 x 480 cells, and the grid independence analysis is elaborated later in this section. In the figure, the red colour represents liquid, and the blue colour represents gas. With the implemented initial film layer (Equation 4.33), the first bubble is formed at the left side of the domain (centre in the figure due to symmetry), and after the departure, the remaining vapour neck returns to the bottom wall

caused by surface tension. Afterwards, the majority of the film layer shift toward the right (sides in the figure due to symmetry) and a new bubble rises. This pattern keeps repeating in steady-state since the evaporation of the film layer equals the vapour lost due to bubble departure. In relation to predicting the bubble shape, bubble departure pattern, and departure time, the present numerical tendencies show agreement with the tendencies of Guo et al. (2011), Kharangate and Mudawar (2020), and (Samkhaniani and Ansari, 2017).

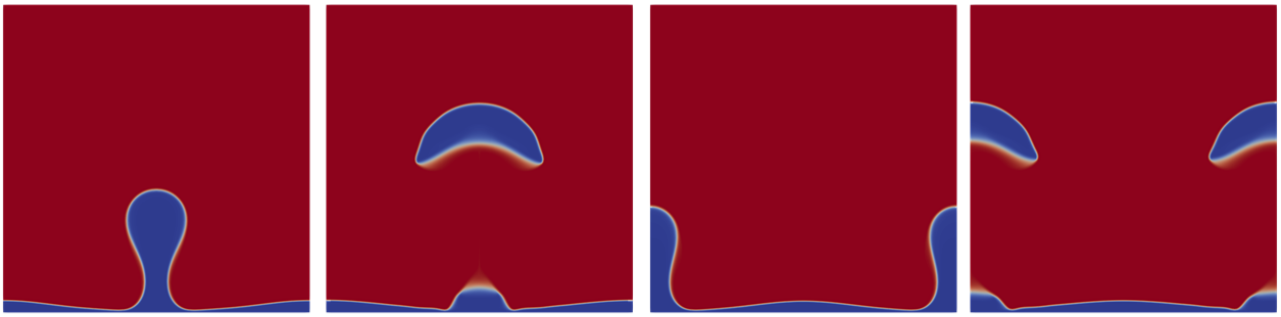

Figure 4.10: The bubble shape to different times. The simulation is performed under the conditions of P_{sat} = 21.9 MPa and $T_w = T_{sat}$ + 5 K.

The Nusselt number to the time can be seen in Figure 4.11 for the numerical simulation, the Berenson correlation, and the Klimenko correlation. The simulated local Nusselt number described in Equation 4.37 has been space-averaged to make the comparison more thorough:

$$\overline{Nu_\lambda} = \frac{\int_0^{y_D/2} \left(\frac{\lambda}{T_w - T_{sat}} \frac{\partial T}{\partial n} |_{n=0} \right) \mathrm{d}x}{y_D/2} \tag{4.37}$$

The Nusselt number depends on the thickness of the film layer. This is a result of the heat flux increases when the film layer thickness decreases and the Nusselt number is calculated proportional dependent on the heat flux. The summarised film layer thickness decreases when the vapour drives to fill and rise the bubble since the film layer at this point is stretched due to surface tension. This yields that the space-averaged heat flux, thus also the Nusselt number, are increasing. As the bubble detaches, the film layer flattens out and the summarised film layer thickness increases, yielding a decrease of the space-averaged heat flux and Nusselt number.

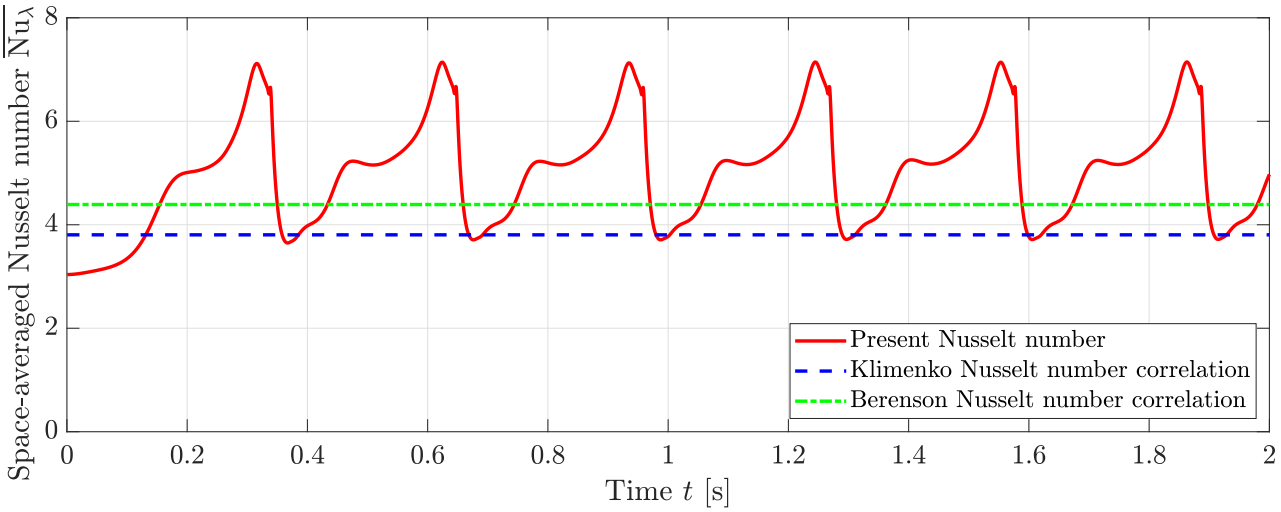

Figure 4.11: Space-averaged Nusselt number for the simulation compared to Nusselt number correlations of Berenson and Klimenko for a 2 s time interval, P_{sat} = 21.9 MPa and $T_w = T_{sat}$ + 5 K.

$$\langle \overline{Nu_\lambda} \rangle = \frac{1}{t_1} \int_{t_0+t_1}^{t_0} \overline{Nu_\lambda} \, \mathrm{d}t \tag{4.38}$$

This periodic Nusselt number tendency can be seen in Figure 4.11 where each period represents one bubble departure. Here $\overline{Nu_\lambda}$ has been time-averaged which is always done over full periods as seen in Equation 4.38 where t_0 is a certain start time and t_1 is a certain end-time of the period. For the numerical simulation presented in Figure 4.11, $\langle \overline{Nu_\lambda} \rangle$ is calculated for t_0 = 0.14 s and t_1 = 1.91 s and equals 5.01. The correlations presented by Berenson and Klimenko do not take the periodic trend into account, and they equal a Nusselt number of 4.39 and 3.81, respectively. This corresponds to an error of, respectively, 14 % and 31 % for the numerical results. Other researchers have obtained a deviation of 44 % in relation to the Berenson correlation (Samkhaniani and Ansari, 2017) and 11.2 % in relation the Klimenko correlation (Guo et al., 2011). Both correlations are built on simple assumptions and equations thus it is not expected to obtain a perfect fit. The deviation of the present numerical results is within the range of previous numerical results. Based on the comparison it is, therefore, determined that the numerical results are within an acceptable range in relation to the Nusselt number.

Based on a visual inspection in Figure 4.12, a grid independence study can be made upon the 2D film boiling problem. Samkhaniani and Ansari (2017) states that the bubble detachment time from the thin vapour neck depends on the grid size since the interface will break when the neck thickness becomes smaller than the specific resolved grid. As a result, the bubble detachment leaves sooner for a coarse mesh. In Figure 4.12, the film boiling simulation is shown for five meshes as the first bubble is rising at t = 0.31 s. It can be seen that the bubble of the coarse mesh simulation of 120 x 240 has already detached, and as the meshes become finer, the vapour film necks are wider, and the bubble has risen less. This is in accordance with the results of (Samkhaniani and Ansari, 2017). The bubble shape does not deviate from the grid of 210 x 420 to 240 x 480 cells. Therefore, a grid of 240 x 480 is found sufficient and is chosen for the film boiling simulations.

A simulation with dynamic mesh refinement enabled can be seen in Figure 4.13. The simulation has

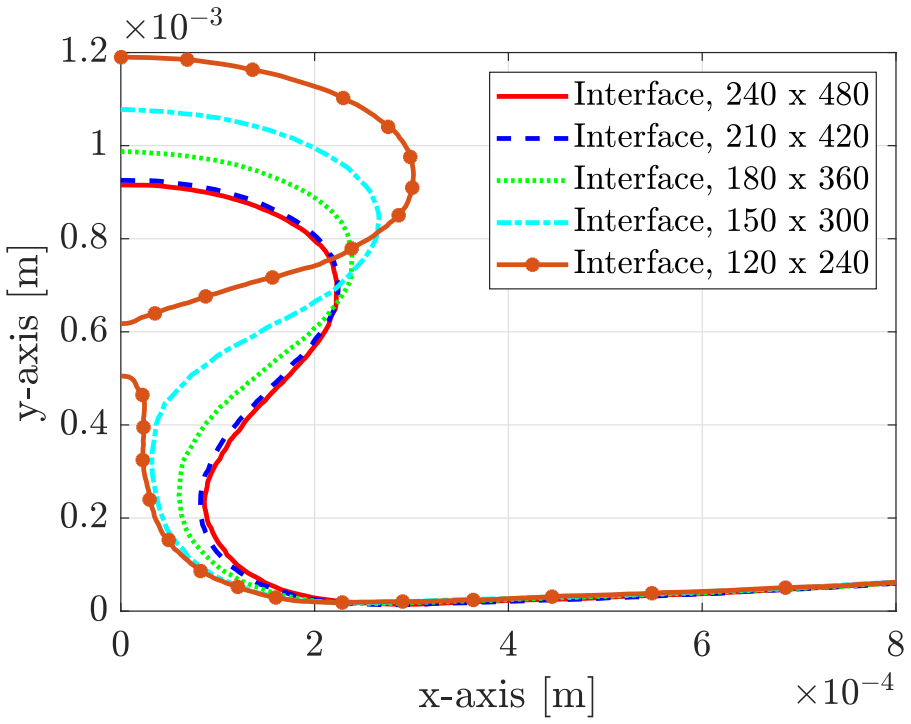

Figure 4.12: Bubble shape for the grids of: 240 x 480, 210 x 420, 180 x 360, 150 x 300, and 120 x 240 at time 0.31 s.

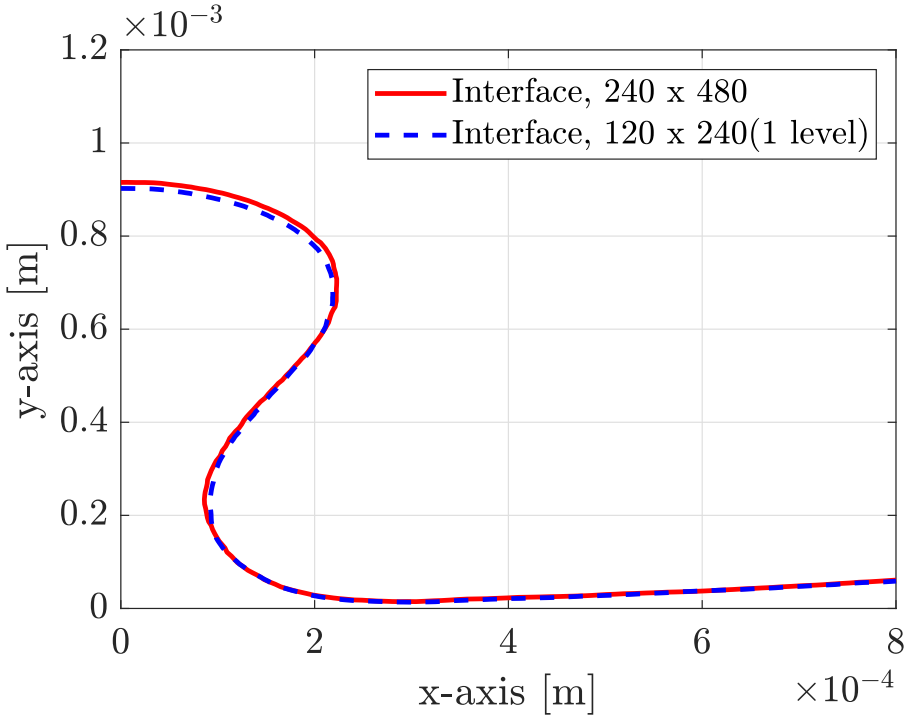

Figure 4.13: Bubble shape for the 120 x 240 grid with a refinement level of 1 and the 240 x 480 grid at time 0.31 s.

a grid of 120 x 240 and a refinement level of 1. Thus the simulations can potentially achieve a grid of 240 x 480 if every cell is refined. The simulation generates a bubble shape that is very similar to the simulation with the fine grid of 240 x 480 cells yielding full convergence is obtained.

	240 x 480	210 x 420	180 x 360	150 x 300	120 x 240	120 x 240 (level 1)
$\langle \overline{Nu_\lambda} \rangle$	5.176	5.183	5.194	5.203	5.206	5.193
% Error	-	0.12	0.34	0.51	0.56	0.31

Table 4.5: Grid independence study in terms of the space-averaged Nusselt number.

The grid indecency is also investigated upon the Nusselt number as shown in Table 4.5. Here $\langle \overline{Nu_\lambda} \rangle$ is calculated for the respective simulations together with the respective errors. The error is calculated with the 240 x 480 grid as the reference point. The table shows that the values of the 210 x 420 simulation and the 120 x 240 level 1 simulation are close to the values of the 240 x 480 grid simulation with respectively an error of 0.0003 % and 0.24 %. It is also seen that the error becomes more significant as the mesh becomes coarser. This is in accordance with the tendency of the visual inspection in Figure 4.12. Wherefore it is concluded that the dynamic mesh refinement is performing accurately thus it will be applied in the microchannel flow boiling simulations of this project.

The bubble release pattern depends on the magnitude of the heat flux as shown in Figure 4.8 by Reimann and Grigull (1975). It was also mentioned that vapour bubbles would detach at low heat fluxes, and the vapour will rise into mushroom-shaped columns at high heat fluxes. Therefore, a simulation with a constant wall temperature of $T_w = T_{sat} + 25$ K has been made as seen in Figure 4.14 together with the present simulation. The simulations show great agreement with the described heat flux tendencies.

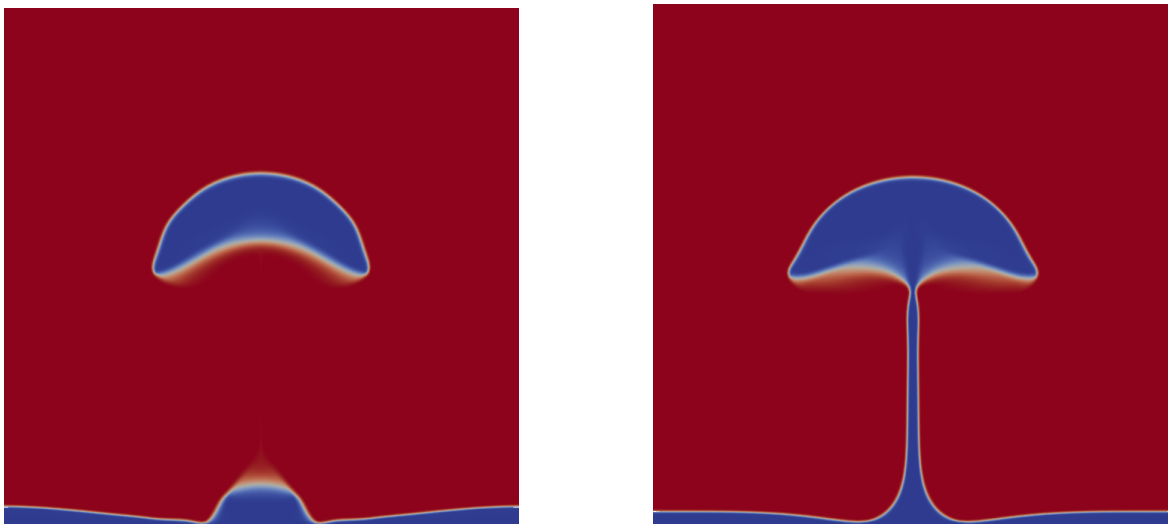

(a) Bubble shape and release pattern for $T_w = T_{sat} + 5$ K at 0.34 s. **(b)** Bubble shape and release pattern for $T_w = T_{sat} + 25$ K at t = 0.4 s.

Figure 4.14

Overall, it can be concluded that the numerical model is capable of simulating the expected tendencies of the 2D Film boiling problem. This is based on the visual bubble shape and bubble

departure inspection, the grid independence test, low and high heat flux comparison, and the Nusselt number comparison. The dynamic mesh refinement is proven to be applicable and accurate for phase-change simulations. Hence, the dynamic mesh refinement will be used in the upcoming microchannel flow boiling simulations.

Discussion of the Phase-Change Coefficient

In section 4.3.1 it was mentioned that a challenge of the Tanasawa phase-change model is to choose a suitable phase-change coefficient γ. In this film boiling case γ = 0.1 has been used. To investigate the influence of γ, $\langle\overline{Nu_\lambda}\rangle$ are calculated for the simulations of γ = 0.05, γ = 0.1, γ = 0.5, and γ = 1 as shown in Table 4.6. The error is calculated with the Berenson solution of 4.39 as the reference value. It can be seen that the tendency is that $\langle\overline{Nu_\lambda}\rangle$ becomes larger as γ increases. This is as expected since a higher γ yields a higher volumetric mass rate across the interface, corresponding to an enhanced evaporation. By looking into Figure 4.14 it can be seen that a more dominant heat transfer and evaporation lead to difficulties in the bubble detachment. Therefore, an even smaller γ could have led to an even more accurate Nusselt number for this simulation case. However, γ is difficult to specify and is individual from case to case as mentioned in section 4.3.1.

γ [-]	0.05	0.1	0.5	1
$\langle\overline{Nu_\lambda}\rangle$ [-]	5.079	5.176	5.325	5.390
Error [%]	15.66	17.89	21.26	22.28

Table 4.6: Time- and space-averaged Nusselt number for different phase-change coefficients specified in the Tanasawa phase-change model.

Chapter 5

Numerical Setup of Flow Boiling in Microchannels

Based on the numerical framework and the two validation cases, it has been proven that the solver is capable of correctly simulating for phase-change and that dynamic mesh refinement is applicable for the subject. In this chapter, microchannel flow boiling is simulated and investigated, but first, the simulation setup is elaborated.

5.1 Numerical Setup of the Domain

The flow boiling is simulated in a microchannel with a cavity as nucleation site. An illustration of the numerical setup can be seen in Figure 5.1 and the dimensions are listed in Table 5.1. The inlet is at the left boundary from where the fluid follows the positive x-direction to the outlet at the right boundary. The length of the channel is specified to L_3 = 15 d_h, which ensures that the bubble rise and detachment occur in the domain. The hydraulic diameter is specified as d_h = 100 μm which satisfies the definition of being a microchannel (Kandlikar, 2002). For the initial channel the hydraulic diameter is kept constant throughout the channel. However, in later simulations, the channel is expanding and thus the hydraulic diameter will vary. From the inlet to the cavity, the length is L_1 = 2 d_h. The cavity is shaped like a square and has a length of L_2 = 0.15 d_h. The channel inlet length L_1 = 2 d_h, the cavity length L_2 = 0.15 d_h, and the total length of the channel L_3 = 15 d_h are kept constant in all simulations.

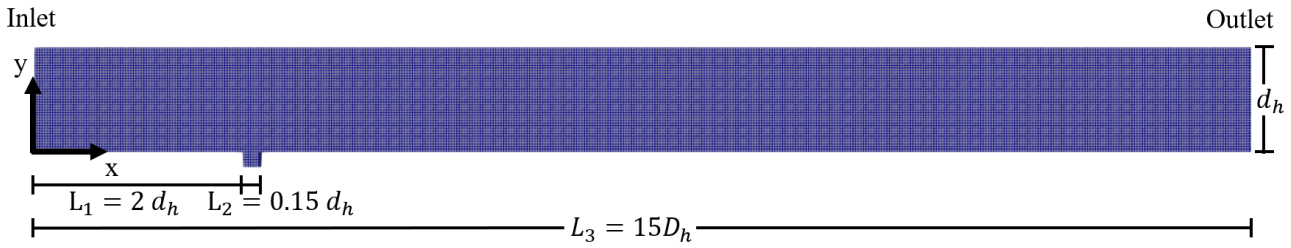

Figure 5.1: The domain and dimensions of the initial simulation.

Table 5.1: The hydraulic diameter, the dimensionless geometry sizes, and the number of cells.

d_h	Inlet length L_1	Cavity length L_2	Total length L_3	Cell number	Refinement level
100 μm	2 d_h	0.15 d_h	15 d_h	40 per d_h	2

For the initial case, the grid is defined uniform with 40 cells per d_h as listed in Table 5.1. Dynamic mesh refinement is applied with a refinement level of 2. The dynamic mesh refinement is applied since it can minimise the total number of required cells without comprising the accuracy of the results as it was shown in relation to the 2D film boiling in Figure 4.13 on page 36. Hence, the computational processing power can be reduced.

5.1.1 Boundary Conditions

In Figure 5.2, a sketch has been made of the front and back part of the microchannel to give a graphical overview of the boundaries. The front and back wall are defined with the OpenFOAM boundary called empty which means that the domain is not affected by the walls. This has been specified since the domain represents a rectangular channel with a high aspect ratio and thus the front and back walls should not affect the flow in the middle of the channel. The boundary conditions specified at, respectively, the bottom and top wall, inlet, and outlet can be seen in Table 5.2.

Figure 5.2: Sketch of the microchannel the front and back of the microchannel.

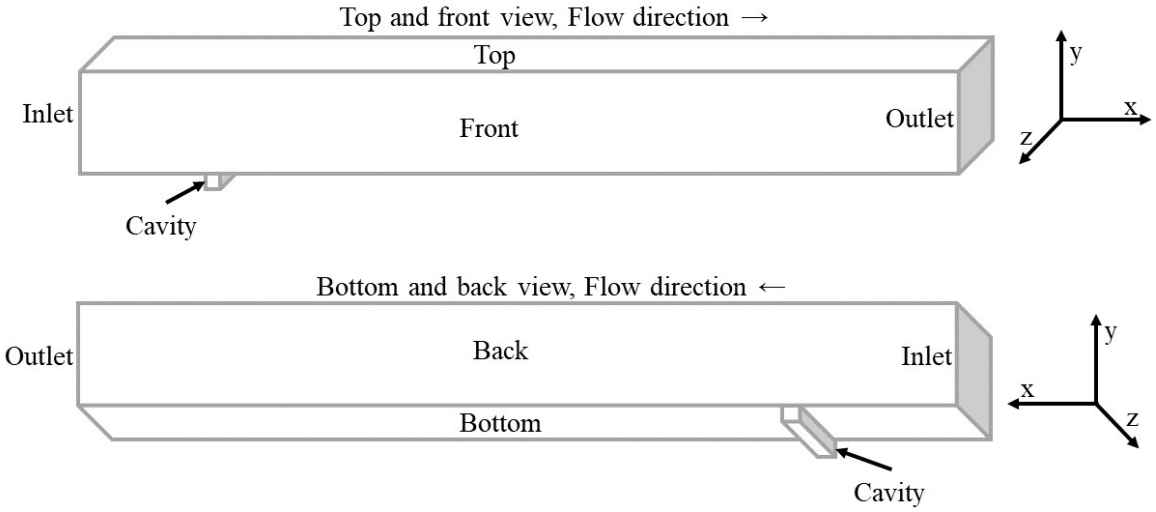

The boundary conditions are either defined with a constant value or a constant gradient. A constant value dictates that the properties specified at the boundary are kept constant for the cells adjoining the boundary. A constant gradient can be seen as the partial derived equations in the table. The value of the gradient is added to the cells adjoining the boundary. It can be seen that the domain is specified with a inlet temperature of 346.55 K and a velocity of 0.297 m/s. This corresponds to subcooled and laminar inlet conditions of, respectively, 5 K subcooling and a Reynolds number of approximately 50. The simulations are performed under atmospheric pressure and thus the outlet boundary is specified with a constant pressure of P = 101 325 MPa.

	Walls	Inlet	Outlet
T [K]	$\partial T/\partial n = 150\ 982$	346.55	$\partial T/\partial n = 0$
U [m/s]	(0 0 0)	(0.297 0 0)	$\partial U/\partial n = 0$
α [-]	$\partial \alpha/\partial n = 0$	1	$\partial \alpha/\partial n = 0$
P [Pa]	$\partial P/\partial n = 0$	$\partial P/\partial n = 0$	101 325

Table 5.2: The boundary conditions specified at, respectively, the top and bottom wall including the cavity, the inlet, and the outlet.

The bottom and top wall, including the cavity, are specified with no-slip conditions and and a constant temperature gradient. Notice that the specified temperature gradient of 150 982 K/m is only valid for the initial simulation. In the parametric investigation, the gradient will be varied

together with the Boiling number. At the top wall, bottom wall, and cavity a constant contact angle of 30° is specified. Because of the temperature gradient at the walls, the liquid will nucleate into gas bubbles. It is expected that the nucleation is going to take place in the cavity since this is the place with the highest surface-area-to-volume ratio. Furthermore, due to the no-slip condition at the walls and the setup of the cavity, the fluid in the cavity will be more or less stagnant, yielding higher temperatures can be obtained here.

5.2 Initial Simulation

The initial simulation is performed based on the numerical setup described in Section 5.1. The coolant in the microchannel is ethanol which is simulated under atmospheric pressure. The thermal properties of ethanol at this pressure can be seen in Table 5.3. Notice that the system is seen as incompressible and the properties of, respectively, liquid and gas, therefore, are constant. This assumption has been found acceptable since the latent heat of vaporisation ensures a stable temperature.

Table 5.3: The thermal properties of ethanol at saturation conditions.

Ethanol	ρ [kg/m^3]	ν [m^2/s]	k [W/m K]	C$_p$ [J/kg K]
Liquid	737.4	$6.156 \cdot 10^{-7}$	0.1541	$2.92 \cdot 10^3$
Gas	1.645	$6.356 \cdot 10^{-6}$	0.02056	$1.72 \cdot 10^3$
T_{sat} = 351.55 K; P_{sat} = 101 325 Pa; H_{lg} = 849.9 kJ/kg; $\sigma = 1.76 \cdot 10^{-2}$ N/m				

In Table 5.4, the Boiling number, Reynolds number, Bond number, and Capillary number are shown. The Boiling number ($B = \dot{q}/H_{\text{lg}}\dot{m}''$) is calculated based on the mass flux rate $\dot{m}''$ and heat flux rate $\dot{q}$. The mass flux rate and heat flux rate can be calculated based thermal properties of ethanol and the domain properties, and are given by:

$$\dot{q} = k_{\text{l}} \frac{\partial T}{\partial \text{n}} \tag{5.1}$$

$$\dot{m}'' = U\rho_{\text{l}} \tag{5.2}$$

Table 5.4: Dimensionless numbers defined for the inlet of the microchannel. Notice, that the Boiling number is specific for the initial case, and will be varied in later simulations.

Boiling Number	Reynolds number	Bond number	Capillary number
$1.25 \cdot 10^{-4}$	48.2456	0.0041	0.0076

The Reynolds number, Bond number, and Capillary number are defined based on the the inlet of the channel which are kept constant for all simulations. The Boiling number is specific for the initial case, and will be varied in later simulations.

In Figure 5.3, an illustration of the dynamic mesh refinement is presented. Here it can be seen that the cells at the interface are divided since this is where $0 < \alpha < 1$. Each cell is divided into 16 smaller cells as a result of the specified refinement level of two.

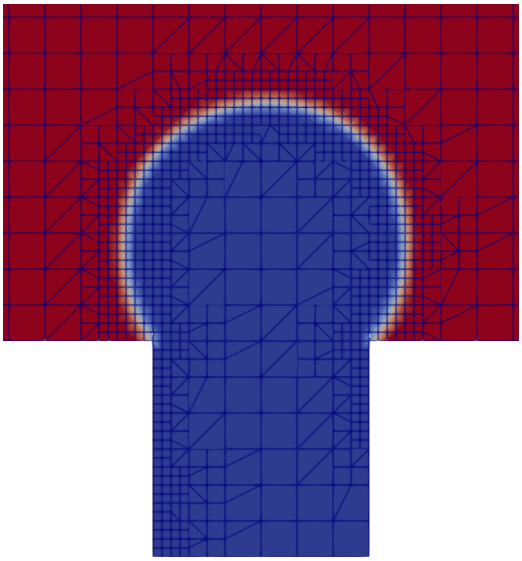

Figure 5.3: View of the cavity showing and the dynamic mesh refinement with a refinement level 2. Note zoom is applied.

First, the initial simulation is used to investigate the onset of the nucleation boiling. The present solver is capable of taking bubble nucleation into account, which is being confirmed in Figure 5.4. Here it can be seen that the bubbles after 10.9 ms nucleates in the corners of the cavity. This is as expected since this area has the highest surface area to volume ratio and a low velocity as mentioned in Section 5.1.1. The two bubbles grow until they coalescence after 33.6 ms, and the merged bubble continues to grow. At 44.6, the bubble occupies the entire cavity and starts to rise out of the cavity.

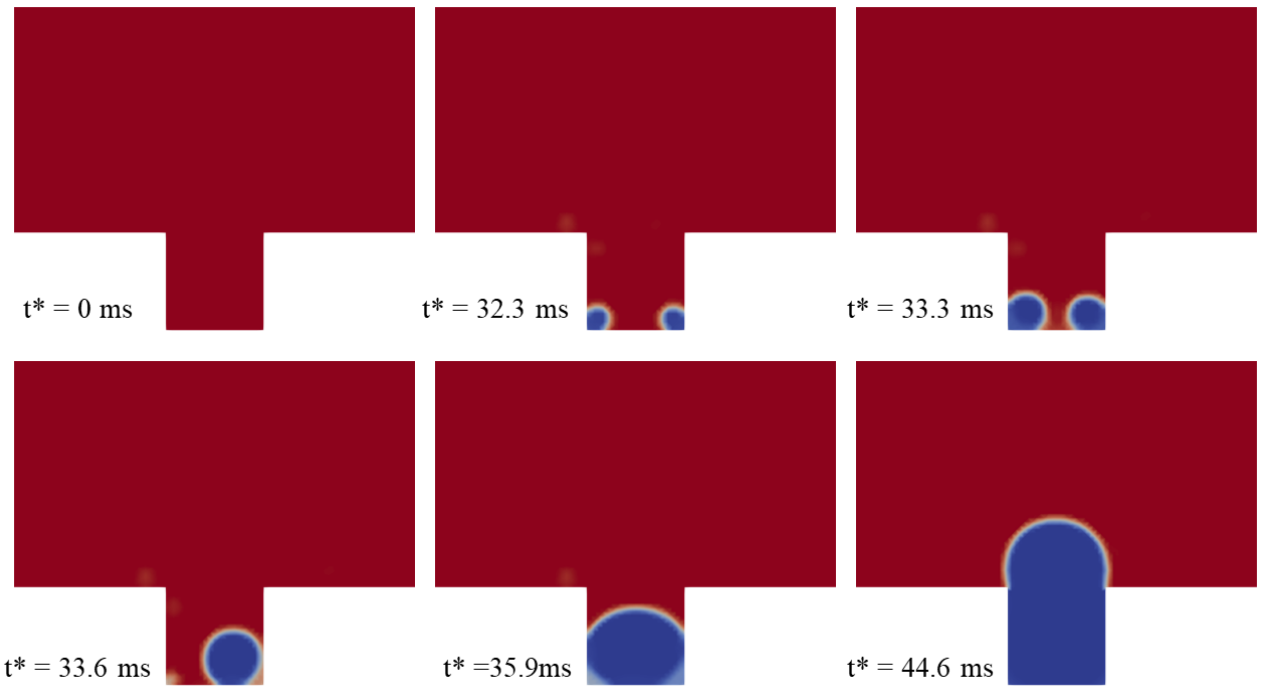

Figure 5.4: View of the cavity at different time steps showing the bubble nucleation and bubble coalescence. Note zoom is applied.

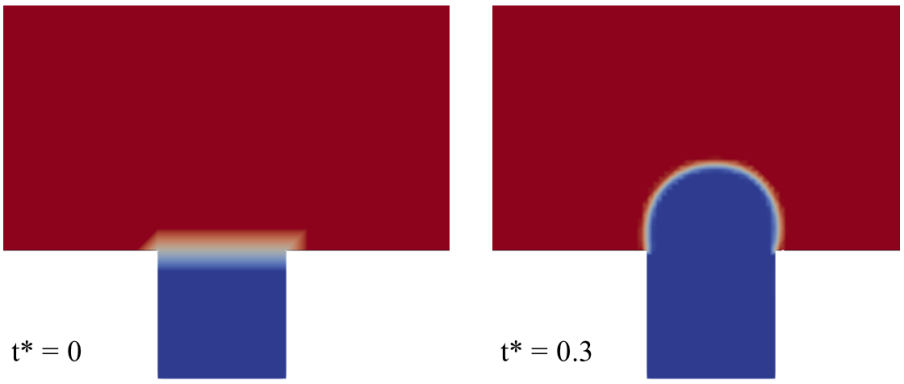

Figure 5.5: View of the cavity with a seeded bubble at t* = 0. Note zoom is applied.

These flow boiling simulations require a lot of computational processing time due to fine cells and small time steps are required. Therefore, to save computational processing time, a bubble has been seeded in the cavity as shown in Figure 5.5. The gas is seeded by using the setFields feature in OpenFOAM and has a specified temperature of saturation. It can be seen that the bubble shape after 0.3 corresponds to the bubble shape of the simulation with no seeded bubble after 44.6. Therefore, to save computational processing time, it is chosen to seed a bubble in all further simulations. Hence, the internal properties at $t* = 0$ are defined as shown in Table 5.5.

Table 5.5: The internal values specified for, respectively, the channel and the cavity at $t* = 0$.

	T [K]	U [m/s]	α	P [Pa]
Channel	346.55	(0.297 0 0)	1	101 325
Cavity	351.55	(0 0 0)	0	101 325

The microchannel flow boiling simulation of the initial case at t* = 16.3 is shown in Figure 5.6. At this time step, it can be that the first bubble has detached and is approaching the outlet while the second bubble is rising from the cavity.

Figure 5.6: View of the microchannel flowboiling for the initial case at t* = 16.3.

5.3 Parametric Study of Convergent Channels and the Boiling Number

The shape of the convergent channel will be determent by two dimensionless numbers; L_E/d_h denoted the expansion length and d_E/d_h denoted the expansion diameter. The two dimensionless numbers are based on Figure 5.7.

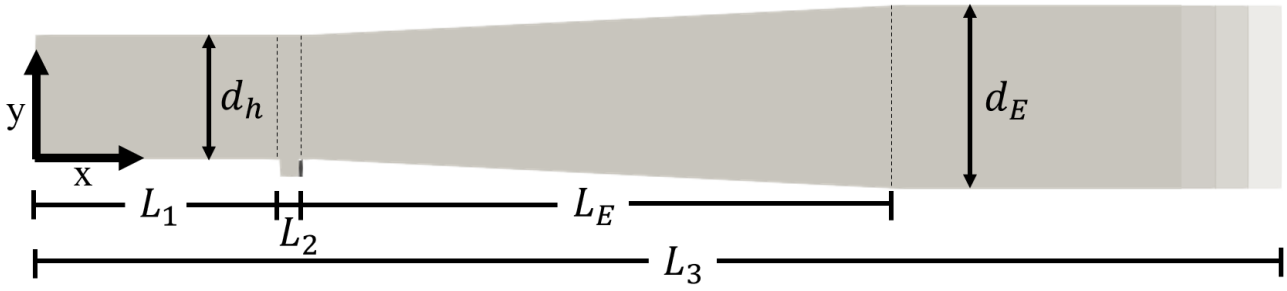

Figure 5.7: Sketch of the divergent shaped microchannel and the relevant dimensions for the dimensionless numbers L_E/d_h and d_E/d_h.

For all the divergent channel cases, the two Boiling numbers of respectively B == $12.5{\cdot}10^{-5}$ and B= $17.5{\cdot}10^{-5}$ will be simulated. In total 20 cases are simulated and they can be seen listed in 5.6.

Table 5.6: Description of the 20 cases.

	L_E/d_h	d_E/d_h	B	**Case nr.**
Cases with their different parameters	0	1	$1.25 \cdot 10^{-4}$	Case 1
			$1.75 \cdot 10^{-4}$	Case 2
	2	1.25	$1.25 \cdot 10^{-4}$	Case 3
			$1.75 \cdot 10^{-4}$	Case 4
		1.5	$1.25 \cdot 10^{-4}$	Case 5
			$1.75 \cdot 10^{-4}$	Case 6
		1.75	$1.25 \cdot 10^{-4}$	Case 7
			$1.75 \cdot 10^{-4}$	Case 8
	5	1.25	$1.25 \cdot 10^{-4}$	Case 9
			$1.75 \cdot 10^{-4}$	Case 10
		1.5	$1.25 \cdot 10^{-4}$	Case 11
			$1.75 \cdot 10^{-4}$	Case 12
		1.75	$1.25 \cdot 10^{-4}$	Case 13
			$1.75 \cdot 10^{-4}$	Case 14
	10	1.25	$1.25 \cdot 10^{-4}$	Case 15
			$1.75 \cdot 10^{-4}$	Case 16
		1.5	$1.25 \cdot 10^{-4}$	Case 17
			$1.75 \cdot 10^{-4}$	Case 18
		1.75	$1.25 \cdot 10^{-4}$	Case 19
			$1.75 \cdot 10^{-4}$	Case 20

5.3.1 Data Points and Data Processing

As previously stated, the heat transfer and the bubble dynamics will be investigated for the different cases. The heat transfer and bubble dynamics will be investigated in form of nose velocity, detachment time, bubble size, Nusselt number, and liquid film layer. In order to investigate these parameters, different tools are required. The bubble detachment time and bubble size are both visual inspected and compared. The bubble nose velocity, the Nusselt number, the bubble diameter, and the volume fraction of liquid are determined by implementing measuring points into the domain. The location of the specified measuring points are are illustrated in Figure 5.8.

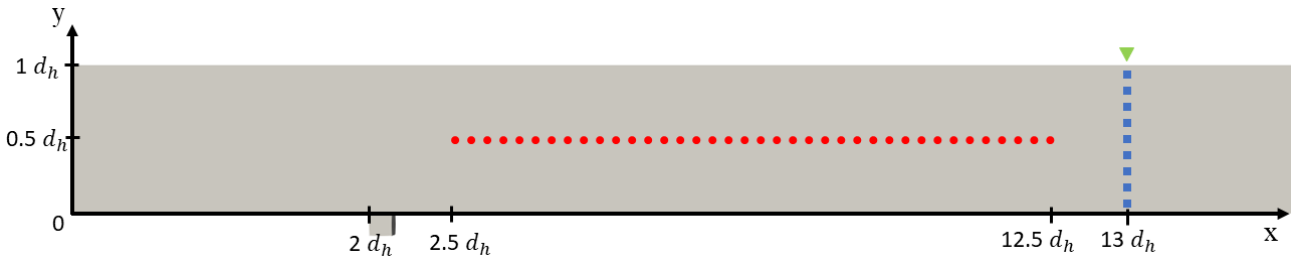

Figure 5.8: Illustration of the measuring points implemented in all domains.

The red line shown in Figure 5.8 illustrates measuring points which are placed in the middle of the channels y-axis y=0.00005 mm and then moves with the x-axis from $x = 2.5d_{\mathrm{h}}$ to $x = 12.5d_{\mathrm{h}}$. These measuring points measures the volume fraction of liquid and the time. This makes it possible to track the position of the interface on the x-axis at a given time and calculate the nose velocity of the bubble:

$$U_b = \frac{\Delta x_i}{\Delta t} = \frac{x_{i,2} - x_{i,1}}{t_2 - t_1} \tag{5.3}$$

The blue line seen in Figure 5.8 is measuring the points placed on the x-axis at $x = 13d_{\mathrm{h}}$ and in the y-direction from $y = 0$ to $y = 1d_{\mathrm{h}}$. These points measures the volume fraction of liquid, the velocity, and the temperature, which will be used to calculate the bulk temperature that is needed to further calculate the local Nusselt number. The Nusselt number is elaborated in Section 3.1.2 and the equation for the local Nusselt number can be seen in Equation 5.4. Here $\partial T/\partial y$ is the specified temperature gradient. In order to determine the wall temperature, some measuring points at the wall are also required. These measuring points are illustrated with the green triangle in Figure 5.8. The Nusselt number can be calculated by:

$$Nu = \frac{d_{\mathrm{h}} \, \frac{\partial T}{\partial n}|_{n=0}}{T_{\mathrm{w}} - T_{\mathrm{bulk}}} \tag{5.4}$$

where $\mathrm{T_{Bulk}}$ is the bulk temperature and is given by an average temperature of the measured points going across the channel:

$$T_{\mathrm{bulk}} = \frac{\sum_{i=1}^{n} U_{x,i} \, \rho_i \, T_i \Delta A_i}{\sum_{i=1}^{n} U_{x,i} \, \rho_i \Delta A_i} \tag{5.5}$$

Based on the implemented measuring points, it is possible to investigate the bubble dynamics and Nusselt number and perform a comparison of the different cases. This will be done in the next chapter.

Chapter 6

Results and Discussion

In this chapter, results from the cases mentioned in the previous section will be presented. However, only a sample of the results is shown, and the rest can be found in Appendix B. First, the two cases with no expansion are shown where the effect of the boiling number can be seen. Then a sample of the divergent channel cases where first the effect of the expanding length and expanding diameter upon the bubble dynamics is presented. Then the effect upon the Nusselt number and liquid film layer is shown.

6.1 Results for Case 1 and 2

Table 6.1: Key observations for Case 1 and 2 and their defining dimensionless parameters. The maximum dimensionless diameter and average dimensionless velocity are measured between $x = 2.5d_\mathrm{h}$ and $12.5d_\mathrm{h}$ at $y = 0.5d_\mathrm{h}$ in the microchannel domain.

	$L_\mathrm{E}/d_\mathrm{h}$	$d_\mathrm{E}/d_\mathrm{h}$	$\mathrm{B_{in}}$	Maximum dimensionless diameter	Average dimensionless velocity	Dimensionless detachment time
Case 1	0	1	$1.25 \cdot 10^{-4}$	4.0866	0.9763	10.7
Case 2	0	1	$1.75 \cdot 10^{-4}$	5.8511	1.1834	9.2

The results for Case 1 and 2, which are the Cases with no expansion, are shown in this section. Here the effect of increasing the Boiling number is investigated based on the data from the data points described in section 5.3.1 on page 44 and by visual inspection. In Figure 6.1 a visualisation of Case 1 and 2 at three different time steps can be seen.

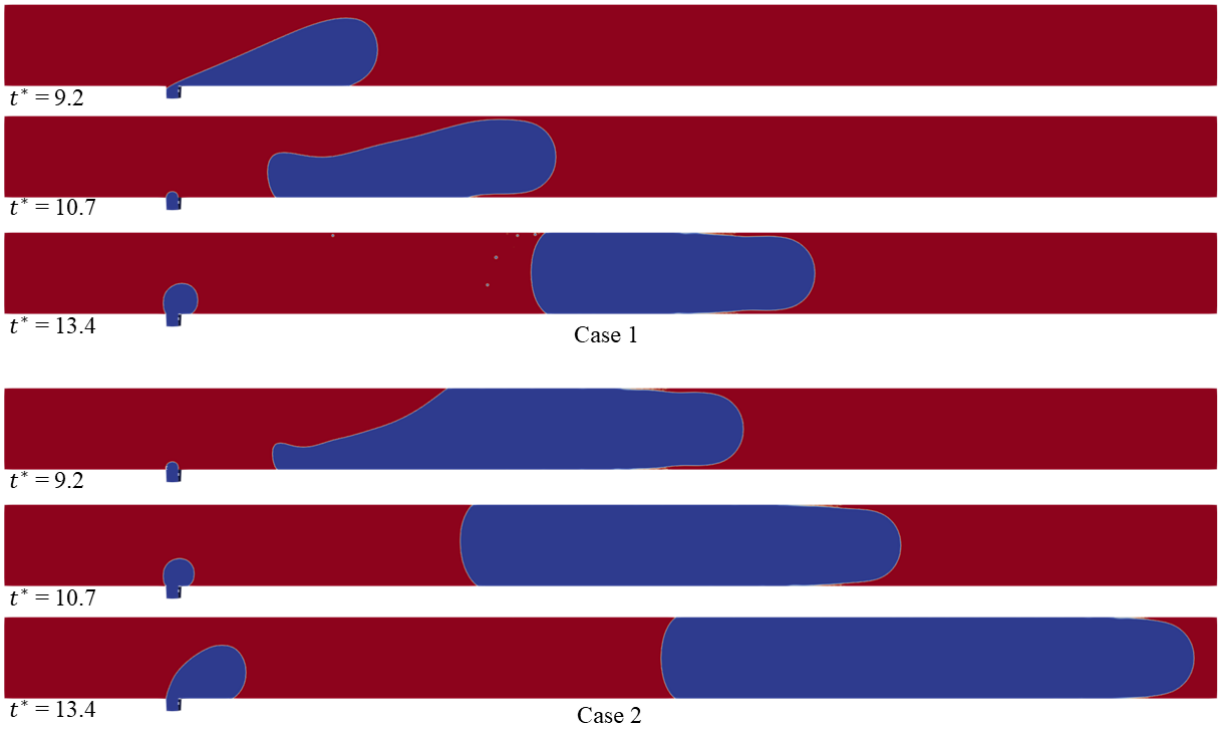

Figure 6.1: Visual inspection of Case 1 and 2 for the dimensionless time $t \cdot U_{\text{in}}/d_{\text{h}}$ of 9.2, 10.7, and 13.4 with a Boiling number of respectively B = $1.25 \cdot 10^{-4}$ and $1.75 \cdot 10^{-4}$.

The first time step shown in Figure 6.1 is for the dimensionless time of 9.2. For this time step, it can be seen that the bubble in Case 1 is growing downstream of the channel while still being attached to the cavity. At the same time, the bubble in Case 2 has just detached from the nucleation site in the cavity. At time 10.7, the bubble in Case 1 is detaching from the cavity, while the bubble in Case 2 has grown large and is far downstream of the channel. This clearly shows that a higher Boiling number results in a much faster bubble growth which is in accordance with the theory stated in Section 3.1.1 on page 10. The bubble detachment time is also faster in Case 2 as shown in both Figure 6.1 and Table 6.1. This could be due to the fast bubble growth leading to the bubble filling out the cross-sectional area faster and thus the drag from the inlet flow pushes the bubble downstream in the channel. Notice that the Boiling number can be increased by either decreasing the mass flux or by increasing the heat flux. In the present simulations, the Boiling number has been increased by increasing the heat flux. However, whether the Boiling number is increased by decreasing the mass flux or by increasing the heat flux seems to be significant. Jafari and Okutucu-Özyurt (2016) investigated the effect of changing the mass flux and found that an increase in the mass flux would also decrease the detachment time of the bubble. This may be explained by that an increase in the mass flux results in a higher drag force on the bubble, which leads to a faster detachment time. For the last time step shown in Figure 6.1, it can be seen that the bubbles are moving downstream of the channel. Here the bubble in Case 2 has become large compared to the bubble in Case 1. This is in accordance with the observations from Jafari and Okutucu-Özyurt (2016). Hence, the effect of the Boiling numbers on the bubble size seems to be the same whether it is changed by varying the mass flux or the heat flux.

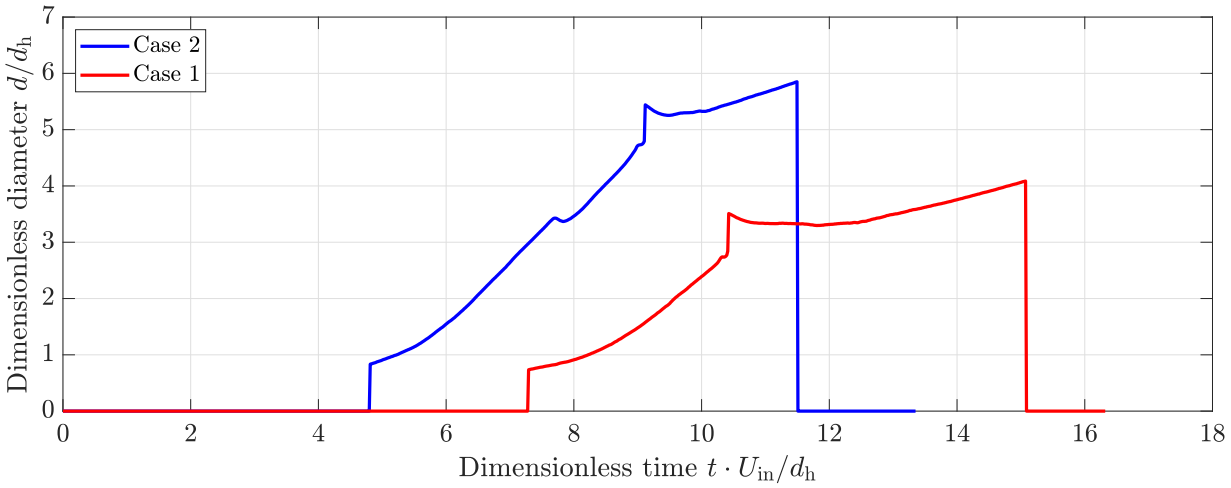

Figure 6.2: The dimensionless diameter d/d_h of the bubble to the dimensionless time $t \cdot U_{in}/d_h$ measured between $x = 2.5d_h$ and $12.5d_h$ at $y = 0.5d_h$ in the microchannel domain for Case 1 and 2.

In Figure 6.2, the bubble diameter to the time can be seen. The bubble diameter is measured between $x = 2.5d_h$ and $x = 12.5d_h$ at $y = 0.5d_h$. Here it is also clearly seen that the simulation with the highest Boiling number, Case 2, is the one with the largest bubble diameter and the one with the fastest growing bubble. The bubble in Case 2 reaches a diameter of $5.85d_h$ which is 43 % larger than the bubble in Case 1 which reaches a diameter of $4.09d_h$. The larger Boiling number results in faster evaporation of the liquid, yielding a larger and faster-growing bubble. This fast-growing bubble yields an increase in the dimensionless bubble nose velocity, which can be seen for Case 1 and 2 in Figure 6.3. Here it is seen that the tendency of bubble nose velocity is similar regardless of the Boiling number. However, the bubble nose velocity for the bubble in Case 2 is larger than the bubble nose velocity in Case 1. This can also be seen in Table 6.1 where a time average of the dimensionless bubble nose velocity is shown. The time average of the dimensionless bubble nose velocity is only calculated for the period where the velocity is above zero. For Case 2, the time average is calculated for the range of approximately 3 to 11.5 in dimensionless time, while for Case 1, the range is approximately 5 to 15. Whenever the dimensionless velocity is zero it means that the bubble nose is no longer within the measuring zone between $x = 2.5d_h$ and $12.5d_h$ at $y = 0.5d_h$. When the bubble nose first reaches the measuring zone, it has not yet expanded out in the entire cross-sectional area. The velocity in the x-direction is, therefore, lower since the bubble is capable of expanding in the y-direction as well. As the bubble fills more of the cross-sectional area, the bubble nose velocity is increased due to a larger drag force from the inlet liquid flow.

The bubble also accelerates as a result a larger surface is coming in contact with the wall yielding more applied heat and a higher growth rate. As the bubbles are detaching from the cavities at 10.4 - 10.7 and 8.9 - 9.2 in Case 1 and 2 it can be seen that the bubble velocity starts decreasing just before the detachment. This happens since the bubbles are stretched to the maximum here, and as the surface tension collapses and the bubble detaches, the bubble velocity becomes more steady as the bubble moves downstream of the channel.

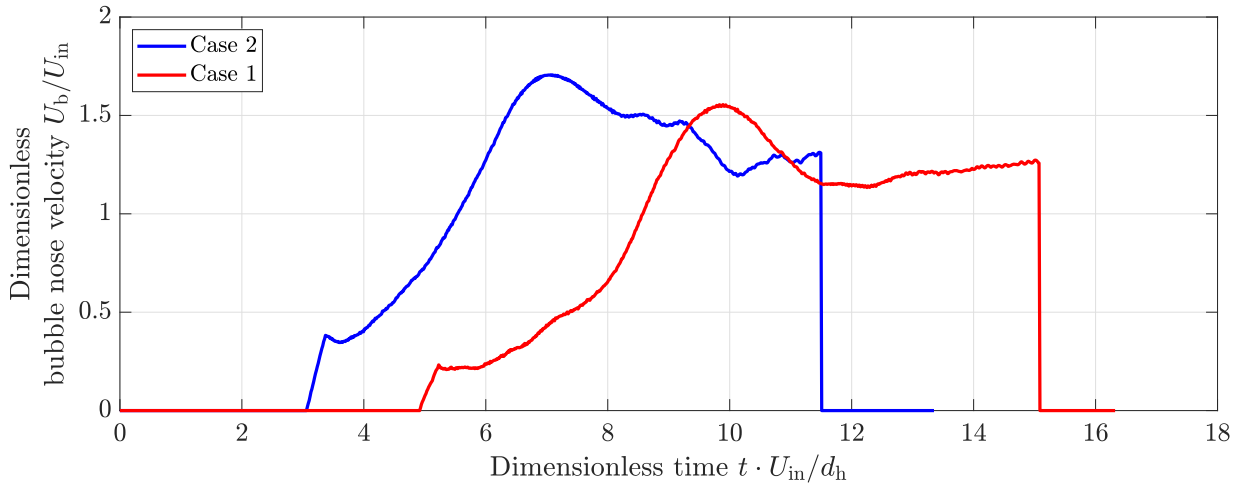

Figure 6.3: The dimensionless bubble nose velocity to the dimensionless time $t \cdot U_{in}/d_h$ measured between $x = 2.5$ and $12.5d_h$ at $y = 0.5d_h$ in the microchannel domain for Case 1 and 2.

6.1.1 Heat Transfer Performance

The heat transfer performance for the Case 1 and 2 are investigated in term of the Nusselt number. The Nusselt number has been calculated using Equation (5.4). From this equation, the only unknown parameters are the bulk temperature and the wall temperature. These two temperatures are calculated by the data points described in Section 5.3.1 on page 44 and can be seen in Figure 6.4 and 6.5 for Case 1 and 2, respectively.

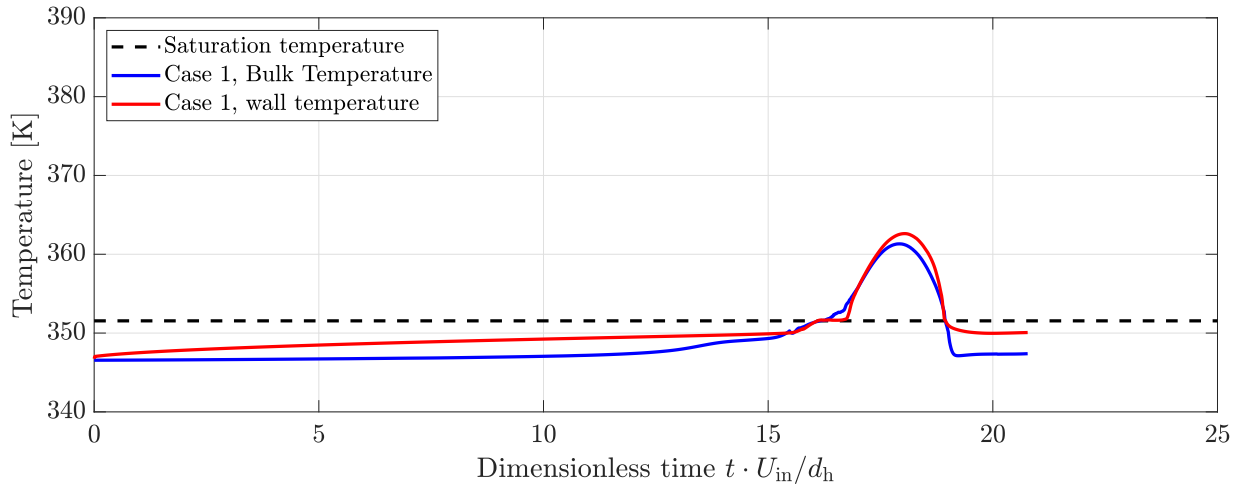

Figure 6.4: The bulk temperature measured between $y = 0d_h$ and $1d_h$ at $x = 13d_h$ and the top wall temperature measured at $x = 13d_h$ and $y = d_h$ in the microchannel domain to the dimensionless time $t \cdot U_{in}/d_h$ for Case 1.

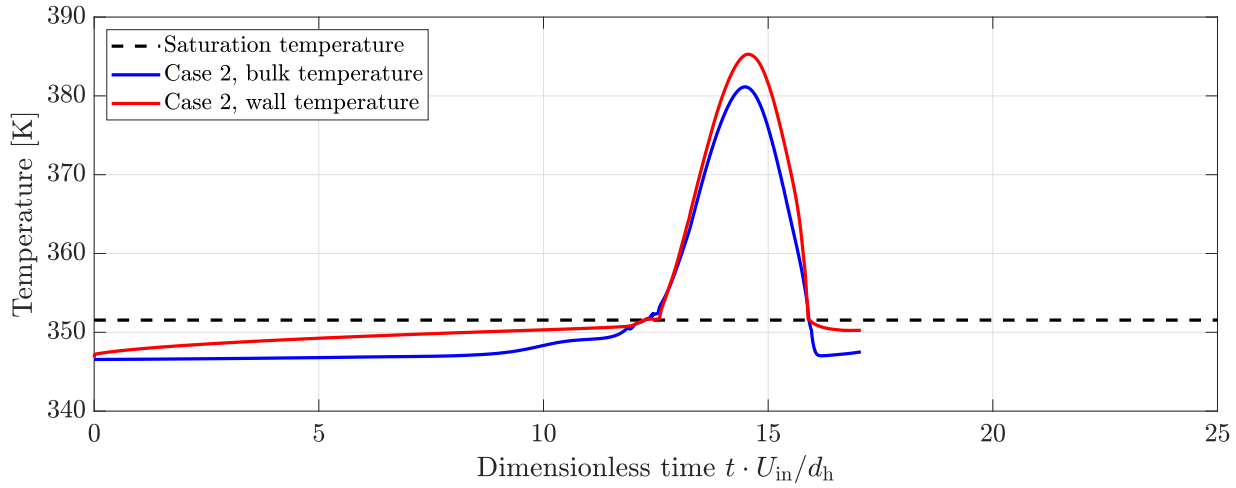

Figure 6.5: The bulk temperature measured between $y = 0d_{\text{h}}$ and $1d_{\text{h}}$ at $x = 13d_{\text{h}}$ and the top wall temperature measured at $x = 13d_{\text{h}}$ and $y = d_{\text{h}}$ in the microchannel domain to the dimensionless time $t \cdot U_{\text{in}}/d_{\text{h}}$ for Case 2.

In Figure 6.4, the bulk and wall temperature can be seen for Case 1. Both temperatures are slowly increasing until the dimensionless time of approximately 15 since only liquid is present. The slope increases further until approximately 15, indicating that the bubble is approaching and a liquid film layer is present. Afterwards, the temperature increases rapidly until approximately 17.8. This rapid increase in the temperature indicates that the bubble is passing the measuring points at $x = 13d_{\text{h}}$. Until approximately 18.5, a decrease is seen in the temperature, indicating that the bubble has left the measuring point. The same tendency is seen for Case 2 in Figure 6.5. However, this is occurring at an earlier dimensionless time step since the bubble reaches the measuring point earlier. It can also be seen that the bulk temperature crosses the wall temperature at approximately 12.5 and again at approximately 16. This occurs since a liquid film layer is present between the bubble and the wall.

The temperature boundary condition specified for the wall is defined as a constant gradient meaning that the wall temperature will be grated from the temperature of the liquid doing the liquid film layer. The bubble is, however, superheated contributing to a higher bulk temperature. Hence, the bulk temperature can exceed the wall temperature.

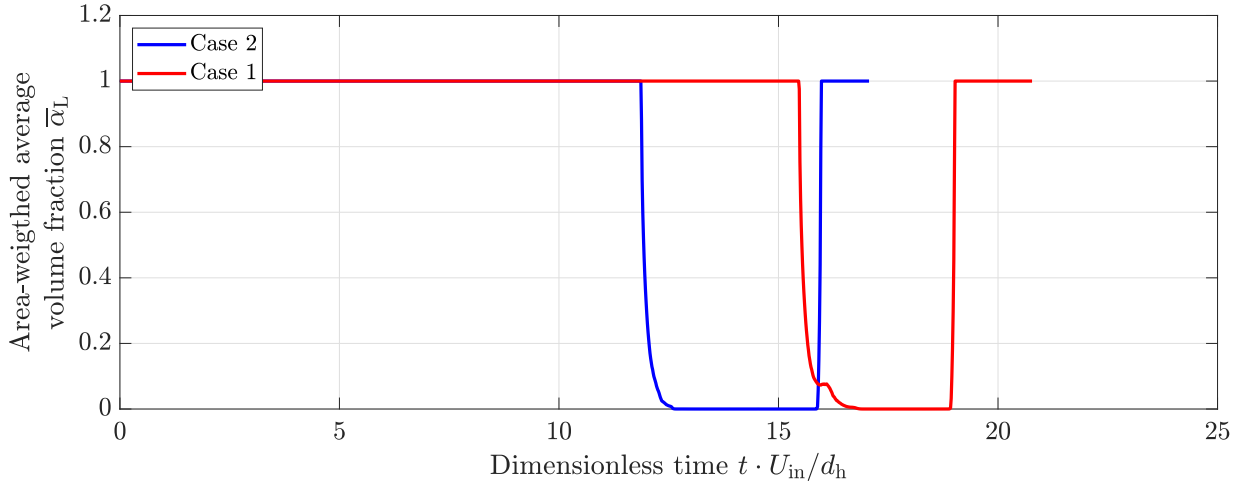

Figure 6.6: The area-weighted average volume fraction of liquid measured between $y = 0d_{\text{h}}$ and $1d_{\text{h}}$ at $x = 13d_{\text{h}}$ to the dimensionless time $t \cdot U_{\text{in}}/d_{\text{h}}$ in the microchannel domain for Case 1 and 2.

In Figure 6.6, the area-weighted volume fraction of liquid can be seen for the cross section measured between $y = 0d_h$ to $y = 1d_h$ at $x = 13d_h$ to the dimensionless time $t \cdot U_{in}/d_h$ in the microchannel domain. These results confirm that a thin liquid film layer exists at the specific time steps of where the wall and bulk temperature are crossing each other in Figure 6.4 and 6.5. A thin liquid film layer is indicated in Figure 6.6 by the volume fraction being close to zero at the dimensionless time of 12.5 for Case 2 and 16.5 for Case 1.

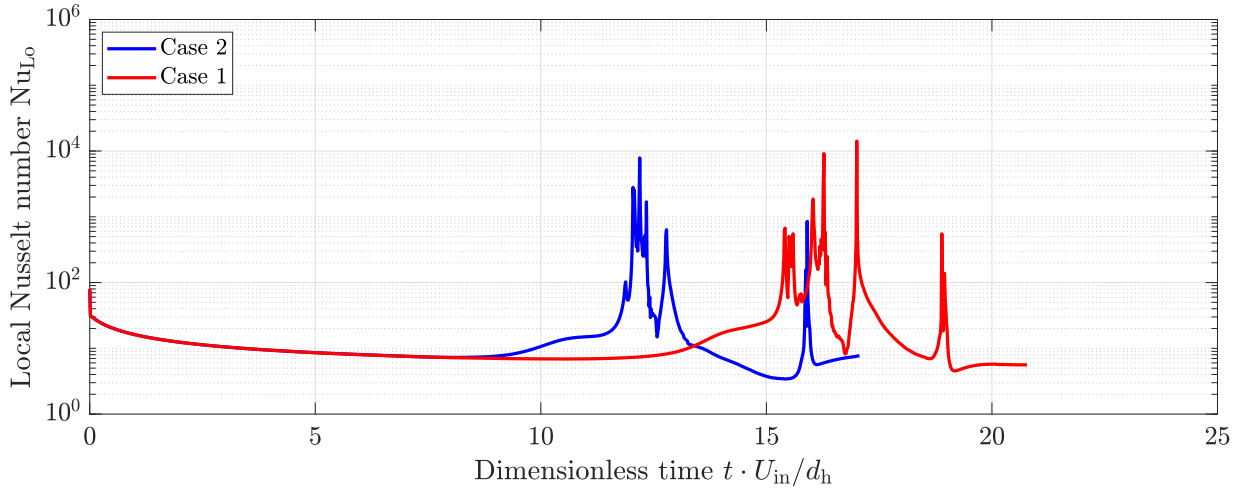

Figure 6.7: The local Nusselt number calculated at $x = 13d_h$ and $y = 1d_h$ to the dimensionless time $t \cdot U_{in}/d_h$ in the microchannel domain for Case 1 and 2. Notice that the scale of the y-axis is logarithmic.

In Figure 6.7, the local Nusselt number measured at $y = 1d_h$ and $x = 13d_h$ in the microchannel domain is shown for Case 1 and 2. It can be seen that from the dimensionless time of 0 to 9, the Nusselt number is the same for Case 1 and 2. It should be noted that Case 2 has a higher Boiling number due to a higher temperature gradient. This higher temperature gradient contributes to a higher Nusselt number, as seen in equation 5.4 on page 45. However, the increase in the temperature gradient is also contributing to a higher wall temperature, and thus it can be seen that the convective part and the conductive part of the Nusselt number is equally affected by the increase in the temperature gradient. The high peaks occurring for both Case 1 and 2 can be explained by Figure 6.4, and 6.5, and equation (5.4). From the equation, it can be seen that a decrease in the temperature difference between the bulk and the wall results in an increase in the Nusselt number. From the figures, it can be seen that the dimensionless time steps where the temperatures are crossing each other are the same time steps of where the Nusselt number is peaking. This is also where the liquid film layer is the thinnest, and thus the convective heat transfer coefficient is the highest as described in Section 3.2.3.

6.2 Results for Cases with Divergent Channel

In this section, the results of the divergent channels described in Section 5.1 are presented. First, the cases with varying expansion lengths, denoted L_E/d_h, are investigated. Afterwards the Cases with varying expansion diameters, denoted, d_E/d_h are investigated.

6.2.1 Bubble Dynamics

For the following cases, the expansion diameter is kept constant as d_E/d_h = 1.5 while the expansion length is investigated for L_E/d_h = 2, L_E/d_h = 5, and L_E/d_h 10.

Constant Expansion Diameter

Table 6.2: Key observations for Case 5, 11, and 17 and their defining dimensionless parameters. The maximum dimensionless diameter and average dimensionless velocity are measured between $x = 2.5d_h$ and $12.5d_h$ at $y = 0.5d_h$ in the microchannel domain.

	L_E/d_h	d_E/d_h	B_{in}	Maximum dimensionless diameter	Average dimensionless velocity	Dimensionless detachment time
Case 5	2	1.5	$1.25 \cdot 10^{-4}$	4.2463	0.7489	10.7
Case 11	5	1.5	$1.25 \cdot 10^{-4}$	3.0347	0.8088	8.9
Case 17	10	1.5	$1.25 \cdot 10^{-4}$	4.1117	0.9220	9.5

Table 6.3: Key observations for Case 6, 12, and 18 and their defining dimensionless parameters. The maximum dimensionless diameter and average dimensionless velocity are measured between $x = 2.5d_h$ and $12.5d_h$ at $y = 0.5d_h$ in the microchannel domain.

	L_E/d_h	d_E/d_h	B_{in}	Maximum dimensionless diameter	Average dimensionless velocity	Dimensionless detachment time
Case 6	2	1.5	$1.75 \cdot 10^{-4}$	6.2352	0.963	10.4
Case 12	5	1.5	$1.75 \cdot 10^{-4}$	5.7886	1.0431	8.9
Case 18	10	1.5	$1.75 \cdot 10^{-4}$	7.1105	1.237	10.4

Case 5, 6, 11, 12, 17, and 18 present the six cases with an expansion diameter of d_E = 1.5 d_h. Case 5, 11, 17 have an expansion length of L_E = 2 d_h, 5 d_h, and 10 d_h, respectively, and with a Boiling number of $B_{in} = 1.25 \cdot 10^{-4}$. In Figure 6.8, the dimensionless bubble nose velocity to the dimensionless time for Case 5, 11, and 17 can be seen. It shows that Case 17 reaches the highest bubble nose velocity of approximately 1.75 at time step 8.3. It also shows that Case 17 is the first to reach a bubble nose velocity of zero at the dimensionless time 15, indicating the the bubble interface has left the measuring zone between $x = 2.5d_h$ and $x = 12.5d_h$ at $y = 0.5d_h$ in the microchannel domain. In Figure 6.8, it can also be seen that Case 11 has the next highest velocity while Case 5 has the lowest. This is also seen in Table 6.2, where the dimensionless time-averaged bubble nose velocity for all three cases are shown. Here Case 5 has the lowest dimensionless time-averaged bubble nose velocity of 0.7489. This is as expected since Case 5 has the largest expansion over the length of L_E/d_h = 2. Thus, the velocity is decreasing due to the constant mass flow through the channel. The bubble in Case 5 is, therefore, reaching a lower bubble nose velocity, faster. This also explains that Case 11 has the second highest bubble nose velocity and Case 17 the highest bubble nose velocity of these three cases.

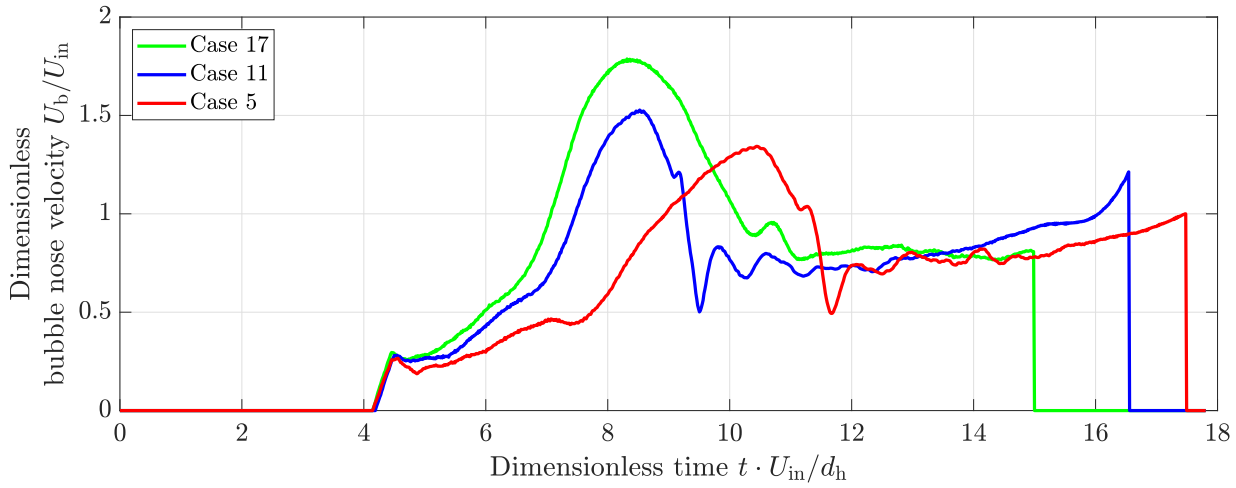

Figure 6.8: The dimensionless bubble nose velocity to the dimensionless time $t \cdot U_{in}/d_h$ measured between $x = 2.5$ and $12.5d_h$ at $y = 0.5d_h$ in the microchannel domain for Case 5, 11, and 17.

The same tendency is seen in Figure 6.9, where the dimensionless bubble nose velocity is seen for Case 6, 12, and 18. Case 6, 12, 18 have expansion lengths of, respectively, L_E / d_h = 2, L_E / d_h = 5, and L_E / d_h = 10 with a Boiling number of B_{in} = $1.75 \cdot 10^{-4}$. The time-averaged dimensionless bubble nose velocity of Case 6, 12, and 18 are listed in Table 6.3. It is seen that Case 6, 12, and 18, which have the highest Boiling number, also have a higher velocity compared to Case 5, 11, and 18, respectively. This is in accordance with the results seen for Case 1 and 2 in Figure 6.3 where the case with the highest Boiling number also has the highest bubble nose velocity.

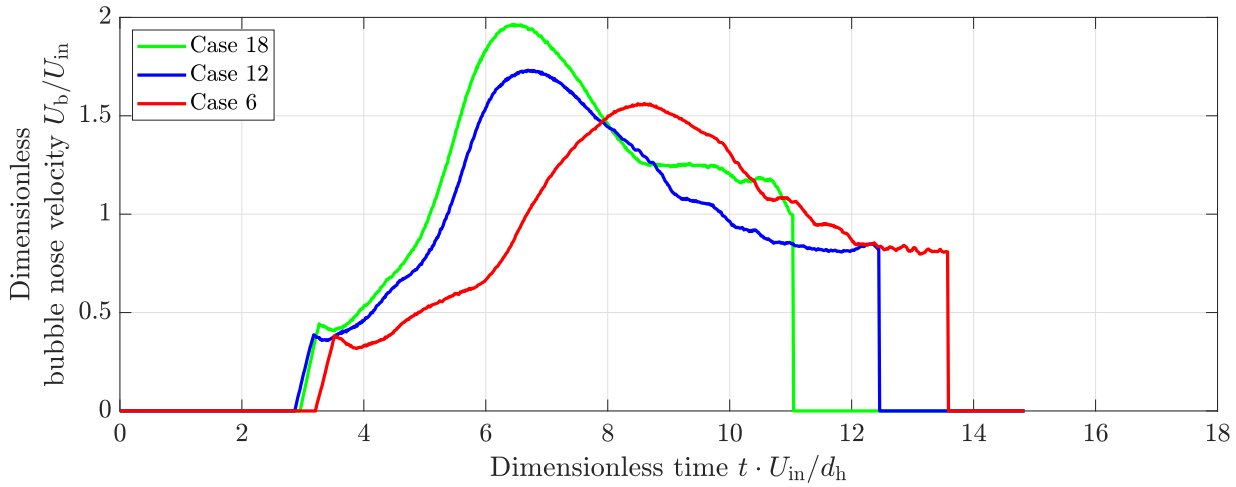

Figure 6.9: The dimensionless bubble nose velocity to the dimensionless time $t \cdot U_{in}/d_h$ measured between $x = 2.5$ and $12.5d_h$ at $y = 0.5d_h$ in the microchannel domain for Case 6, 12, and 18.

In Table 6.2 the maximum dimensionless bubble diameter measured between $x = 2.5d_h$ and $x = 12.5d_h$ at $y = 0.5d_h$ can be seen. Here Case 11 with $L_E/d_h = 5$ has the lowest dimensionless bubble diameter of 3.03 while Case 5 with $L_E/d_h = 2$ and Case 17 with $L_E/d_h = 5$ have a dimensionless bubble diameter of 4.25 and 4.11, respectively. This can first of all be explained by the expansion of the channel since the more confined channel has a larger surface-area-to-volume ratio resulting in a higher heat transfer coefficient (Kandlikar et al., 2006). The confined space also yields that a bubble

occupying the entire cross sectional area is forced to grow in the downstream direction resulting in a larger width of the bubble. In practical application the bubble can also be forced in the upstream direction referred to as reversed flow as described in Section 1.1.1. This explains that Case 17 has a higher dimensionless bubble diameter compared to Case 11. According to this, Case 5 should have a smaller bubble diameter than Case 11. However, Case 5 has a larger bubble diameter than Case 11 which can be explained by the more rapid expansion occurring and the mass balance. The more rapid expansion yields a decrease in the velocity in order to maintain a constant mass flow throughout the channel. A decrease in the velocity causes the mass flux rate to decrease resulting in an increase of the local Boiling number as seen in equation 3.1. A higher Boiling number results in a larger bubble diameter as shown in Section 6.1 on page 46. This is also confirmed in Table 6.3 by Case 6, 12, and 18 which all have a higher Boiling number and thus a larger bubble diameter compared to Case 5, 11, and 17.

Constant Expansion Length

In the following results the expansion length is kept constant while the expansion diameter is varied instead. The expansion length is chosen to be $L_E = 5d_h$ since good results where seen in the previous results for this number. Results from Case 9, 11, and 13 will therefore be shown. These cases all have a constant expansion length of $L_E = 5d_h$ while the expansions diameter is varying with $d_E = 1.25d_h$ for Case 9, $d_E = 1.5d_h$ for Case 11, and $d_E = 1.75d_h$ for Case 13.

Table 6.4: Key observations for Case 9, 11, and 13 and their defining dimensionless parameters. The maximum dimensionless diameter and average dimensionless velocity are measured between $x = 2.5d_h$ and $12.5d_h$ at $y = 0.5d_h$ in the microchannel domain.

	L_E/d_h	d_E/d_h	B_{in}	Maximum dimensionless diameter	Average dimensionless velocity	Dimensionless detachment time
Case 9	5	1.25	$1.25 \cdot 10^{-4}$	3.7752	1.154	9.5
Case 11	5	1.5	$1.25 \cdot 10^{-4}$	3.0347	0.8088	8.9
Case 13	5	1.75	$1.25 \cdot 10^{-4}$	3.2378	0.7744	9.8

In Figure 6.10 the dimensionless bubble nose velocity in the measuring zone between $x = 2.5d_h$ and $x = 12.5d_h$ at $y = 0.5d_h$ in the microchannel domain due to the dimensionless time can be seen for Case 9, 11, and 13. An time average of this velocity can likewise be seen in Table 6.4 for Case 9, 11, 13. The effect of the expansion diameter is as expected were the lower expansion diameter of $d_E = 1.25d_h$ in Case 9 yields a higher velocity compared to the higher expansion diameter of $d_E = 1.75d_h$ in Case 13. This is due to the mass balance as previous stated where an decrease in the cross sectional area results in an increase of the velocity.

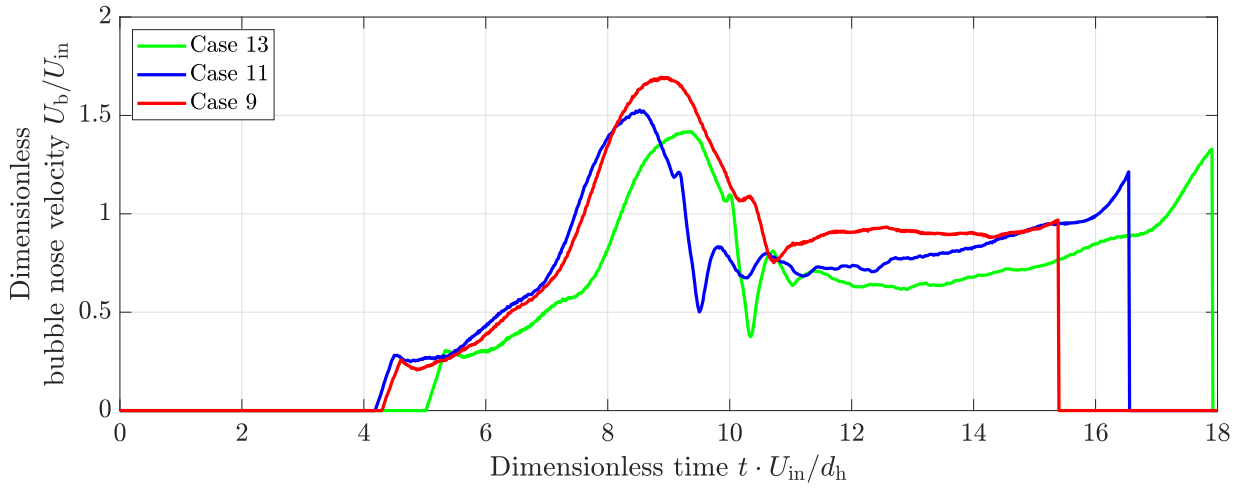

Figure 6.10: The dimensionless bubble nose velocity to the dimensionless time $t \cdot U_{\text{in}}/d_{\text{h}}$ measured between $x = 2.5$ and $12.5d_{\text{h}}$ at $y = 0.5d_{\text{h}}$ in the microchannel domain for Case 9, 11, and 13.

In Table 6.4 the maximum dimensionless diameter can be seen for Case 9, 11, and 13. The result of the maximum diameter is similar to what was seen for Case 5, 11, and 17. Case 11 with the expansion of 1.5 has the lowest dimensionless diameter compared to Case 9 and 13 with expansion diameters of $d_{\text{E}} = 1.25d_{\text{h}}$ and $d_{\text{E}} = 1.75d_{\text{h}}$, respectively.

However if the expansion length is kept at $L_{\text{E}} = 5d_{\text{h}}$ while the Boiling number is increased to $\text{B} = 1.75 \cdot 10^{-4}$ it is no longer the case with the expansion diameter of $d_{\text{E}} = 1.5d_{\text{h}}$ that has the lowest bubble diameter. This is shown by comparing Case 10, 12, and 14 where the maximum dimensionless diameter can be seen in Table 6.5. Here it can be seen that it is now Case 14 with $d_{\text{E}} = 1.75d_{\text{h}}$ that has the lowest diameter. This indicates that the size of the bubble is a balance between the Boiling number and the slope of the expansion.

Table 6.5: Key observations for Case 10, 12, and 14 and their defining dimensionless parameters. The maximum dimensionless diameter and average dimensionless velocity are measured between $x = 2.5d_{\text{h}}$ and $12.5d_{\text{h}}$ at $y = 0.5d_{\text{h}}$ in the microchannel domain.

	$L_{\text{E}}/d_{\text{h}}$	$d_{\text{E}}/d_{\text{h}}$	B_{in}	Maximum dimensionless diameter	Average dimensionless velocity	Dimensionless detachment time
Case 10	5	1.25	$1.75 \cdot 10^{-4}$	6.6053	1.1667	10.1
Case 12	5	1.5	$1.75 \cdot 10^{-4}$	5.7886	1.0431	8.9
Case 14	5	1.75	$1.75 \cdot 10^{-4}$	5.2855	0.9643	8.9

6.2.2 Heat Transfer

In this section the effect of changing either the expansion length or the expansion diameter are shown. First the expansion diameter is kept constant at $d_{\text{E}} = 1.5d_{\text{h}}$, the Boiling number is $\text{B} = 1.25 \cdot 10^{-4}$, and the expansion length is changed from $L_{\text{E}} = 2d_{\text{h}}$ for Case 5, $L_{\text{E}} = 5d_{\text{h}}$ for Case 11, and $L_{\text{E}} = 10d_{\text{h}}$ for Case 17.

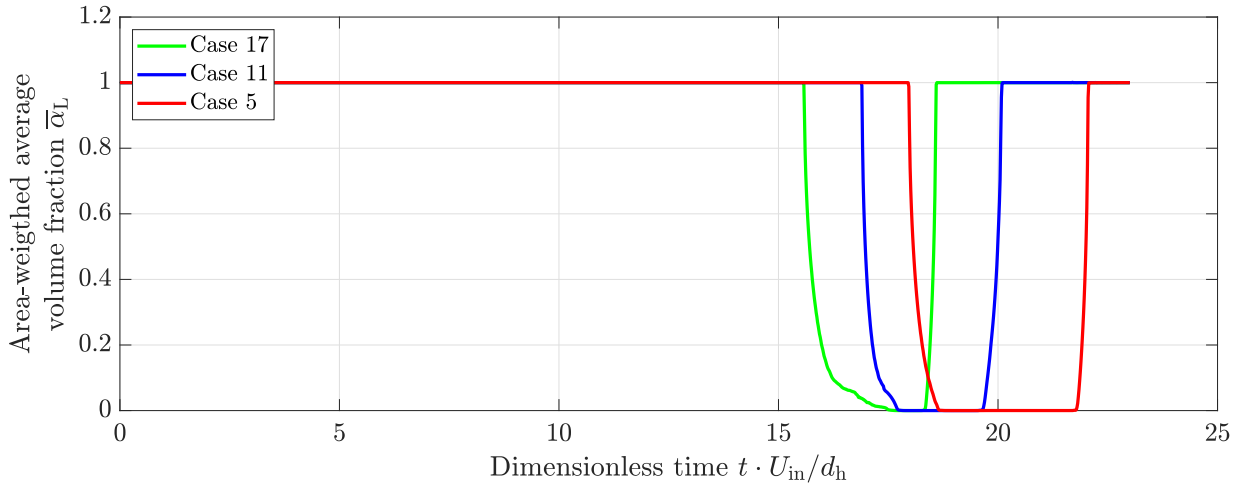

Figure 6.11: .

In Figure 6.11, the area-weighted average volume fraction of liquid can be seen for Case 5, 11, and 17. It is seen that the volume fraction for Case 17 is the first to decrease at a dimensionless time of approximately 15.5. Hereafter comes Case 11 at approximately 17 and Case 5 at approximately 17.7. This indicates, the time where the nose of the bubble reaches the measuring line in the microchannel domain between $y = 0d_h$ and $y = 1d_h$ at $x = 13d_h$. The bubble in Case 17 is the first to reach the measuring points, and this is a result of the higher dimensionless average bubble velocity as seen in Table 6.2. The bubble in Case 17 is also the first to pass these measuring points, indicated by the volume fraction of liquid reaching 1 at the dimensionless time of approximately 18. In the dimensionless time between approximately 16 and 17.5, it can be seen that the slope is decreasing as it approaches zero. This indicates that a liquid film layer is present between the wall and the bubble. The dimensionless time range where the liquid film layer is present is also the time with the higher Nusselt number as seen in Figure 6.12. It can also be seen that the lowest Nusselt number is at the time with either solely liquid or gas which is indicated by the volume fraction of liquid being 0 in Figure 6.11.

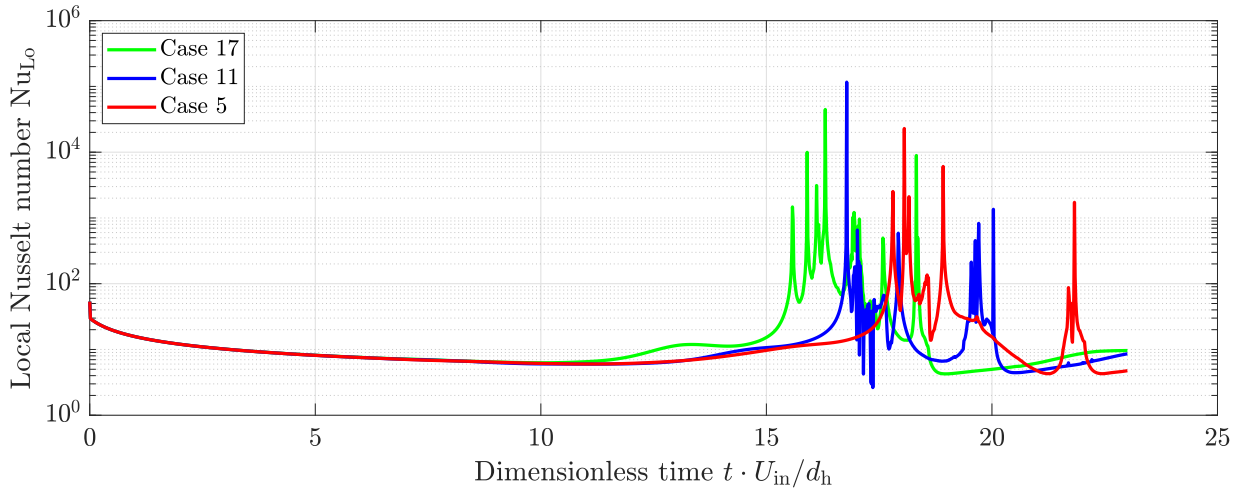

Figure 6.12: The local Nusselt number calculated at $x = 13d_h$ and $y = 1d_h$ to the dimensionless time $t \cdot U_{in}/d_h$ in the microchannel domain for Case 5, 11, and 17. Notice that the scale of the y-axis is logarithmic.

In Figure 6.12, it can also be seen that Case 11 has the highest peak in the local Nusselt number. Whereas Case 17 has multiple peaks over a longer period. If comparing Figure 6.12 with Figure 6.11, it can be seen that Case 17 has a longer period with liquid film layer resulting in the long period of peaks seen in Figure 6.12.

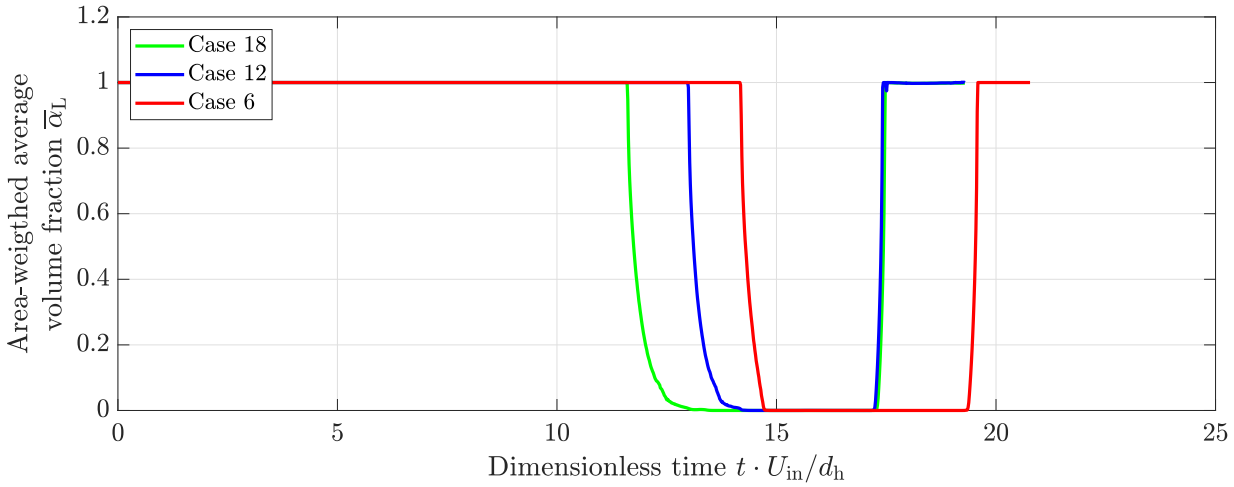

Figure 6.13: The area-weighted average volume fraction of liquid measured between $y = 0d_h$ and $1d_h$ at $x = 13d_h$ to the dimensionless time $t \cdot U_{in}/d_h$ in the microchannel domain for Case 6, 12, and 18.

In Figure 6.13, the area-weighted average volume fraction of liquid can be seen for Case 6, 12, and 18. Case 6, 12, and 18 have the same expansion length and expansion diameter as Case 5, 11, and 17, respectively. Case 6, 12, 18 have however a higher Boiling number of B = $1.75 \cdot 10^{-4}$. In general it can be seen in Figure 6.13, that Case 6, 12, and 18 have much more dryout compared to Case 5, 11, and 17 in 6.11. Case 6, 12, and 18 also have a much shorter liquid film layer region. This is also reflected in the Nusselt number seen in Figure 6.14 where the Nusselt number is much lower compared to Case 5, 11, and 17. This was also seen in Case 1 and 2, where Case 1, with the lowest Boiling number, had higher peaks in the Nusselt number.

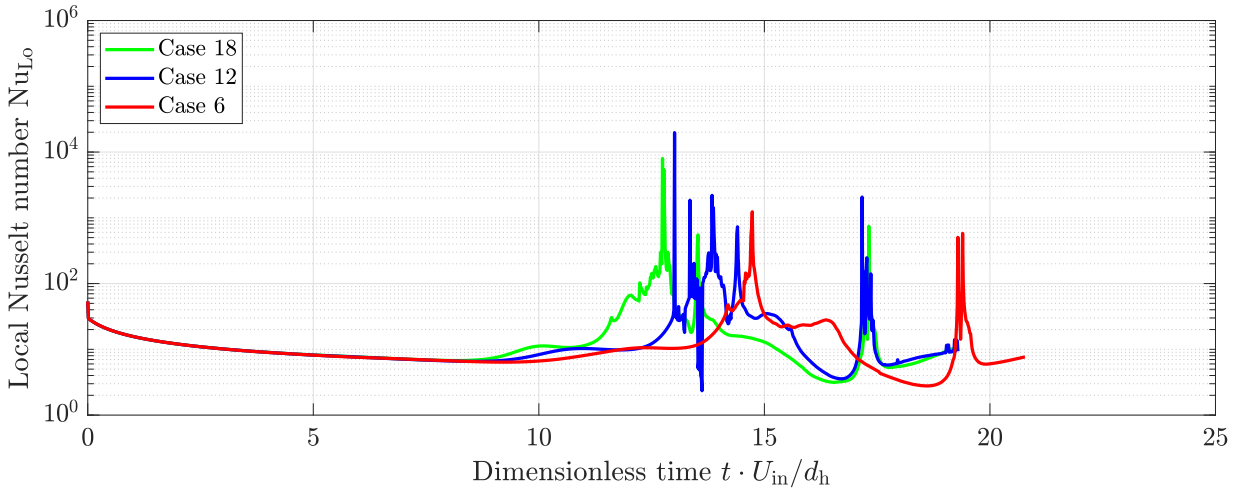

Figure 6.14: The local Nusselt number calculated at $x = 13d_h$ and $y = 1d_h$ to the dimensionless time $t \cdot U_{in}/d_h$ in the microchannel domain for Case 6, 12, and 18. Notice that the scale of the y-axis is logarithmic.

The area-weighted average volume fraction of liquid and the Nusselt number can also be seen for Case 9, 11, 13 in Figure 6.15 and 6.16 . Case 9, 11, and 13 have the same expansion length of $L_E = 5d_h$ but varies in expansion diameter. Overall, it can be seen that Case 11 has the highest Nusselt number peaks. Case 11 was also the with smallest diameter and the fastest detachment time.

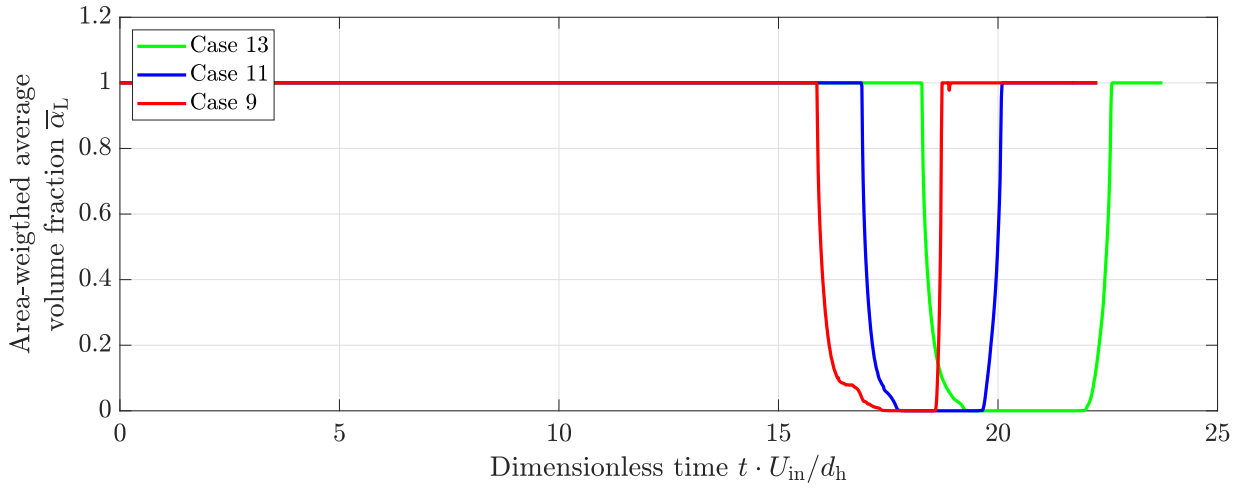

Figure 6.15: The area-weighted average volume fraction of liquid measured between $y = 0d_h$ and $1d_h$ at $x = 13d_h$ to the dimensionless time $t \cdot U_{in}/d_h$ in the microchannel domain for Case 9, 11, and 13.

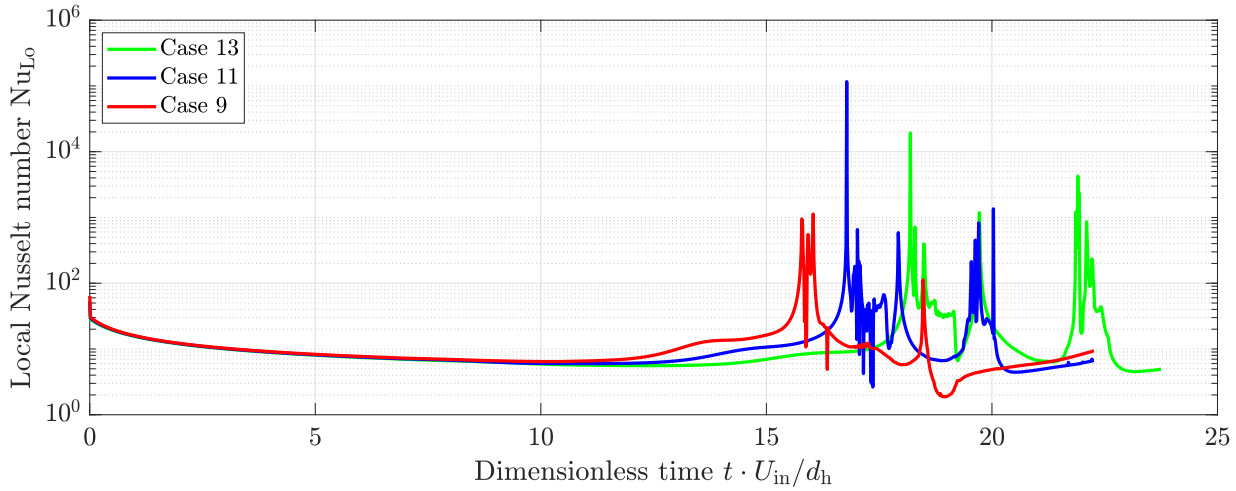

Figure 6.16: The local Nusselt number calculated at $x = 13d_h$ and $y = 1d_h$ to the dimensionless time $t \cdot U_{in}/d_h$ in the microchannel domain for Case 9, 11, and 13. Notice that the scale of the y-axis is logarithmic.

6.3 Overall Discussion of Results

It can be seen from Table 6.1 that an increase in the Boiling number results in an increase in maximum dimensional diameter. The Boiling number was increased by 40 %, which results in a 43.2 % increase in the diameter of the bubble. Between Case 11 and 12, the increase in the diameter was above 90 %. It can also be seen in Table 6.1 that the average dimensional velocity increases with an increasing Boiling number. The cases with the high Boiling number have, in general, a more rapid bubble growth which resulted in larger bubbles and faster bubble nose velocities. Case 2, which

has the higher Boiling number, also has the faster detachment time compared to Case 1. This is, however, not always the result. For Case 17 and 18, it was Case 17 with the lowest Boiling number that has the fastest detachment time. In Figure 6.6 and 6.7 it is seen that an increase in the Boiling number, decreases the area with liquid film layer resulting in lower Nusselt numbers.

The impact of the expanding channel on the diameter of the bubble do not show any clear tendencies. In some situations the bubble diameter is increased when the expansion is increased while it also increased when the expansion was decreased. The case with the lowest diameter was Case 11 which has an expanding length of $L_E = 5d_h$ and an expanding diameter of $d_E = 1.5d_h$. For the case with the highest Boiling number it is however Case 14 that has the lowest diameter. Case 14 has an expanding length of $L_E = 5d_h$ and an expanding diameter of $d_E = 1.75d_h$. The Nusselt number shows the same tendencies between the different cases as the bubble diameter. The case having the highest Nusselt number is Case 11, which also has the smallest bubble diameter. The average velocity does, however, show a clear tendency. The channels with the largest expansion and steepest expanding slope have the lowest velocity.

Chapter 7
Closure

7.1 Conclusion

In the present study, flow boiling in divergent shaped microchannels have been numerically investigated. This has been done through CFD simulations with a new assembled volume of fluid based solver in OpenFOAM. First, the characteristics of flow boiling and the numerical details of the solver have been presented in order to form the foundation for the numerical investigation. Two validation problems have been simulated to test the accuracy and applicability of the solver.

The first validation problem is the 1D Stefan problem which has an analytic solution. For this problem, two phase-change models presented by, respectively, Lee and Berenson have been simulated. Based on comparison to the analytic solution, both phase-change models showed high accuracy in the results. In relation to the interface position, the simulation with the Lee model showed an error of 2.5 % and the simulation with the Tanasawa model an error of 0.25 % as shown in Table 4.2 on page 26. On that account, it is concluded that the solver accurately can simulate the problem, and thus the Tanasawa model has been selected and implemented as the phase-change solver in the further study.

The second validation problem regards 2D film boiling with an implemented Taylor wave. For this validation problem, the space-averaged Nusselt number for the numerical simulations have been compared to the Nusselt number correlations presented by Berenson and Klimenko, as shown in Figure 4.11 on page 35. The simulated Nusselt number deviates with, respectively, 14 % and 31 % to the two Nusselt number correlations. Compared to the results of other researchers, this result is within an acceptable range. The bubble shape, bubble departure, and the heat flux influence have furthermore been compared to the results of other researchers, and the comparison shows agreement in the tendencies. A grid independence study has, furthermore, been applied this validation problem as shown in Figure 4.12 and 4.13 on page 36. The feature of dynamic mesh refinement is included in this study, and it is shown that the dynamic mesh of 120 x 240 cells with one refinement level is as accurate as the fine mesh of 240 x 480 cells. Therefore, it can be concluded that the required number of cells and thus the processing power can be abbreviated without compromising the accuracy of the results by applying dynamic mesh refinement. Hence, dynamic mesh refinement is applied in the microchannel flow boiling simulations.

The numerical setup of the microchannel flow boiling and the initial simulation are presented in Chapter 5. A parametric study is performed upon the Boiling number and the slope of the wall in term of the dimensionless numbers; D_E / D_h and L_E / D_h which are illustrated in Figure 5.7 on page 44. The Boiling number is varied from $1.25 \cdot 10^{-4}$ to $1.75 \cdot 10^{-4}$. The increase in the Boiling number yields an increase in the bubble growth rate yielding higher bubble velocities. It is also seen that the bubble diameter becomes larger, resulting in large bubbles with a minimal liquid film layer. This results in low Nusselt numbers. The detachment time is also increased due to an increase in the Boiling number. However, a change in the slope of the wall also changed the detachment time, and under some conditions, the case with the highest Boiling number has the shortest detachment time. Thus the slope of the expansion has a greater impact on the detachment time. The Nusselt

number is highest for Case 11 which has the following values $D_E = 1.5\ D_h$ and $L_E = 5\ D_h$. This case also has the smallest bubble diameter. For the cases with the Boiling number of $B = 1.75 \cdot 10^{-4}$, Case 14 has the smallest bubble. Case 14 has values of $D_E = 1.75\ D_h$ and $L_E = 5\ D_h$ indicating that the optimal slope for a divergent channel depends on the Boiling number.

Chapter 8

Future Work

To assume that a system can be seen as 2D comes in most cases with some uncertainties. In the present work, it was stated that a rectangular channel with an aspect ratio above wight could be seen as a 2D system. However, the bubble nucleation and growth have 3D effects. First, when the bubble has grown to a slug, the characteristics can be seen as 2D. 3D simulations would, therefore, be the next step in order to obtain a more thorough understanding of bubble dynamics under nucleation and bubble growth. 3D simulations of a squared channel could also be interesting in order to account for the effect of the corners. Due to the surface tension, a bubble is shaped curved, leading to liquid is flowing in the corners, and thus a liquid film layer is more likely to be present. The presence of a film layer increases the Nusselt number, as proven in this study and is also the flow regime with the highest convective heat transfer coefficient. Hence, 3D simulations in squared microchannels could be investigated with the objective of enhancing the heat transfer performance. Simulating in 3D would also provide more accurate results, but it comes with a cost of a lot more computational power.

The simulations in the present work have been for a single microchannel. However, in most real-life applications, a microchannel cooling system would consist of multiple microchannels. It was stated in theory about instabilities in Section 1.1.1 that a system with multiple channels would be more likely to experience instabilities such as reverse flow. A natural step would therefore be to investigate a microchannel system with multiple channels in order to get a better understanding of how instabilities such as reverse flow can be avoided. Such a system would, however, have to be simulated in 3D, and the computational cost would be significantly higher than for the present work. Access to more computational power would therefore be required.

In this study, a cavity was defined as nucleation site. In a practical application, the surface roughness itself is working as nucleation site with countless of cavities. To simulate this, more processing power is required since bubbles will nucleate everywhere at the walls, and thus the dynamic mesh needs to refine everywhere. Alternatively, a fixed grid could be used, however, a much fine mesh would be required. Furthermore, the domain length should be significantly longer to account for the bubble merging and the flow patterns.

Bibliography

Agostini et al., 2007. Bruno Agostini, Matteo Fabbri, Jung E. Park, Leszek Wojtan, John R. Thome and Bruno Michel. *State of the Art of High Heat Flux Cooling Technologies*. Heat Transfer Engineering, 28(4), 258–281, 2007. doi:10.1080/01457630601117799.

Alexiades et al., 1993. Vasilios Alexiades and Alan D. Solomon. *MATHEMATICAL MODELING OF MELTING AND FREEZING PROCESSES*. HEMISPHERE PUBLISHING CORPORATION, 1993. ISBN: 1-56032-125-3.

Berenson, 08 1961. P. J. Berenson. *Film-Boiling Heat Transfer From a Horizontal Surface*. Journal of Heat Transfer, 83(3), 351–356, 1961. ISSN: 0022-1481. doi:10.1115/1.3682280. URL: https://doi.org/10.1115/1.3682280.

Berenson. P J Berenson. *TRANSITION BOILING HEAT TRANSFER FROM A HORIZONTAL SURFACE. Technical Report No. 17*. URL: https://www.osti.gov/biblio/4205359.

Bogojevic et al., 2009. D. Bogojevic, K. Sefiane, A.J. Walton, H. Lin and G. Cummins. *Two-phase flow instabilities in a silicon microchannels heat sink*. International Journal of Heat and Fluid Flow, 30(5), 854–867, 2009. doi:https://doi.org/10.1016/j.ijheatfluidflow.2009.03.013.

Bogojevic et al., 2013. D. Bogojevic, K. Sefiane, G. Duursma and A.J. Walton. *Bubble dynamics and flow boiling instabilities in microchannels*. International Journal of Heat and Mass Transfer, 58(1), 663–675, 2013. doi:https://doi.org/10.1016/j.ijheatmasstransfer.2012.11.038.

Brutin et al., 2003. D Brutin, F Topin and L Tadrist. *Experimental study of unsteady convective boiling in heated minichannels*. International Journal of Heat and Mass Transfer, 46(16), 2957–2965, 2003.

Ferrari et al., 2018a. Andrea Ferrari, Mirco Magnini and John R. Thome. *Numerical analysis of slug flow boiling in square microchannels*. International Journal of Heat and Mass Transfer, 123(1), 928–944, 2018. doi:https://doi.org/10.1016/j.ijheatmasstransfer.2018.03.012.

Ferrari et al., 2018b. Andrea Ferrari, Mirco Magnini and John R. Thome. *Numerical analysis of slug flow boiling in square microchannels*. International Journal of Heat and Mass Transfer, 123, 928 – 944, 2018. ISSN: 0017-9310. doi:https://doi.org/10.1016/j.ijheatmasstransfer.2018.03.012. URL: http://www.sciencedirect.com/science/article/pii/S0017931018303016.

Guo et al., 06 2011. D. Guo, Dongliang Sun, Zeng-Yao Li and Wen-Quan Tao. *Phase Change Heat Transfer Simulation for Boiling Bubbles Arising from a Vapor Film by the VOSET Method*. Numerical Heat Transfer, Part A: Applications, 857–881, 2011. doi:10.1080/10407782.2011.561079.

Hardt et al., 2008a. S. Hardt and F. Wondra. *Evaporation model for interfacial flows based on a continuum-field representation of the source terms*. Journal of Computational Physics, 227(11), 5871 – 5895, 2008. ISSN: 0021-9991. doi:https://doi.org/10.1016/j.jcp.2008.02.020. URL: http://www.sciencedirect.com/science/article/pii/S0021999108001228.

Hardt et al., 2008b. S. Hardt and F. Wondra. *Evaporation model for interfacial flows based on a continuum-field representation of the source terms*. Journal of Computational Physics, 227(11), 5871–5895, 2008. ISSN: 0021-9991. doi:https://doi.org/10.1016/j.jcp.2008.02.020. URL: https://www.sciencedirect.com/science/article/pii/S0021999108001228.

Hetsroni et al., 2006. G. Hetsroni, A. Mosyak, E. Pogrebnyak and Z. Segal. *Periodic boiling in parallel micro-channels at low vapor quality*. International Journal of Multiphase Flow, 32(10), 1141–1159, 2006. doi:https://doi.org/10.1016/j.ijmultiphaseflow.2006.06.005.

Hirt et al., 1981. C.W Hirt and B.D Nichols. *Volume of fluid (VOF) method for the dynamics of free boundaries*. Journal of Computational Physics, 39(1), 201–225, 1981. ISSN: 0021-9991. doi:https://doi.org/10.1016/0021-9991(81)90145-5. URL: https://www.sciencedirect.com/science/article/pii/0021999181901455.

Jafari et al., 2016. Rahim Jafari and Tuba Okutucu-Özyurt. *Numerical simulation of flow boiling from an artificial cavity in a microchannel*. International Journal of Heat and Mass Transfer, 97(1), 270–278, 2016. doi:https://doi.org/10.1016/j.ijheatmasstransfer.2016.02.028.

Kandlikar, 2002. Satish G Kandlikar. *Fundamental issues related to flow boiling in minichannels and microchannels*. Experimental Thermal and Fluid Science, 26(2), 389–407, 2002. doi:https://doi.org/10.1016/S0894-1777(02)00150-4.

Kandlikar, 2006. Satish G. Kandlikar. *Nucleation characteristics and stability considerations during flow boiling in microchannels*. Experimental Thermal and Fluid Science, 30(5), 441–447, 2006. doi:https://doi.org/10.1016/j.expthermflusci.2005.10.001.

Kandlikar et al., 2006. Satish G. Kandlikar, Srinivas Garimella, Dongqing Li, Stéphane colin and Michael R. King. *Heat Transfer and Fluid Flow in Minichannels and Microchannels*. Elsevier, 1 edition, 2006. ISBN: 0-0804-4527-6.

Karayiannis et al., 2017. T.G. Karayiannis and M.M. Mahmoud. *Flow boiling in microchannels: Fundamentals and applications*. Applied Thermal Engineering, 115(1), 1372–1397, 2017. doi:https://doi.org/10.1016/j.applthermaleng.2016.08.063.

Kharangate et al., 2017. Chirag R. Kharangate and Issam Mudawar. *Review of computational studies on boiling and condensation*. International Journal of Heat and Mass Transfer, 108, 1164–1196, 2017. ISSN: 0017-9310. doi:https://doi.org/10.1016/j.ijheatmasstransfer.2016.12.065. URL: https://www.sciencedirect.com/science/article/pii/S0017931016320051.

Kharangate et al., 2020. Chirag R. Kharangate and Issam Mudawar. *Numerical investigation of film boiling heat transfer on the horizontal surface in an oscillating system with low frequencies*. Nuclear Engineering and Technology, 52(5), 918–924, 2020. ISSN: 1738-5733. doi:https://doi.org/10.1016/j.net.2019.11.002. URL: https://www.sciencedirect.com/science/article/pii/S1738573319304784.

Kim et al., 2014. Sung-Min Kim and Issam Mudawar. *Review of databases and predictive methods for heat transfer in condensing and boiling mini/micro-channel flows*. International Journal of Heat and Mass Transfer, 77, 627 – 652, 2014. ISSN: 0017-9310. doi:https://doi.org/10.1016/j.ijheatmasstransfer.2014.05.036. URL: http://www.sciencedirect.com/science/article/pii/S0017931014004360.

Klimenko, 1981. V.V. Klimenko. *Film boiling on a horizontal plate — new correlation*. International Journal of Heat and Mass Transfer, 24(1), 69–79, 1981. ISSN: 0017-9310. doi:https://doi.org/10.1016/0017-9310(81)90094-6. URL: https://www.sciencedirect.com/science/article/pii/0017931081900946.

Lee et al., 2008. Jaeseon Lee and Issam Mudawar. *Fluid flow and heat transfer characteristics of low temperature two-phase micro-channel heat sinks – Part 1: Experimental methods and flow visualization results*. International Journal of Heat and Mass Transfer, 51(17), 4315–4326, 2008. doi:https://doi.org/10.1016/j.ijheatmasstransfer.2008.02.012.

Lee, 1980. W. H. Lee. *A Pressure Iteration Scheme for Two-Phase Flow Modeling*. pages 407 – 431, 1980.

Li et al., 2010. Wei Li and Zan Wu. *A general criterion for evaporative heat transfer in micro/mini-channels*. International Journal of Heat and Mass Transfer, 53(9), 1967 – 1976, 2010. doi:https://doi.org/10.1016/j.ijheatmasstransfer.2009.12.059.

Ling et al., 2015. Kong Ling, Gihun Son, Dong-Liang Sun and Wen-Quan Tao. *Three dimensional numerical simulation on bubble growth and merger in microchannel boiling flow*. International Journal of Thermal Sciences, 98(1), 135 – 147, 2015. doi:https://doi.org/10.1016/j.ijthermalsci.2015.06.019.

Liu et al., 2005. Dong Liu, Poh-Seng Lee and Suresh V. Garimella. *Prediction of the onset of nucleate boiling in microchannel flow*. International Journal of Heat and Mass Transfer, 48(25), 5134 – 5149, 2005. ISSN: 0017-9310. doi:https://doi.org/10.1016/j.ijheatmasstransfer.2005.07.021. URL: `http://www.sciencedirect.com/science/article/pii/S0017931005004837`.

LIU, 2017. Qingming LIU. *Numerical study of flow boiling in micro/mini channels*. pages 1–82, 2017. ISSN: 1102-0245.

Magnini et al., 2020a. M. Magnini and O.K. Matar. *Numerical study of the impact of the channel shape on microchannel boiling heat transfer*. International Journal of Heat and Mass Transfer, 150(1), 119322, 2020. doi:https://doi.org/10.1016/j.ijheatmasstransfer.2020.119322.

Magnini et al., 2020b. M. Magnini and O.K. Matar. *Numerical study of the impact of the channel shape on microchannel boiling heat transfer*. International Journal of Heat and Mass Transfer, 150(1), 119322, 2020. doi:https://doi.org/10.1016/j.ijheatmasstransfer.2020.119322.

Magnini et al., 2013a. M. Magnini, B. Pulvirenti and J.R. Thome. *Numerical investigation of hydrodynamics and heat transfer of elongated bubbles during flow boiling in a microchannel*. International Journal of Heat and Mass Transfer, 59, 451–471, 2013. ISSN: 0017-9310. doi:https://doi.org/10.1016/j.ijheatmasstransfer.2012.12.010. URL: `https://www.sciencedirect.com/science/article/pii/S0017931012009556`.

Magnini et al., 2013b. M. Magnini, B. Pulvirenti and J.R. Thome. *Numerical investigation of the influence of leading and sequential bubbles on slug flow boiling within a microchannel*. International Journal of Thermal Sciences, 71(1), 36–52, 2013. doi:https://doi.org/10.1016/j.ijthermalsci.2013.04.018.

Marcinichen et al., 2013. Jackson B. Marcinichen, Jonathan A. Olivier, Nicolas Lamaison and John R. Thome. *Advances in Electronics Cooling*. Heat Transfer Engineering, 34(5-6), 434–446, 2013. doi:10.1080/01457632.2012.721316.

Marek et al., 2001a. R. Marek and J. Straub. *Analysis of the evaporation coefficient and the condensation coefficient of water*. International Journal of Heat and Mass Transfer, 44(1), 39–53, 2001. ISSN: 0017-9310. doi:https://doi.org/10.1016/S0017-9310(00)00086-7. URL: `https://www.sciencedirect.com/science/article/pii/S0017931000000867`.

Marek et al., 2001b. R. Marek and J. Straub. *Analysis of the evaporation coefficient and the condensation coefficient of water*. International Journal of Heat and Mass Transfer, 44(1), 39–53, 2001. ISSN: 0017-9310. doi:https://doi.org/10.1016/S0017-9310(00)00086-7. URL: https://www.sciencedirect.com/science/article/pii/S0017931000000867.

Megahed, 2011. Ayman Megahed. *Experimental investigation of flow boiling characteristics in a cross-linked microchannel heat sink*. International Journal of Multiphase Flow, 37(4), 380–393, 2011. ISSN: 0301-9322. doi:https://doi.org/10.1016/j.ijmultiphaseflow.2010.12.002. URL: https://www.sciencedirect.com/science/article/pii/S0301932210001977.

Mukherjee et al., 2009. A. Mukherjee and S.G. Kandlikar. *The effect of inlet constriction on bubble growth during flow boiling in microchannels*. International Journal of Heat and Mass Transfer, 52 (21), 5204–5212, 2009. doi:https://doi.org/10.1016/j.ijheatmasstransfer.2009.04.025.

Mukherjee et al., 2011. A. Mukherjee, S.G. Kandlikar and Z.J. Edel. *Numerical study of bubble growth and wall heat transfer during flow boiling in a microchannel*. International Journal of Heat and Mass Transfer, 54(15), 3702 – 3718, 2011. doi:https://doi.org/10.1016/j.ijheatmasstransfer.2011.01.030.

Márkus et al., 2012. Attila Márkus and Gábor Házi. *Numerical simulation of the detachment of bubbles from a rough surface at microscale level*. Nuclear Engineering and Design, 248, 263 – 269, 2012. ISSN: 0029-5493. doi:https://doi.org/10.1016/j.nucengdes.2012.03.040. URL: http://www.sciencedirect.com/science/article/pii/S0029549312001744.

Okajima et al., 2019. Junnosuke Okajima and Peter Stephan. *Numerical simulation of liquid film formation and its heat transfer through vapor bubble expansion in a microchannel*. International Journal of Heat and Mass Transfer, 136(1), 1241–1249, 2019. doi:https://doi.org/10.1016/j.ijheatmasstransfer.2019.03.004.

Pan et al., 2020. Zhenhai Pan, Yu Shen and Huiying Wu. *Saturated flow boiling of isolated seed bubble across a heated square cylinder in two-dimensional microchannel*. International Journal of Heat and Mass Transfer, 157(1), 119885, 2020. doi:https://doi.org/10.1016/j.ijheatmasstransfer.2020.119885.

Prajapati et al., 2017. Yogesh K. Prajapati and Prabhakar Bhandari. *Flow boiling instabilities in microchannels and their promising solutions – A review*. Experimental Thermal and Fluid Science, 88 (1), 576–593, 2017. doi:https://doi.org/10.1016/j.expthermflusci.2017.07.014.

Prajapati et al., 2015. Yogesh K. Prajapati, Manabendra Pathak and Mohd. Kaleem Khan. *A comparative study of flow boiling heat transfer in three different configurations of microchannels*. International Journal of Heat and Mass Transfer, 85(1), 711–722, 2015. doi:https://doi.org/10.1016/j.ijheatmasstransfer.2015.02.016.

Qu et al., 2001. Weilin Qu, Seok-Mann Yoon and Issam Mudawar. *Two-Phase Flow and Heat Transfer in Rectangular Micro-Channels*. Journal of Electronic Packaging, 126(3), 288–300, 2001. doi:10.1115/1.1756589.

Reimann et al., 1975. M. Reimann and U. Grigull. *Wärmeübergang bei freier Konvektion und Filmsieden im kritischen Gebiet von Wasser und Kohlendioxid*. Wärme - und Stoffübertragung, 8, 229–239, 1975. ISSN: 1432-1181. doi:10.1115/1.3682280. URL: https://doi.org/10.1007/BF01002151.

Saha, 2015. Sujoy Kumar Saha. *Microchannel Phase Change Transport Phenomena*. Elsevier Science Technology, 1 edition, 2015. ISBN: 9780128043561.

Samkhaniani et al., 2017. Nima Samkhaniani and Mohamad Reza Ansari. *The evaluation of the diffuse interface method for phase change simulations using OpenFOAM*. Heat Transfer—Asian Research, 46(8), 1173–1203, 2017. doi:https://doi.org/10.1002/htj.21268. URL: https://onlinelibrary.wiley.com/doi/abs/10.1002/htj.21268.

Schrage, 1953. Robert W. Schrage. *A Theoretical Study of Interphase Mass Transfer*. Columbia University Press, 1953. doi:doi:10.7312/schr90162. URL: https://doi.org/10.7312/schr90162.

Serizawa et al., 2002. Akimi Serizawa, Ziping Feng and Zensaku Kawara. *Two-phase flow in microchannels*. Experimental Thermal and Fluid Science, 26(6), 703–714, 2002. doi:https://doi.org/10.1016/S0894-1777(02)00175-9.

Steinke et al., 2004. Mark Steinke and Satish Kandlikar. *An Experimental Investigation of Flow Boiling Characteristics of Water in Parallel Microchannels*. Journal of Heat Transfer-transactions of The Asme - J HEAT TRANSFER, 126(1), 518–526, 2004. doi:10.1115/1.1778187.

Tanasawa, 1991. Ichiro Tanasawa. *Advances in Condensation Heat Transfer*. 21, 55 – 139, 1991. ISSN: 0065-2717. doi:https://doi.org/10.1016/S0065-2717(08)70334-4. URL: http://www.sciencedirect.com/science/article/pii/S0065271708703344.

Tullius et al., 2011. Jami F. Tullius, Robert Vajtai and Yildiz Bayazitoglu. *A Review of Cooling in Microchannels*. Heat Transfer Engineering, 32(7-8), 527–541, 2011. doi:10.1080/01457632.2010.506390.

VDI, 2010. Gesellschaft Verfahrenstechnik und Chemieingenieurwesen VDI. *VDI Heat Atlas*. Springer, Berlin, Heidelberg, 2.ed edition, 2010. ISBN: 978-3-540-77877-6. doi:10.1007/978-3-540-77877-6.

Wang et al., 2007. Guodong Wang, Ping Cheng and Huiying Wu. *Unstable and stable flow boiling in parallel microchannels and in a single microchannel*. International Journal of Heat and Mass Transfer, 50(21), 4297–4310, 2007. doi:https://doi.org/10.1016/j.ijheatmasstransfer.2007.01.033.

Wang et al., 2012. Yuan Wang, Khellil Sefiane and Souad Harmand. *Flow boiling in high-aspect ratio mini- and micro-channels with FC-72 and ethanol: Experimental results and heat transfer correlation assessments*. Experimental Thermal and Fluid Science, 36(1), 93–106, 2012. doi:https://doi.org/10.1016/j.expthermflusci.2011.09.001.

Welch et al., 2000. S W.J. Welch and J Wilson. *A volume of fluid based method for fluid flows with phase change*. Journal of Computational Physics, 160(2), 2000. ISSN: 0021-9991. doi:10.1006/jcph.2000.6481.

Whalley, 1996. P. B. Whalley. *Two-Phase Flow and Heat Transfer*. Oxford Science Publications, 1 edition, 1996. ISBN: 0-19-856444-9.

Yen et al., 2006. Tzu-Hsiang Yen, Masahiro Shoji, Fumio Takemura, Yuji Suzuki and Nobuhide Kasagi. *Visualization of convective boiling heat transfer in single microchannels with different shaped cross-sections*. International Journal of Heat and Mass Transfer, 49(21), 3884–3894, 2006. doi:https://doi.org/10.1016/j.ijheatmasstransfer.2005.12.024.

Yin et al., 2016. Liaofei Yin and Li Jia. *Confined bubble growth and heat transfer characteristics during flow boiling in microchannel*. International Journal of Heat and Mass Transfer, 98, 114–123, 2016. ISSN: 0017-9310. doi:https://doi.org/10.1016/j.ijheatmasstransfer.2016.02.063. URL: https://www.sciencedirect.com/science/article/pii/S0017931015311571.

Appendix A

OpenFOAM Code

A.1 OpenFOAM Code Flow Boiling

Listing A.1: The different setting used for the simulations.

```
/*---------------------------------*- C++ -*----------------------------------*\
| =========                 |                                                 |
| \\      /  F ield         | OpenFOAM: The Open Source CFD Toolbox           |
|  \\    /   O peration     | Website:  https://openfoam.org                  |
|   \\  /    A nd           | Version:  8                                     |
|    \\/     M anipulation  |                                                 |
\*---------------------------------------------------------------------------*/
FoamFile
{
    version     8.0;
    format      binary;
    class       dictionary;
    location    "system";
    object      controlDict;
}
// * * * * * * * * * * * * * * * * * * * * * * * * * * * * * * * * * * * * //

application     thermalPhaseChangeFoam;

startFrom       latestTime;

startTime       0.0;

stopAt          endTime;

endTime         0.02;

deltaT          1E-8;

writeControl    adjustableRunTime;
writeInterval   0.0001;

purgeWrite      0;

writeFormat     binary;

writePrecision  8;
```

```
writeCompression uncompressed;

timeFormat      general;

timePrecision   8;

runTimeModifiable yes;

adjustTimeStep  on;

maxAlphaCo      0.5;
maxCo           0.5;
maxFourier      100;
maxDeltaT       2E-6;
libs
(
    "libdynamicFvMeshUser.so"
);
// ************************************************************************* //
```

Listing A.2: The schemes used for the simulations.

```
/*--------------------------------*- C++ -*----------------------------------*\
| =========                 |                                                 |
| \\      /  F ield         | OpenFOAM: The Open Source CFD Toolbox           |
|  \\    /   O peration     | Website:  https://openfoam.org                  |
|   \\  /    A nd           | Version:  8                                     |
|    \\/     M anipulation  |                                                 |
\*---------------------------------------------------------------------------*/
FoamFile
{
    version     8.0;
    format      binary;
    class       dictionary;
    location    "system";
    object      fvSchemes;
}
// * * * * * * * * * * * * * * * * * * * * * * * * * * * * * * * * * * * * * //

ddtSchemes
{
    default          Euler;
}

gradSchemes
{
    default          Gauss linear;
    grad(U)          cellLimited Gauss linear 1;

}

divSchemes
{

    div(phi,alpha) Gauss interfaceCompression vanLeer 1
    div(phi,omega)  Gauss upwind;
    div(((rho*nuEff)*dev2(T(grad(U))))) Gauss linear;
    div(rho*phi,U)  Gauss upwind;
    div(rhoPhi,T)   Gauss upwind;
    div(rhoPhi,K)   Gauss upwind;
    div(rhoPhi,U)   Gauss upwind;
    div(phi,p)      Gauss upwind;
    div(phi,T)      Gauss upwind;
    div(phi,k)          Gauss upwind;
    div(phi,epsilon)    Gauss upwind;
    default             Gauss upwind;
}
```

```
laplacianSchemes
{
    default         Gauss linear limited corrected 0.33;
}

interpolationSchemes
{
    default         linear;
}

snGradSchemes
{
    default         limited corrected 0.33;
}

// ************************************************************************* //
```

Listing A.3: The domain used for the simulations.

```
/*--------------------------------*- C++ -*----------------------------------*\
| =========                 |                                                 |
| \\      /  F ield         | OpenFOAM: The Open Source CFD Toolbox           |
|  \\    /   O peration     | Website:  https://openfoam.org                  |
|   \\  /    A nd           | Version:  8                                     |
|    \\/     M anipulation  |                                                 |
\*---------------------------------------------------------------------------*/
FoamFile
{
    version     8.0;
    format      binary;
    class       dictionary;
    location    "";
    object      system/blockMeshDict;
}
// * * * * * * * * * * * * * * * * * * * * * * * * * * * * * * * * * * * * * //

convertToMeters 0.001;


vertices
(
    (0.000000e+00 0.000000e+00 0.000000e+00) // 0
    (2.000000e-01 0.000000e+00 0.000000e+00) // 1
    (2.000000e-01 -1.500000e-02 0.000000e+00) // 2
    (2.150000e-01 -1.500000e-02 0.000000e+00) // 3
    (2.150000e-01 0.000000e+00 0.000000e+00) // 4
    (1.500000e+00 0.000000e+00 0.000000e+00) // 5
    (1.500000e+00 1.000000e-01 0.000000e+00) // 6
    (2.150000e-01 1.000000e-01 0.000000e+00) // 7
    (2.000000e-01 1.000000e-01 0.000000e+00) // 8
    (0.000000e+00 1.000000e-01 0.000000e+00) // 9
    (0.000000e+00 0.000000e+00 1.000000e-02) // 10
    (2.000000e-01 0.000000e+00 1.000000e-02) // 11
    (2.000000e-01 -1.500000e-02 1.000000e-02) // 12
    (2.150000e-01 -1.500000e-02 1.000000e-02) // 13
    (2.150000e-01 0.000000e+00 1.000000e-02) // 14
    (1.500000e+00 0.000000e+00 1.000000e-02) // 15
    (1.500000e+00 1.000000e-01 1.000000e-02) // 16
    (2.150000e-01 1.000000e-01 1.000000e-02) // 17
    (2.000000e-01 1.000000e-01 1.000000e-02) // 18
    (0.000000e+00 1.000000e-01 1.000000e-02) // 19
);

blocks
(
```

```
hex (0 1 8 9 10 11 18 19) (80 40 1) simpleGrading (1 1 1)
hex (1 4 7 8 11 14 17 18) (6 40 1) simpleGrading (1 1 1)
hex (2 3 4 1 12 13 14 11) (6 6 1) simpleGrading (1 1 1)
hex (4 5 6 7 14 15 16 17) (514 40 1) simpleGrading (1 1 1)
);

edges
(
);

boundary
(
inlet
{
type patch;
faces
(
(0 10 19 9)
);
}
walls
{
type wall;
faces
(
(9 19 18 8)
(10 0 1 11)
(8 18 17 7)
(7 17 16 6)
(14 4 5 15)
);
}
cavity
{
type wall;
faces
(
(12 2 3 13)
(3 4 14 13)
(1 2 12 11)
);
}
front
{
type empty;
faces
(
```

```
(19 10 11 18)
(18 11 14 17)
(11 12 13 14)
(17 14 15 16)
);
}
back
{
type empty;
faces
(
(0 9 8 1)
(1 8 7 4)
(2 1 4 3)
(4 7 6 5)
);
}
outlet
{
type patch;
faces
(
(5 6 16 15)
);
}
);

mergePatchPairs
(
);

// ************************************************************************* //
```

Listing A.4: The temperature boundaries used for the simulations.

```
/*--------------------------------*- C++ -*----------------------------------*\
| =========                 |                                                 |
| \\      /  F ield         | OpenFOAM: The Open Source CFD Toolbox           |
|  \\    /   O peration     | Website:  https://openfoam.org                  |
|   \\  /    A nd           | Version:  8                                     |
|    \\/     M anipulation  |                                                 |
\*---------------------------------------------------------------------------*/
FoamFile
{
    version     8.0;
    format      binary;
    class       volScalarField;
    location    "0";
    object      T;
}
// * * * * * * * * * * * * * * * * * * * * * * * * * * * * * * * * * * * * //

dimensions      [0 0 0 1 0 0 0];

internalField uniform 346.55;

boundaryField
{
    inlet
    {
        type            fixedValue;
        value           uniform 346.55;
    }
    walls
    {
        type            fixedGradient;
        gradient        uniform 150982.376;
    }
    cavity
    {
        type            fixedGradient;
        gradient        uniform 150982.376;
    }
    front
    {
        type            empty;
    }
    back
    {
        type            empty;
    }
```

```
    outlet
    {
        type            zeroGradient;
    }
}


// ************************************************************************* //
```

Listing A.5: The velocity boundaries used for the simulations.

```
/*--------------------------------*- C++ -*----------------------------------*\
| =========                 |                                                 |
| \\      /  F ield         | OpenFOAM: The Open Source CFD Toolbox           |
|  \\    /   O peration     | Website:  https://openfoam.org                  |
|   \\  /    A nd           | Version:  8                                     |
|    \\/     M anipulation  |                                                 |
\*---------------------------------------------------------------------------*/
FoamFile
{
    version     8.0;
    format      binary;
    class       volVectorField;
    location    "0";
    object      U;
}
// * * * * * * * * * * * * * * * * * * * * * * * * * * * * * * * * * * * * //

dimensions      [0 1 -1 0 0 0 0];

internalField   uniform (0.297 0 0);

boundaryField
{
    inlet
    {
        type            fixedValue;
        value           uniform (0.297 0 0);
    }
    walls
    {
        type            noSlip;
    }
    cavity
    {
        type            noSlip;
    }
    front
    {
        type            empty;
    }
    back
    {
        type            empty;
    }
    outlet
    {
```

```
        type            zeroGradient;
    }
}


// ************************************************************************* //
```

Listing A.6: The pressure boundaries used for the simulations.

```
/*--------------------------------*- C++ -*----------------------------------*\
| =========                 |                                                 |
| \\      /  F ield         | OpenFOAM: The Open Source CFD Toolbox           |
|  \\    /   O peration     | Website:  https://openfoam.org                  |
|   \\  /    A nd           | Version:  8                                     |
|    \\/     M anipulation  |                                                 |
\*---------------------------------------------------------------------------*/
FoamFile
{
    version     8.0;
    format      binary;
    class       volScalarField;
    location    "0";
    object      p_rgh;
}
// * * * * * * * * * * * * * * * * * * * * * * * * * * * * * * * * * * * * //

dimensions      [1 -1 -2 0 0 0 0];

internalField   uniform 101325;

boundaryField
{
    inlet
    {
        type            zeroGradient;
    }
    walls
    {
        type            zeroGradient;
    }
    cavity
    {
        type            zeroGradient;
    }
    front
    {
        type            empty;
    }
    back
    {
        type            empty;
    }
    outlet
    {
        type            fixedValue;
```

```
        value           uniform 101325;
    }
}


// ************************************************************************* //
```

Listing A.7: The volume fraction of liquid boundaries used for the simulations.

```
/*--------------------------------*- C++ -*----------------------------------*\
| =========                 |                                                 |
| \\      /  F ield         | OpenFOAM: The Open Source CFD Toolbox           |
|  \\    /   O peration     | Website:  https://openfoam.org                  |
|   \\  /    A nd           | Version:  8                                     |
|    \\/     M anipulation  |                                                 |
\*---------------------------------------------------------------------------*/
FoamFile
{
    version     8.0;
    format      binary;
    class       volScalarField;
    location    "0";
    object      alpha.water;
}
// * * * * * * * * * * * * * * * * * * * * * * * * * * * * * * * * * * * * * //

dimensions      [0 0 0 0 0 0 0];

internalField   uniform 1;

boundaryField
{
    inlet
    {
        type            fixedValue;
        value           uniform 1;
    }

    walls
    {
        type            constantAlphaContactAngle;
        gradient        uniform 1;
        limit           zeroGradient;
        theta0          30;
        value           uniform 1;
    }

    cavity
    {
        type            constantAlphaContactAngle;
        gradient        uniform 1;
        limit           zeroGradient;
        theta0          30;
        value           uniform 1;
    }
```

```
    front
    {
        type            empty;
    }

    back
    {
        type            empty;
    }

    outlet
    {
        type            zeroGradient;
    }
}


// ************************************************************************* //
```

Listing A.8: The liquid and gas properties used for the simulations.

```
/*--------------------------------*- C++ -*----------------------------------*\
| =========                 |                                                 |
| \\      /  F ield         | OpenFOAM: The Open Source CFD Toolbox           |
|  \\    /   O peration     | Website:  https://openfoam.org                  |
|   \\  /    A nd           | Version:  8                                     |
|    \\/     M anipulation  |                                                 |
\*---------------------------------------------------------------------------*/
FoamFile
{
    version     8.0;
    format      binary;
    class       dictionary;
    object      transportProperties;
}
// * * * * * * * * * * * * * * * * * * * * * * * * * * * * * * * * * * * * //
phases (water vapour);

phaseChange true;


phaseChangeTwoPhaseMixture Hardt;

pSat             pSat       [1 -1 -2 0 0 0 0]    101325;

TSat             TSat       [0 0  0  1 0 0 0]     351.55;
R                R          [0 2 -2 -1 0 0 0]     180.5;
TSatLocal        false;


Hfg              Hfg        [0 2 -2 0 0 0 0]      849883;
sigma            sigma      [1 0 -2 0 0 0 0]      0.01764;

water //liquid
{
    transportModel Newtonian;
    nu              nu  [0 2 -1 0 0 0 0]  6.156e-07;
    rho             rho [1 -3 0 0 0 0 0]  737.4;
    C               C   [0 2 -2 -1 0 0 0] 2920;
    K               K   [1 1 -3 -1 0 0 0] 0.1541;
}

vapour//vapor
{
  transportModel Newtonian;
    nu              nu [0 2 -1 0 0 0 0]  6.356e-06;
    rho             rho [1 -3 0 0 0 0 0] 1.645;
```

```
    C               C [0 2 -2 -1 0 0 0]  1720;
    K               K  [1 1 -3 -1 0 0 0] 0.02056;
}

HardtCoeffs
{

  Cv            Cv    [0 0 0 0 0 0 0]     1;
  rv            rv    [0 0 0 0 0 0 0]     1;
  rc            rc    [0 0 0 0 0 0 0]     0;

}

LeeCoeffs
{
  rv            rv    [0 0 -1 0 0 0 0]    1000;
  rc            rc    [0 0 -1 0 0 0 0]    0;
}

FourierCoeffs
{

  r             r    [0 0 0 0 0 0 0]     1E5;
  type          invLinear;//
}

//  ************************************************************************* //
```

Listing A.9: gravitational acceleration.

```
/*--------------------------------*- C++ -*----------------------------------*\
| =========                 |                                                 |
| \\      /  F ield         | OpenFOAM: The Open Source CFD Toolbox           |
|  \\    /   O peration     | Website:  https://openfoam.org                  |
|   \\  /    A nd           | Version:  8                                     |
|    \\/     M anipulation  |                                                 |
\*---------------------------------------------------------------------------*/
FoamFile
{
    version     8.0;
    format      binary;
    class       uniformDimensionedVectorField;
    location    "constant";
    object      g;
}
// * * * * * * * * * * * * * * * * * * * * * * * * * * * * * * * * * * * * //

dimensions      [0 1 -2 0 0 0 0];
value           ( 0 -9.81 0 );


// ************************************************************************* //
```

Listing A.10: momentum Transport.

```
/*--------------------------------*- C++ -*----------------------------------*\
| =========                 |                                                 |
| \\      /  F ield         | OpenFOAM: The Open Source CFD Toolbox           |
|  \\    /   O peration     | Website:  https://openfoam.org                  |
|   \\  /    A nd           | Version:  8                                     |
|    \\/     M anipulation  |                                                 |
\*---------------------------------------------------------------------------*/
FoamFile
{
    version     8.0;
    format      binary;
    class       dictionary;
    object      momentumTransport;
}
// * * * * * * * * * * * * * * * * * * * * * * * * * * * * * * * * * * * * //

simulationType laminar;


// ************************************************************************* //
```

Listing A.11: turbulence Properties.

```
/*---------------------------*- C++ -*----------------------------*\
| =========                 |                                     |
| \\      /  F ield         | OpenFOAM: The Open Source CFD Toolbox |
|  \\    /   O peration     | Website:  https://openfoam.org      |
|   \\  /    A nd           | Version:  8                         |
|    \\/     M anipulation  |                                     |
\*---------------------------------------------------------------*/
FoamFile
{
    version     8.0;
    format      binary;
    class       dictionary;
    location    "constant";
    object      turbulenceProperties;
}
// * * * * * * * * * * * * * * * * * * * * * * * * * * * * * * * * * * * * //

simulationType  laminar;

// ************************************************************************* //
```

Listing A.12: setFieldsDict.

```
/*--------------------------------*- C++ -*----------------------------------*\
| =========                 |                                                 |
| \\      /  F ield         | OpenFOAM: The Open Source CFD Toolbox           |
|  \\    /   O peration     | Website:  https://openfoam.org                  |
|   \\  /    A nd           | Version:  8                                     |
|    \\/     M anipulation  |                                                 |
\*---------------------------------------------------------------------------*/
FoamFile
{
    version     8.0;
    format      binary;
    class       dictionary;
    location    "system";
    object      setFieldsDict;
}
// * * * * * * * * * * * * * * * * * * * * * * * * * * * * * * * * * * * * * //


defaultFieldValues
(
        volScalarFieldValue alpha.water 1
        volScalarFieldValue T 346.55
);

regions
(
        boxToCell
        {
                box (0.0002 -0.000015 0) (0.000215 0.00000 0.00001);
                fieldValues
                (
                        volScalarFieldValue alpha.water 0
                        volScalarFieldValue T 351.75
                );
        }
);



// ************************************************************************* //
```

Listing A.13: fvSolution.

```
/*--------------------------------*- C++ -*----------------------------------*\
| =========                 |                                                 |
| \\      /  F ield         | OpenFOAM: The Open Source CFD Toolbox           |
|  \\    /   O peration     | Website:  https://openfoam.org                  |
|   \\  /    A nd           | Version:  8                                     |
|    \\/     M anipulation  |                                                 |
\*---------------------------------------------------------------------------*/
FoamFile
{
    version     8.0;
    format      binary;
    class       dictionary;
    object      fvSolution;
}
// * * * * * * * * * * * * * * * * * * * * * * * * * * * * * * * * * * * * //

solvers
{
    "alpha.water.*"
    {
        maxUnboundedness 1e-5;
        CoCoeff          2;
        nLimiterIter     2;

        cAlpha           0;
        nAlphaCorr       2;
        nAlphaSubCycles  1;

        MULESCorr        yes;

        solver           smoothSolver;
        smoother         symGaussSeidel;
        tolerance        1e-8;
        relTol           0;
        maxIter          10;
            smoothItr                   2;
    kSmoothItr                  0;
    };

    "(U|UFinal)"
    {
        solver           PBiCG;
        preconditioner   DILU;
        tolerance        1e-08;
        relTol           0;
    };
```

```
p_rgh
{
    solver          PCG;
    preconditioner
    {
        preconditioner  GAMG;
        tolerance       1e-08;
        relTol          0;
        nVcycles        2;
        smoother        GaussSeidel;
        nPreSweeps      0;
        nPostSweeps     2;
        nFinestSweeps   2;
        cacheAgglomeration true;
        nCellsInCoarsestLevel 10;
        agglomerator    faceAreaPair;
        mergeLevels     1;
    }

    tolerance       1e-08;
    relTol          0;
    maxIter         20;
};

"pcorr.*"
{
    $p_rgh;
    relTol          0;
};

Phi
{
    $p_rgh;
    relTol          0;
};


p_rghFinal
 {
    solver          PCG;
    preconditioner
    {
        preconditioner  GAMG;
        tolerance       1e-08;
        relTol          0;
        nVcycles        2;
```

```
            smoother          GaussSeidel;
            nPreSweeps        0;
            nPostSweeps       2;
            nFinestSweeps     2;
            cacheAgglomeration true;
            nCellsInCoarsestLevel 10;
            agglomerator      faceAreaPair;
            mergeLevels       1;
        }

        tolerance         1e-08;
        relTol            0;
        maxIter           20;
    };

    "(T|TFinal)"
    {
        solver            PBiCG;
        preconditioner    DILU;
        tolerance         1e-10;
        relTol            0;
    };

    rho    //add
    {
        solver            Diagonal;
        tolerance         1e-8;
        relTol            0;
    };

}

potentialFlow
{
    nNonOrthogonalCorrectors    3;
}

PIMPLE
{
    momentumPredictor           yes;
    nOuterCorrectors            1;
    nCorrectors                 3;
    nNonOrthogonalCorrectors    0;

    cAlpha                      1;
    nAlphaCorr                  1;
    nAlphaSubCycles             4;
```

```
    smoothItr                   2;
    kSmoothItr                  0;




        correctPhi          yes;
    nOuterCorrectors    3;
    nCorrectors         1;
    nNonOrthogonalCorrectors 0;
}


// ************************************************************************* //
```

Appendix B

Visual Representation of the Simulations

The following figures show the first time step after the bubble detachment for all of the 20 cases. In Table B.1, the cases are described and in Figure B.1 an illustration of the domain and the dimensionless numbers L_E/d_h and d_E/d_h are shown.

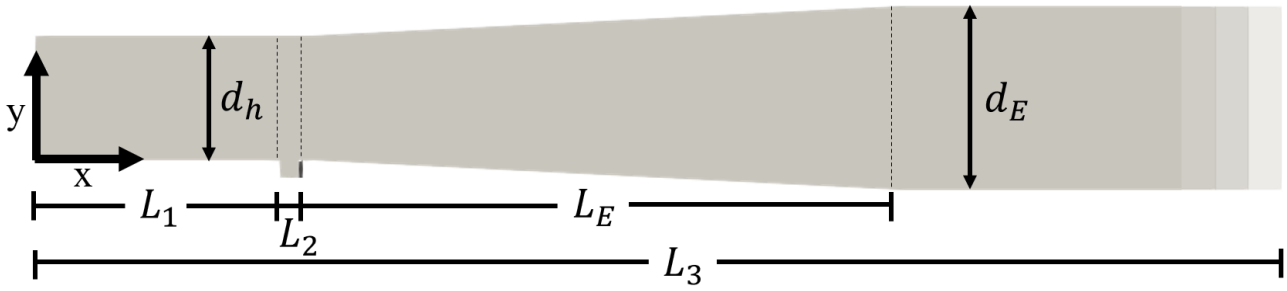

Figure B.1: Sketch of the divergent shaped microchannel and the relevant dimensions for the dimensionless numbers L_E/d_h and d_E/d_h.

Table B.1: Description of the 20 cases.

	L_E/d_h	d_E/d_h	B	**Case nr.**
Cases with their different parameters	0	1	$1.25 \cdot 10^{-4}$	Case 1
			$1.75 \cdot 10^{-4}$	Case 2
	2	1.25	$1.25 \cdot 10^{-4}$	Case 3
			$1.75 \cdot 10^{-4}$	Case 4
		1.5	$1.25 \cdot 10^{-4}$	Case 5
			$1.75 \cdot 10^{-4}$	Case 6
		1.75	$1.25 \cdot 10^{-4}$	Case 7
			$1.75 \cdot 10^{-4}$	Case 8
	5	1.25	$1.25 \cdot 10^{-4}$	Case 9
			$1.75 \cdot 10^{-4}$	Case 10
		1.5	$1.25 \cdot 10^{-4}$	Case 11
			$1.75 \cdot 10^{-4}$	Case 12
		1.75	$1.25 \cdot 10^{-4}$	Case 13
			$1.75 \cdot 10^{-4}$	Case 14
	10	1.25	$1.25 \cdot 10^{-4}$	Case 15
			$1.75 \cdot 10^{-4}$	Case 16
		1.5	$1.25 \cdot 10^{-4}$	Case 17
			$1.75 \cdot 10^{-4}$	Case 18
		1.75	$1.25 \cdot 10^{-4}$	Case 19
			$1.75 \cdot 10^{-4}$	Case 20

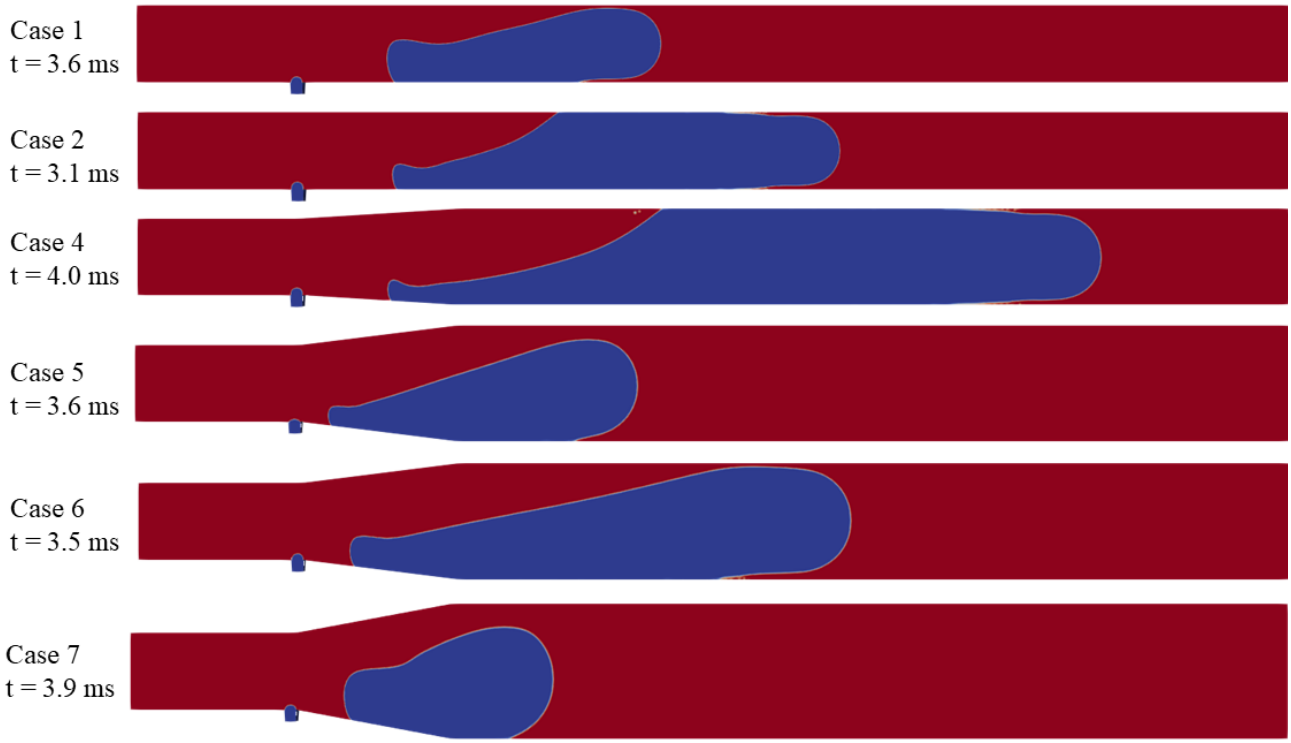

Figure B.2: .

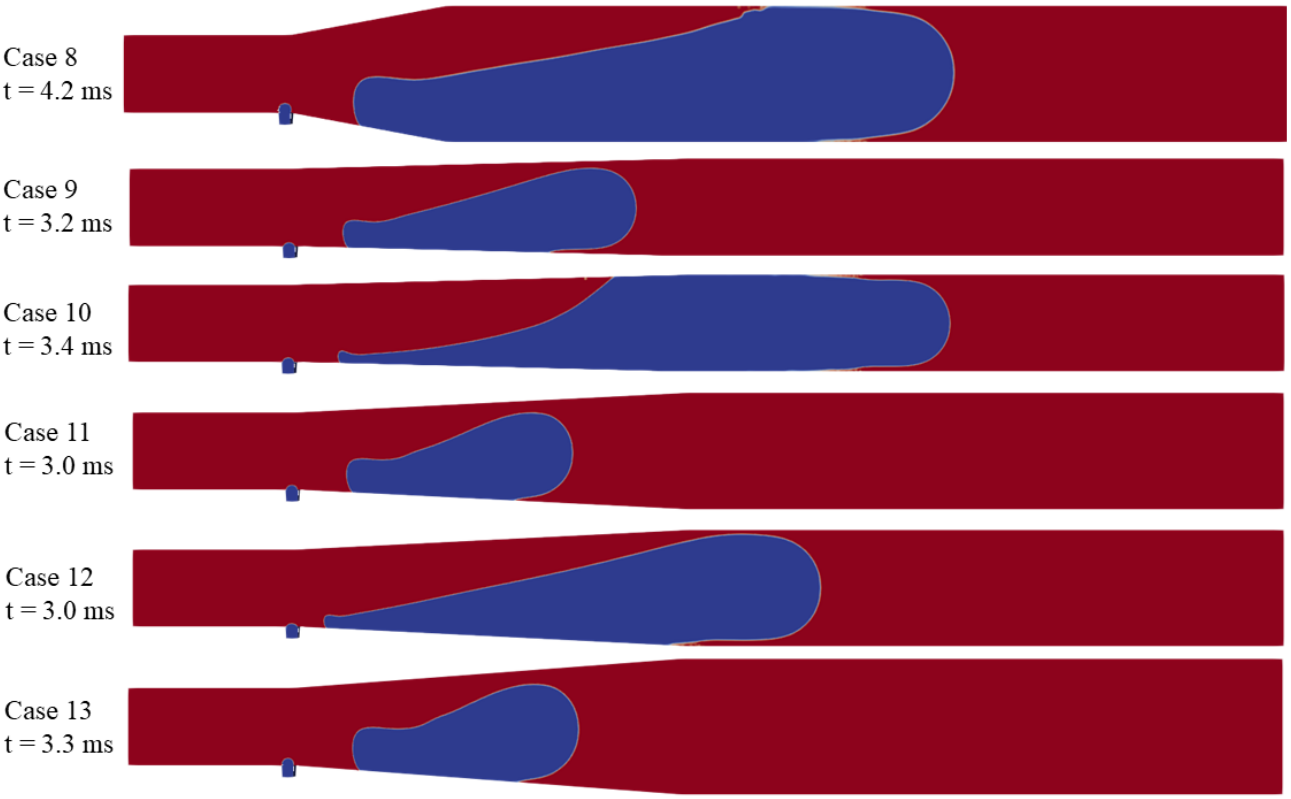

Figure B.3: .

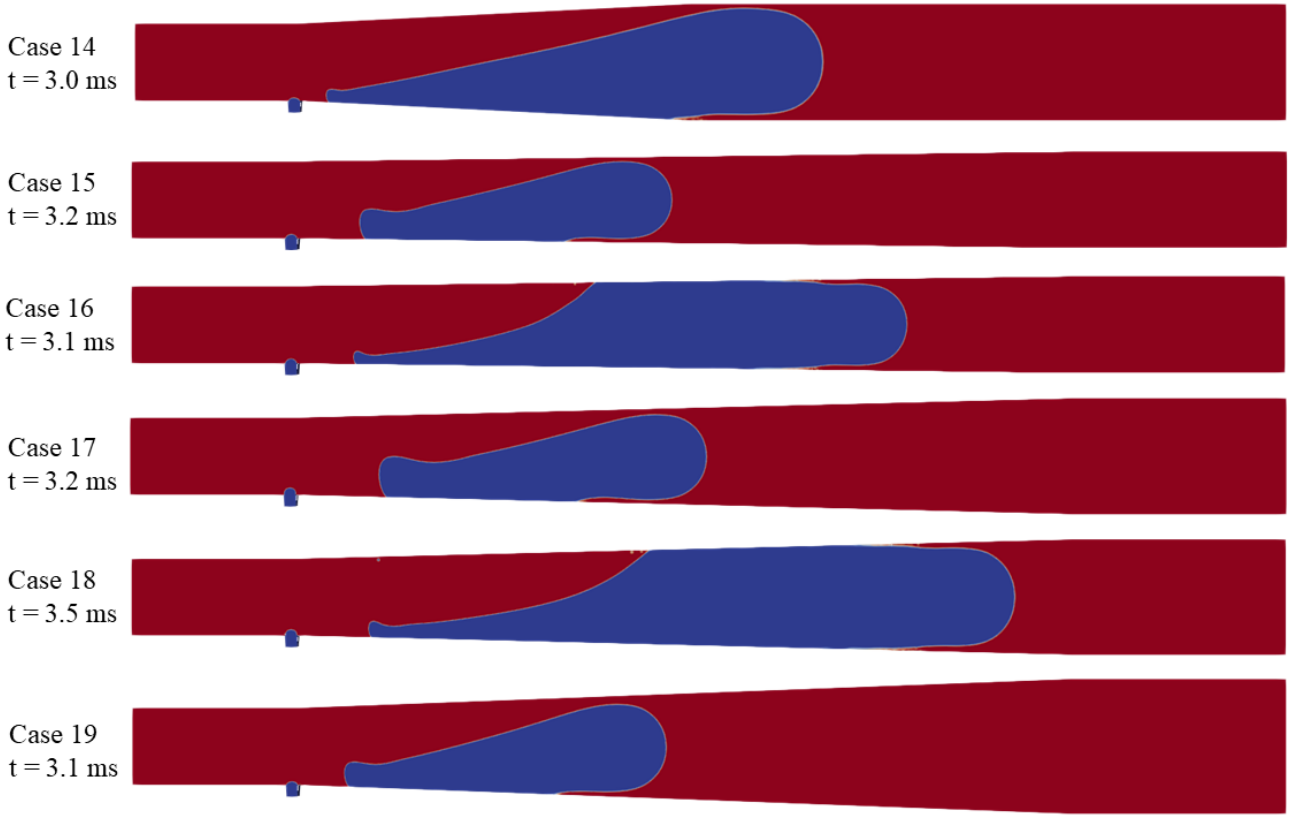

Figure B.4: .

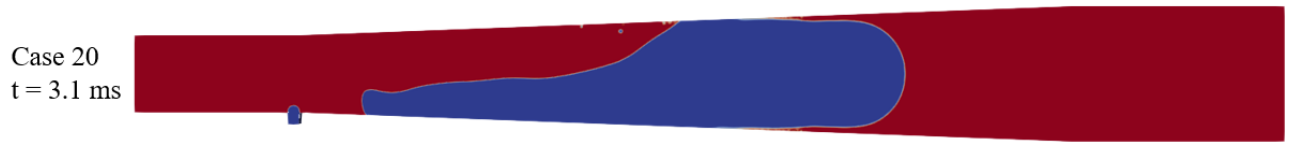

Figure B.5: .